INTERACTION OF PAYLOAD AND ATTITUDE CONTROLLER IN SPACE ROBOTIC SYSTEMS

Eric Martin

B. Eng. (University of Sherbrooke), 1992

Department of Mechanical Engineering
McGill University
Montreal, Quebec, Canada

A thesis submitted to the Faculty of Graduate Studies and Research
in partial fulfilment of the requirements of the degree of
Master of Engineering

November 1994

ISBN 0-612-05461-6

Abstract

Space manipulators mounted on a free-floating base are structurally flexible mechanical systems. For some applications, it is necessary to control the attitude of the base by the use of on-off thrusters. However, thruster operation produces a rather broad frequency spectrum that can excite sensitive modes of the flexible system. This situation is likely to occur especially when the manipulator is moving a big payload. The excitation of these modes can introduce further disturbances to the attitude control system, and therefore, undesirable fuel replenishing limit cycles may develop. To investigate these dynamic interactions, an approximate two-mass system, where the manipulator is replaced with an equivalent spring-and-dashpot system, is used to reproduce the relative motion of the payload with respect to the spacecraft. A dynamic model of a two-flexible-joint planar manipulator was derived to obtain its natural frequencies and then, to determine the corresponding spring stiffness and damping coefficient of the approximate system. Since the attitude controller assumes the use of on-off thrusters, which are nonlinear devices, the describing function technique, an approximate method for the analysis of nonlinear systems, is used to perform a parametric study investigating the significant parameters of three models studied. This study provides some guidelines for the design of attitude control systems when flexibility is a major concern. As well, this study shows that one of the three models studied is a very good alternative to the actual attitude controllers. Finally, simulations are executed to confirm these results and to study the addition of noise and model uncertainties in the three selected models.

Résumé

Les robots manipulateurs montés sur une base flottante et opérant dans l'espace sont des systèmes mécaniques flexibles. Pour certaines opérations, il est nécessaire de commander la position de la base en utilisant des fusées de type tout-ou-rien. Cependant, l'opération de ces fusées produit un large spectre de fréquences qui peuvent exciter les modes vibratoires du système. Cette situation devenant plus probable lorsque le manipulateur transporte de grosses charges. L'excitation de ces modes peut introduire davantage de perturbations au système de commande, continuant alors le cycle et augmentant en même temps la consommation de combustible, sans stabiliser la base. Afin d'étudier ces interactions dynamiques, un modèle simplifié à deux masses, remplaçant le manipulateur par un système équivalent ressort-amortisseur, est utilisé pour reproduire le mouvement relatif de la charge par rapport à la base. Un modèle dynamique d'un manipulateur planaire à deux articulations flexibles a été développé afin d'obtenir les fréquences de résonance et ainsi déterminer la rigidité du ressort et le coefficient d'amortissement nécessaire pour le système simplifié. Puisque la commande présume l'utilisation de fusées tout-ou-rien, qui sont des mécanismes non-linéaires, la technique des fonctions descriptives a été utilisée pour effectuer une étude paramétrique examinant les paramètres importants de trois modèles différents. Cette étude fournie quelques lignes directrices dans la conception de ce type de commande, lorsque la flexibilité du système est un paramètre important. En outre, cette étude démontre qu'un des trois modèles étudiés pourrait être une très bonne solution de rechange aux méthodes de commande utilisées à l'heure actuelle dans l'espace.

Acknowledgements

I would like to thank my research supervisors, Professors J. Angeles and E. Papadopoulos for their guidance, encouragement and support throughout the Master's program. Working in conjunction with them was a very enriching experience.

I would like to express my gratitude to those who helped me with the English while producing this thesis, particularly Mr. Bernard Boutin. Many thanks are also due to the Centre for Intelligent Machines (CIM) for all the computer facilities provided and for the pleasant research environment.

I am very grateful to my wife, Dominique Mathieu, for her love, support and understanding throughout my thesis work, and most of all, for convincing me to pursue graduate studies.

This research was possible under the NSERC (Natural Science and Engineering Research Council of Canada) Research Grants OGPIN 013 and OGP0004532. Funding was also provided to the author through an NSERC graduate scholarship.

Contents

List of Figures

List of Tables

Nomenclature

All bold-face, lower-case, Latin and Greek letters used in this thesis denote vectors; all bold-face, upper-case, Latin and Greek letters denote matrices.

A	: amplitude of the sinusoidal input in the describing function method
$\mathbf{A}$	: plant coefficient matrix of the state equations
$\mathbf{b}$	: control vector of the state equations
B	: amplitude of the force developed by the thrusters
c	: damping ratio of the simplified system
$\mathbf{c}$	: output vector of the state equations
c_i	: ith-joint damping coefficient for the 2-DOF manipulator system
$\mathbf{C}$	: damping matrix of the 2-DOF manipulator system
$\mathbf{C}_2$	: reduced damping matrix of the 2-DOF manipulator system
CM	: centre of mass of the 2-DOF manipulator system
e	: error on the position of the base or the spacecraft
$\mathbf{E}$	: output matrix of the state equations
F	: force acting on the mass of the single-mass system example
$F_c(t)$	: fuel consumption
$G_{\mathrm{asym}}(s)$	: transfer function representing the linear elements of the model with an asymptotic state-estimator
$G_{\mathrm{filter}}(s)$	: transfer function representing the linear elements of the model with position and velocity filters
$G_p(s)$	: transfer function representing the plant of the simplified system

$G_{rate}(s)$: transfer function representing the linear elements of the model with a velocity estimator and a position filter

H_{ij} : (i,j) component of $\mathbf{H}^*(\mathbf{q}_r)$ for the 2-DOF manipulator system

$\mathbf{H}^*(\mathbf{q}_r)$: reduced inertia matrix for the 2-DOF manipulator system

I_i : ith-body moment of inertia with respect to the centre of mass of the body for the 2-DOF manipulator system

J_i : ith-motor moment of inertia for the 2-DOF manipulator system

J_{ij} : (i,j) entry of $\mathbf{J}(\mathbf{q}_r)$ for the 2-DOF manipulator system

$\mathbf{J}(\mathbf{q}_r)$: Jacobian matrix for the 2-DOF manipulator system

k : spring stiffness of the simplified system

$\mathbf{k}$: gain vector of the asymptotic state-estimator

k_i : ith joint torsional spring stiffness of the 2-DOF manipulator system

$\mathbf{K}$: stiffness matrix of the 2-DOF manipulator system

$\mathbf{K}_2$: reduced stiffness matrix of the 2-DOF manipulator system

L_i : ith component of $\mathbf{k}$

m_i : ith body mass for the 2-DOF manipulator system

m_t : total mass of the 2-DOF manipulator system

M : mass of the single-mass system example

$\mathbf{M}(\mathbf{q}_r)$: inertia matrix for the 2-DOF manipulator system

M_1 : mass of the base or the spacecraft in the simplified system

M_{1p} : perturbed mass of the base for the simplified system

M_2 : mass of the payload in the simplified system

M_{2p} : perturbed mass of the payload in the simplified system

M_t : total mass of the simplified system

$\mathbf{N}(\mathbf{q}_r, \dot{\mathbf{q}}_r)$: expressions of Coriolis and centrifugal terms for the 2-DOF manipulator system

$N_d(A)$: describing function for the relay with a dead zone

$N_h(A)$: describing function for the relay with a dead zone and hysteresis

$\mathbf{q}$: vector of joint angles for the 2-DOF manipulator system

q_{2i-1} : angular position of the motor for joint i for the 2-DOF manipulator system

q_{2i} : angular position of the link for joint i for the 2-DOF manipulator system

$\mathbf{q}_r$: reduced vector of joint angles for the 2-DOF manipulator system

Q_i : generalized force corresponding to the joint angle q_i for the 2-DOF manipulator system

R : Rayleigh's dissipation function for the 2-DOF manipulator system

$R_f(t)$: rate of fuel consumption

T : total kinetic energy in the system for the 2-DOF manipulator system

T_m : kinetic energy of the rotors for the 2-DOF manipulator system

T_M : kinetic energy of the manipulator for the 2-DOF manipulator system

u : command of the thrusters, either $+1$, 0 or -1

V : total potential energy for the 2-DOF manipulator system

$w(t)$: output of the nonlinearity in the describing function method

$\mathbf{W}$: dynamic matrix for the 2-DOF manipulator system

$\mathbf{x}$: state vector for the simplified system

$\hat{\mathbf{x}}$: estimate of the state vector for the simplified system

$\tilde{\mathbf{x}}$: error in the estimate of the state vector for the simplified system

y_1 : position of the base or the spacecraft for the simplified system

$\hat{y}_1$: estimate of the position of the base or the spacecraft for the simplified system

y_2 : position of the payload for the simplified system

y_c : position of the centre of mass for the simplified system

y_{d1} : desired position of the base for the simplified system

y_f : relative displacement of the payload with respect to the base for the simplified system

β : ratio of the mass of the payload over the mass of the base for the simplified system

δ : attitude or dead zone limits

$\delta(\cdot)$: deviation from an operating point

Δ : amount of hysteresis included in the relay

$\Delta T_{\min}$: minimum operating time of the thrusters

λ : negative inverse of the slope of the switching lines, or the velocity gain

μ : equivalent reduced mass of the simplified system

ω : frequency of the sinusoidal input in the describing function method

ω_1 : first natural frequency for the 2-DOF manipulator system

ω_2 : second natural frequency for the 2-DOF manipulator system

ω_f : cutoff frequency of the second-order filter

ω_n : resonance frequency of the simplified system

ω_{se} : cutoff frequency of the differentiator-filter

σ_{motion} : variance of a stable motion

σ_{noise} : variance of the white noise

τ : time delay of the sensor reading

$\boldsymbol{\tau}$: joint torque vector for the 2-DOF manipulator system

τ_d : time delay due to the relay operation

τ_i : ith-joint applied torque for the 2-DOF manipulator system

ζ : damping ratio of the simplified system

ζ_f : damping ratio of the second-order filter

ζ_{se} : damping ratio of the differentiator-filter

Chapter 1

Introduction

1.1 Robots in Space

In the last few years, robotics have begun to play a very important role in space exploration and exploitation. Space robots are expected to become an increasingly vital part of future space operations. Not only will they be used for the assembly and fabrication of large space structures, but also for in-orbit service and repair activities. The mission cost and hazards of human orbital presence will therefore be reduced by minimizing the need for astronaut Extra Vehicular Activity (EVA).

The control of space manipulators presents various challenges. For example, the robot must be mounted on a free-floating base. Since robots are likely to carry very large payloads compared to the mass of the spacecraft, large disturbances may result at the base, thereby causing the robot to miss its target. Moreover, structural flexibility is present in space robots, as they are required to be light and to have large workspaces.

Currently, the only operational space manipulator available is the Space Shuttle CANADARM, which is a six-degree-of-freedom arm, weighing nearly 400 kg and 15 m long. This manipulator was designed by a Canadian team in cooperation with NASA, and is primarily used for deploying or retrieving satellites and space modules in orbit. A larger and more advanced version of the CANADARM is currently under design for the Space Station Freedom; this will be the contribution of Canada to this international project. This manipulator, called MSS, for Mobile Servicing System, will assist in the construction, operation and maintenance of the Space Station.

These two teleoperated manipulator systems are useful only for operation in Low Earth Orbit (LEO). However, we can imagine for the future a completely autonomous robot mounted on a spacecraft that will be able to go in a Geostationary Orbit (GEO) at 35,800 km from the Earth, pick up a satellite and bring it back to the Space Station for maintenance. As we can see, there are many possibilities for robots in space, which is why extensive research is currently being conducted to further improve and develop new technologies in this new field of robotics.

1.2 Literature Survey

1.2.1 Dynamics and Control

The kinematics, dynamics, and control of space robotic manipulators are much more complicated than their counterparts on Earth due to the dynamic coupling between the manipulators and their spacecraft. Several control schemes have been proposed for such systems. Most of them assume that the manipulator moves sufficiently slow to neglect the flexibility in drives, shafts, links, and gear transmissions. These control methods can be classified in three major categories. In the first one, the position and the orientation of the spacecraft is controlled by jet thrusters and reaction wheels, or a combination of both, to compensate for any manipulator dynamic forces exerted on the spacecraft. The base of the manipulator thus being of a free-flying type. In this case, the spacecraft is kept almost stationary, the control methods for ground-fixed robots thus being applicable. The kinematic problem is consequently relatively simple. However, the use of these control methods is limited, due to the relatively high fuel requirements and the possibility to saturate the reaction-jet system (Dubowsky, Vance and Torres, 1989). To minimize these problems, Nenchev, Umetani and Yoshida (1992) and Quinn, Chen and Lawrence (1994) studied motions of the manipulator arm that do not disturb the attitude of the spacecraft. With the same objective, Torres and Dubowsky (1992) developed an Enhanced Disturbanced Map (EDM) used to suggest paths for a given manipulator that result in low-attitude fuel consumption.

In the second category, reaction wheels or jet thrusters are used to control the attitude only. The centre of mass of the spacecraft, however, is still free to translate in response to the force disturbances from the robot and its payload. This is an interesting approach, since reaction wheels can be used, thereby reducing the fuel consumption while keeping fixed the attitude when necessary, as for antennae pointing towards the Earth. Unfortunately, the control problem is obviously more complicated than in the first category because the relative disturbance translation of the payload with respect to the spacecraft must be taken into account. This problem was addressed in (Longman, Lindberg and Zedd, 1987) by developing a new kind of robot kinematics that adjusts the joint angle command to account for the base motion. As well, a method to obtain the reaction moment needed to cancel all attitude disturbances to the spacecraft was established, without recourse to a full dynamic analysis of the robot. A technique called the Virtual Manipulator, is available to simplify the control problem. This technique, presented in (Vafa and Dubowsky, 1987; Vafa and Dubowsky, 1990a,b), defined a virtual manipulator that combines the kinetic and dynamic properties of the manipulator and the spacecraft. This virtual manipulator is used in (Vafa and Dubowsky, 1987; Vafa and Dubowsky, 1990a) to develop a numerical approach to solve the inverse kinematic problem when the orientation of the spacecraft is controlled. The inverse kinematic problem is also solved in (Longman, Lindberg and Zedd, 1987; Lindberg, Longman and Zedd, 1990) for an elbow manipulator like the CANADARM.

In the third category, the free-floating case, no actuators are used to control the position and orientation of the spacecraft. Therefore, the spacecraft is free to move in response to the manipulator motion. This control scheme has the advantages that no fuel is required to control the spacecraft and that the risk of collision of the robot end-effector with an object about to be grasped, resulting from the attitude control thrusters suddenly firing, is eliminated. However, path planning becomes much more complicated than before, because the platform is floating and, therefore, as shown in (Lindberg, Longman and Zedd, 1990), the position of the robot end-effector is no longer a function of the present robot joint angles, but rather of the whole history of these joint angles. The inverse kinetics problem (instead of inverse kinematics for ground-fixed robots) is very complicated and generally has an infinite number of solutions. Longman (1990b) developed one of these solutions for the free-floating case at hand. Despite the complicated dynamics, Papadopoulos and Dubowsky (1991b) suggested that nearly any control algorithm that can be used for fixed-based manipulators can also be implemented for free-floating space robots with a few additional conditions. Alexander and Cannon (1990) developed control methods that achieved accurate end-effector control in spite of the free dynamic response of the vehicle to arm motion, using resolved-acceleration control. Umetani and Yoshida (1989) developed a similar control algorithm, but with the use of resolved-rate control.

Since the attitude control system of the spacecraft does not operate during this mode of space manipulation, this mode becomes feasible when no external forces and torques act on the system and when its total momentum is negligible (Papadopoulos and Dubowsky, 1991b). Therefore, the robot workspace is reduced because the centre of mass of the system will remain fixed under these assumptions. The workspace is also reduced due to the existence of dynamic singularities (Papadopoulos and Dubowsky, 1993), which are not present in Earth-bound robots. To achieve an unlimited workspace, a control scheme that switches between a free-floating mode and a mode in which the system is treated as a redundant manipulator with a pseudo-inverse Jacobian-based controller is derived in (Spofford and Akin, 1990). In the last three control schemes, the end-effector is able to track a desired path while the spacecraft floats freely in a noncoordinated way.

Using the inherent redundancy in free-flying space robotic systems, it is possible to guarantee coordinated motion of the spacecraft and the end-effector without use of special compensating devices, as shown in (Nenchev, Umetani and Yoshida, 1992). Also, Vafa and Dubowsky (1987; 1990b) have shown, using the virtual manipulator approach, that the manipulator itself can correct the position and attitude of the spacecraft through small cyclic motions in joint space. Based on this idea and using the nonholonomic mechanical structure of space vehicle-manipulator systems, Nakamura and Mukherjee (1991) proposed a path-planning scheme to control both the vehicle orientation and the manipulator joints by actuating only the latter. In another study, a coordinated controller was designed to control both the spacecraft and the end-effector, and allowing the command of a desirable manipulator configuration and the planning of a system motion with the use of thrusters (Papadopoulos and Dubowsky, 1991a).

In all previous control schemes reported, no analysis has been performed that includes the actual flexibility of space robotic systems. In fact, one might presume the vibrations of the robot arm will only induce attitude oscillations for the spacecraft and that, after these vibrations are damped, the spacecraft attitude would be the same as directed from the reaction moment compensation torques derived for a rigid-body model in (Longman, Lindberg and Zedd, 1987). However, Longman (1990a) showed that such a presumption is false and that the most common situation is that the structural vibrations of the robot arm will try to tumble the spacecraft. Longman developed a general formulation to determine the satellite attitude control torque required to counteract robot motion disturbances that include the effects of robot flexibility.

1.2.2 Flexible Spacecraft Controlled by On-Off Thrusters

The control schemes introduced in Subsection 1.2.1 that require thrusting actions assume the use of reaction jets that provide forces and torques proportional to the commanded control input. Unfortunately, this is never the case in space, since such technology is still not applicable and only on-off thrusters can be used to control the position and attitude of the spacecraft (Anthony, Wie and Carroll, 1990). These on-off thrusters are nonlinear devices, the design of a control system becoming a very difficult problem when flexible modes must be controlled.

Currently, the common approach to the design of control systems using on-off devices is to consider single-axis rigid-body motion and to define a switching logic for a single set of thrusters by the use of phase plane analyses. The optimal-fuel problem for this kind of rigid-body motion appears in many textbooks (Bryson and Ho, 1975). However, the actual space structures are likely to be flexible and their control using these nonlinear devices may interact with the structural modes and create instabilities that can be manifested as limit cycles (Millar and Vigneron, 1979).

Many researchers addressed the problem of controlling a flexible spacecraft using on-off thrusters. Wie and Plescia (1984) designed an on-off pulse modulator attitude control system using the describing function analysis. They used the relative stability margin, with respect to the limit cycle condition of a structural mode, as a measure of the robustness of the nonlinear control system. Using the same idea, Anthony, Wie and Carroll (1990) showed that the describing function analysis can be utilized for practical control design problems such as flexible spacecraft equipped with pulse-modulated reaction jets. Hablani (1992) developed a method to optimize the pulse-width of the thrusters for fast active damping of flexible modes, without destabilizing the rigid-body modes. Adaptive bandpass filters were used to obtain an accurate measure of the mode frequency, which was known imprecisely before. Assuming that control moment gyros or other internal mechanisms were available for proportional fine control, Nakano and Willms (1982) developed an open-loop control scheme using only three switching times for rest-to-rest manoeuvres. These switching times were chosen to minimize residual elastic energy at the end of the reorientation. On the other hand, Vander Velde and He (1983) implemented the phase plane approach to design a control system for a flexible space structure of any order, while using any number of thrusters, based on an approximation to an optimal control formulation.

Unfortunately, all these methods assume a precomputed exact or approximate knowledge of the flexible modes. For a space robotic system, or for a multitask servicer as the Space Shuttle, the natural frequencies are always changing with the robot configuration or the payload carried. Therefore, these control methods are very difficult to implement and more research is needed.

1.2.3 Payload-Attitude Controller Interaction

The Space Shuttle Reaction Control System (RCS) is similar to the one that flew in Apollo missions. It evolved under the assumption that the Orbiter is sufficiently rigid to allow the use of rigid-body mechanics in the description of Orbiter response to RCS activity (Sackett and Kirchwey, 1982). No special attention was taken to include structural flexibility in the RCS design that is described in (Hattis, 1982; Sackett and Kirchwey, 1982; Nakano and Willms, 1982). However, at the time of payload deployment, with or without the CANADARM system, flexibility becomes important. The structural modes can have rather low frequencies and can be excited by the RCS activity. Sackett and Kirchwey (1982) looked at the performance degradation of the RCS due to the deployment of a flexible payload by various means. They grouped these dynamic interaction possibilities in order of increasing severity:

1. control effects — flexibility either induced additional firings or omitted some of these;

2. structural motion and load response to typical, aperiodic jet firings;

3. structural resonance due to periodic jet firing caused by rigid-body Flight Control System (FCS) response to disturbance accelerations;

4. closed-loop instability, where RCS firings cause flexure, which passes through the Inertial Measurements units (IMU) and state estimator causing RCS firings, which reinforces flexure and continues to eventually reach a limit cycle.

After conducting extensive simulations, they concluded that the judicious selection of control parameter values and careful operational procedures, based on a knowledge of the payload structural characteristics, can reduce dynamic interactions and load problems. Penchuk, Hattis and Kubiak (1985) used the describing function method to analyze the problem of a payload deployed by means of a tilt table with a pivot near the aft end of the Space Shuttle. Stability maps were obtained and compared to simulation results to validate the describing function analysis. In (Redding and Adams, 1987), a new attitude controller based on fuel-optimal manoeuvres was developed for the Space Shuttle, while Kubiak and Martin (1983) developped a new design for the RCS to reduce the impact of large measurement uncertainties in the rate signal during attitude control. In both cases, the performance of the RCS is increased significantly for rigid-body motion. However, they did not deal with the flexibility problem and only mentioned that by diminishing the required firings, the likelihood to cause structural problems diminishes.

1.3 Problem Formulation and Objectives

As mentioned in Section 1.1, space manipulators are structurally flexible mechanical systems. When the free-flying base of the manipulator is controlled by the use of on-off thrusters, which produce a rather broad frequency spectrum that can excite sensitive modes of the flexible system, dynamic interactions are likely to occur. The excitation of these modes can introduce further disturbances to the attitude control system, and therefore, undesirable fuel replenishing limit cycles may develop.

In those cases, thrusters are firing without stabilizing the base and a lot of fuel is consumed for almost nothing. Since fuel is an unavailable resource in space, the consequences of such interactions can be very problematic. In the case where the natural frequencies are dependent upon the payload and the configuration of the system, as for a free-flying robot, the current method for resolving these problems is to perform extensive simulations to examine the possibilities for dynamic interactions. If these occur, corrective actions are taken, which would include adjusting the RCS parameter values, or simply changing the operational procedures (Sackett and Kirchwey, 1982; Penchuk, Hattis and Kubiak, 1985). Hence, classical attitude controllers must be improved to reduce these dynamic interaction possibilities.

In this thesis, it is intended to model the foregoing problems for a general space manipulator mounted on a free-flying base controlled by on-off thrusters, and to develop control methods to reduce these undesired effects. Approximate CANADARM flexible modes are used to make the model behaviour more realistic; however, the analysis is not restricted to this robotic system. The dynamic interactions are modelled for the worst case that can occur, i.e. when the system is limit cycling. Since the describing function method has been shown to be helpful for such nonlinear systems (Wie and Plescia, 1984; Anthony, Wie and Carroll, 1990; Penchuk, Hattis and Kubiak, 1985), this method is used in a parametric study to find the system parameters that affect system performance. Using these results, design guidelines are presented for various control schemes, and based on this knowledge, control methods that are intented to reduce the undesired effects are then developed. Simulation models are used to confirm results obtained by the describing function analysis and to examine cases to which describing function analysis does not apply, as for the addition of white noise in the system.

1.4 Thesis Organization

A resonance frequency analysis is performed in Chapter 2 for a two-flexible-joint space manipulator system. Thereafter, an approximate model is derived to simplify the analysis problem, and finally, various methods for nonlinear system analysis are briefly described. Chapter 3 is devoted to the control problem. First, a classical spacecraft attitude controller using phase plane techniques is introduced. A single-rigid-mass system is used to show the function of the controller. The effects of hysteresis and time delays are briefly studied. Finally, alternative control systems used in simulation studies are formulated, and are followed by the stability definition used in this thesis. In Chapter 4, values are chosen for all parameters in the models studied. The describing function technique is used to perform a parametric study and to construct stability maps, used to draw conclusions. Some simulation results are introduced to confirm the validity of the describing function studies. The importance of hysteresis and the effects of noise on the system are also discussed in Chapter 4 by the use of simulation. Finally the influence of perturbed mass properties into a particular model studied are investigated. Chapter 5 concludes the thesis by summarizing the results of this study, and then outlining some recommendations for future work.

Chapter 2

Modelling and Analysis of Space Robots

2.1 Introduction

As mentioned in Section 1.1, the CANADARM, shown in Fig. 2.1, is the only operational space manipulator. One limitation of this system is that it can work only within its own reach, thereby requiring very long links to have a large workspace. To avoid this problem, free-flying robots are currently being studied and will grab, dock and manipulate while in orbit. Two interesting concepts are the U.S. Flight Telerobotic Servicer (FTS) shown in Fig. 2.2(a), and the Japan NASDA OSV of Fig. 2.2(b). Such free-flying systems are to be equipped with thrusters, manipulators, several visual sensors, a high-gain antenna, and a docking mechanism. Also, they are to be teleoperated from Earth or from orbit through a satellite link.

All three systems presented above have the common feature that they are working in a zero-gravity environment. The dynamic modelling and control of such systems are therefore much more complicated than for fixed-base robots. Moreover, structural and joint flexibility is likely to be important in space robots, as they are required to be lightweight, move large payloads and/or have large workspaces, thereby increasing

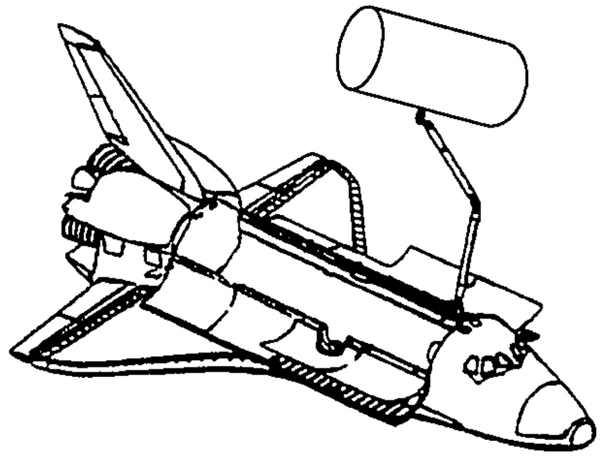

Figure 2.1: The CANADARM mounted on the Space Shuttle.

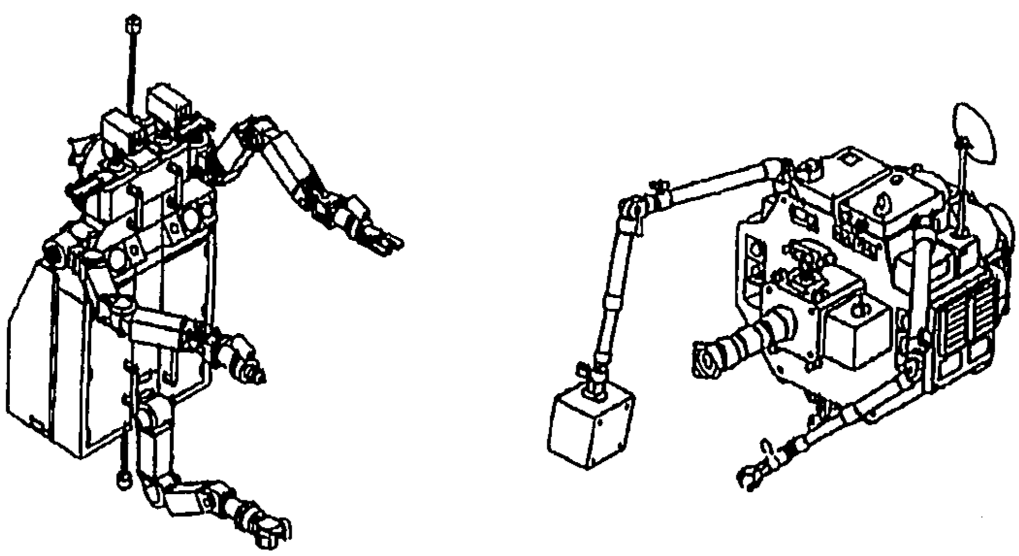

(a) (b)

Figure 2.2: Two concepts of free-flying robots. (a) U.S. Flight Telerobotic Servicer (FTS), (b) Japan NASDA OSV.

the complexity of the modelling and control problem. To simplify the analysis, the dynamic modelling presented in the next section is restricted to a two-flexible-joint planar manipulator mounted on a 3-DOF spacecraft. This approximation is legitimate since in the case of a free-flyer, as those of Fig. 2.2, they are likely to have reduced structural flexibility but will have joint compliance which becomes important when payload are big. In the case of the CANADARM, both structural and joint flexibility is present but the latter is more important than the former. It can also be assumed that all flexibility in the system are lumped at the joints. In Section 2.3, a two-DOF simplified model where the frequency characteristics are chosen to match those of the manipulator studied in Section 2.2 is introduced. Since the use of on-off thrusters is assumed in this thesis, analysis methods for nonlinear systems are discussed in Section 2.4.

2.2 System Description: 2-DOF Planar Manipulator on a 3-DOF Spacecraft

2.2.1 Manipulator Equations of Motion

In this section, the dynamics model of a two-flexible-joint planar manipulator mounted on a free-floating base is developed using the Lagrangian formulation. In this case, free-floating operations are assumed, which means that no thruster or external force act on the system. It is intended to obtain the general expressions for the natural frequencies of this free-floating system. The manipulator under study is shown in Fig. 2.3, each flexible-joint being modelled as a torsional spring in parallel with a torsional dashpot, both lumped in a mechanical coupling, as shown in Fig. 2.4. The angle q_{2i-1} represents the angular position of the motor for joint i, while the angle q_{2i} is the angular position of the link for the same joint. Angles q_{2i-1} and q_{2i} are measured relative to a reference line fixed to link $i-1$.

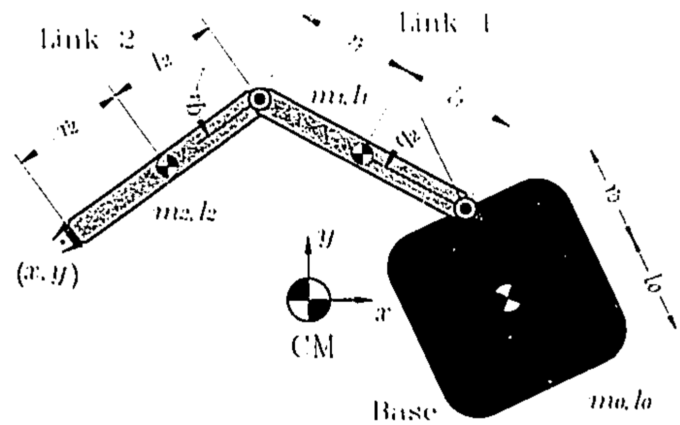

Figure 2.3: A planar free-floating manipulator system.

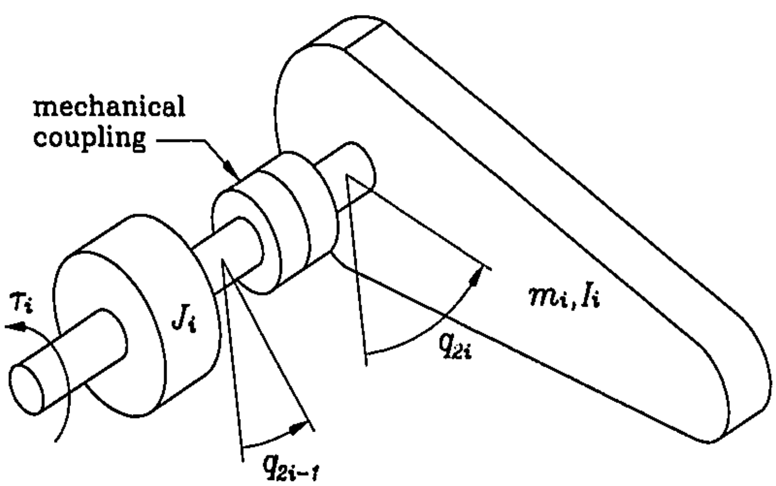

Figure 2.4: A flexible-joint model.

The system centre of mass (CM) can be chosen as the inertial origin, since, under the assumptions of free-floating operation, i.e., in the absence of external forces and of zero initial momentum, the CM remains fixed in inertial space. Also, under these assumptions, the angular momentum with respect to the system CM is constant. As explained in (Papadopoulos and Dubowsky, 1991b), we can further assume that, during free-floating operations, the system momentum is zero. If momentum accumulates, the system may operate for a limited period of time. In practice, the control system of the attitude of the spacecraft would be turned on and perform a momentum dump manoeuvre in order to eliminate any accumulated momentum (Papadopoulos, 1990). From the conservation of angular momentum, the spacecraft angular velocity can be expressed as a function of the reduced vector of joint angles ($\mathbf{q}_r$) and their time-rates of change ($\dot{\mathbf{q}}_r$), where $\mathbf{q}_r$ is defined as

$$\mathbf{q}_r \equiv [q_2, q_4]^T \,. \tag{2.1}$$

Therefore, the manipulator kinetic energy T_M can be expressed as a function of $\mathbf{q}_r$ and $\dot{\mathbf{q}}_r$ only, and is given in (Papadopoulos and Dubowsky, 1991b) as

$$T_M = \frac{1}{2}\dot{\mathbf{q}}_r^T \mathbf{H}^*(\mathbf{q}_r)\dot{\mathbf{q}}_r \tag{2.2}$$

where $\mathbf{H}^*(\mathbf{q}_r)$ is the reduced inertia matrix. For the simple planar case at hand, the system inertia is of the form

$$\mathbf{H}^*(\mathbf{q}_r) = \begin{bmatrix} d_{11} + 2d_{12} + d_{22} - \dfrac{(D_1 + D_2)^2}{D} & d_{12} + d_{22} - \dfrac{D_2(D_1 + D_2)}{D} \\ d_{12} + d_{22} - \dfrac{D_2(D_1 + D_2)}{D} & d_{22} - \dfrac{D_2^2}{D} \end{bmatrix} \tag{2.3}$$

where

$$\begin{aligned} d_{00} &= I_0 + \frac{m_0(m_1 + m_2)}{m_t} r_0^2 \\ d_{10} &= \frac{m_0 r_0}{m_t}\Big[l_1(m_1 + m_2) + r_1 m_2\Big]\cos(q_2) = d_{01} \\ d_{20} &= \frac{m_0 m_2}{m_t} r_0 l_2 \cos(q_2 + q_4) = d_{02} \\ d_{11} &= I_1 + \frac{m_0 m_1}{m_t} l_1^2 + \frac{m_1 m_2}{m_t} r_1^2 + \frac{m_0 m_2}{m_t}(l_1 + r_1)^2 \end{aligned}$$

$$\begin{aligned}
d_{21} &= \left[\frac{m_1 m_2}{m_t} r_1 l_2 + \frac{m_0 m_2}{m_t} l_2 (l_1 + r_1)\right] \cos(q_4) = d_{12} \\
d_{22} &= I_2 + \frac{m_2(m_0 + m_1)}{m_t} l_2^2 \\
D_j &\equiv \sum_{i=0}^{2} d_{ij}, \qquad j = 0, 1, 2 \\
D &\equiv D_0 + D_1 + D_2
\end{aligned} \tag{2.4}$$

where m_i and I_i $(i = 0, 1, 2)$ are the ith body mass and moment of inertia with respect to the centre of mass of the corresponding link, l_i and r_i $(i = 0, 1, 2)$ are defined in Fig. 2.3, and m_t is the total mass of the system, given by $m_t = m_0 + m_1 + m_2$. All d_{ij}, D_j and D are expressed in frame 0, i.e., in the frame attached to the base.

The kinetic energy of the rotors, T_m, is

$$T_m = \frac{1}{2} J_1 \dot{q}_1^2 + \frac{1}{2} J_2 \dot{q}_3^2 \tag{2.5}$$

where J_i, for $i = 1, 2$, is the moment of inertia of motor i about its axis of rotation, which is assumed to contain the mass centre of the rotor. The total kinetic energy of the system is, therefore,

$$T = T_M + T_m \; . \tag{2.6}$$

In the absence of gravity, the potential energy in the system is only due to joint flexibility. Assuming direct drives, this potential energy can be written as

$$V = \frac{1}{2} k_1 (q_2 - q_1)^2 + \frac{1}{2} k_2 (q_4 - q_3)^2 \; , \tag{2.7}$$

where k_i $(i = 1, 2)$ is the torsional spring stiffness of joint i.

Viscous friction forces due to damping at each joint can be taken into account by using Rayleigh's dissipation function R, as discussed in (Goldstein, 1980)

$$R = \frac{1}{2} c_1 (\dot{q}_2 - \dot{q}_1)^2 + \frac{1}{2} c_2 (\dot{q}_4 - \dot{q}_3)^2 \; , \tag{2.8}$$

where c_i $(i = 1, 2)$ is the damping coefficient of joint i.

The system dynamical equations are obtained from the Euler-Lagrange equation

$$\frac{d}{dt}\left(\frac{\partial T}{\partial \dot{q}_j}\right) - \frac{\partial T}{\partial q_j} + \frac{\partial V}{\partial q_j} = Q_j - \frac{\partial R}{\partial \dot{q}_j}, \qquad j = 1, 2, 3, 4 \tag{2.9}$$

where Q_j is the generalized force corresponding to the joint angle q_j. In this case, Q_j is equal to the torque applied by the motor for $j = 1$ and 3, and is zero for $j = 2$ and 4. Therefore, applying Eq.(2.9) to the kinetic energy given by Eq.(2.6), the potential energy given by Eq.(2.7) and Rayleigh's dissipation function given by Eq.(2.8), results in a set of four scalar dynamics equations of the form

$$\mathbf{M}(\mathbf{q}_r)\ddot{\mathbf{q}} + \mathbf{N}(\mathbf{q}_r, \dot{\mathbf{q}}_r)\dot{\mathbf{q}} + \mathbf{C}\dot{\mathbf{q}} + \mathbf{K}\mathbf{q} = \boldsymbol{\tau} \tag{2.10}$$

where,

$$\mathbf{q} = \begin{bmatrix} q_1 \\ q_2 \\ q_3 \\ q_4 \end{bmatrix}, \qquad \boldsymbol{\tau} = \begin{bmatrix} \tau_1 \\ 0 \\ \tau_2 \\ 0 \end{bmatrix}$$

$$\mathbf{M}(\mathbf{q}_r) = \begin{bmatrix} J_1 & 0 & 0 & 0 \\ 0 & d_{11} + 2d_{12} + d_{22} - \dfrac{(D_1 + D_2)^2}{D} & 0 & d_{12} + d_{22} - \dfrac{D_2(D_1 + D_2)}{D} \\ 0 & 0 & J_2 & 0 \\ 0 & d_{12} + d_{22} - \dfrac{D_2(D_1 + D_2)}{D} & 0 & d_{22} - \dfrac{D_2^2}{D} \end{bmatrix}$$

$$\mathbf{C} = \begin{bmatrix} c_1 & -c_1 & 0 & 0 \\ -c_1 & c_1 & 0 & 0 \\ 0 & 0 & c_2 & -c_2 \\ 0 & 0 & -c_2 & c_2 \end{bmatrix}$$

$$\mathbf{K} = \begin{bmatrix} k_1 & -k_1 & 0 & 0 \\ -k_1 & k_1 & 0 & 0 \\ 0 & 0 & k_2 & -k_2 \\ 0 & 0 & -k_2 & k_2 \end{bmatrix}$$

$$\mathbf{N}(\mathbf{q}_r, \dot{\mathbf{q}}_r) = \begin{bmatrix} 0 & 0 & 0 & 0 \\ 0 & N_{11}(\mathbf{q}_r, \dot{\mathbf{q}}_r) & 0 & N_{12}(\mathbf{q}_r, \dot{\mathbf{q}}_r) \\ 0 & 0 & 0 & 0 \\ 0 & N_{21}(\mathbf{q}_r, \dot{\mathbf{q}}_r) & 0 & N_{22}(\mathbf{q}_r, \dot{\mathbf{q}}_r) \end{bmatrix}$$

where $N_{ij}(\mathbf{q}_r, \dot{\mathbf{q}}_r)$, for $i = 1,2$; $j = 1,2$, are expressions of Coriolis and centrifugal terms that are included in Appendix A.

2.2.2 Manipulator Natural Frequencies

In this section, general expressions for the manipulator natural frequencies are derived. To perform this frequency analysis, the joints are locked in a specific configuration, the motion then being analyzed around this position.

Let us define

$$\delta q_2 = q_2 - q_1 \tag{2.11a}$$

$$\delta q_4 = q_4 - q_3 \; . \tag{2.11b}$$

Since brakes are applied and there is no rotation of the motor shafts, i.e. q_1 and q_3 are constant, we have

$$\delta \dot{q}_2 = \dot{q}_2 \tag{2.12a}$$

$$\delta \dot{q}_4 = \dot{q}_4 \tag{2.12b}$$

$$\delta \ddot{q}_2 = \ddot{q}_2 \tag{2.12c}$$

$$\delta \ddot{q}_4 = \ddot{q}_4 \; . \tag{2.12d}$$

Using Eqs.(2.11) and (2.12), and linearizing about an operating point, where second-order terms can be neglected, Eq.(2.10) can be written as

$$\begin{bmatrix} J_1 & 0 & 0 & 0 \\ 0 & d_{11} + 2d_{12} + d_{22} - \dfrac{(D_1 + D_2)^2}{D} & 0 & d_{12} + d_{22} - \dfrac{D_2(D_1 + D_2)}{D} \\ 0 & 0 & J_2 & 0 \\ 0 & d_{12} + d_{22} - \dfrac{D_2(D_1 + D_2)}{D} & 0 & d_{22} - \dfrac{D_2^2}{D} \end{bmatrix} \begin{bmatrix} 0 \\ \delta \ddot{q}_2 \\ 0 \\ \delta \ddot{q}_4 \end{bmatrix}$$
$$+ \begin{bmatrix} -c_1 \delta \dot{q}_2 \\ c_1 \delta \dot{q}_2 \\ -c_2 \delta \dot{q}_4 \\ c_2 \delta \dot{q}_4 \end{bmatrix} + \begin{bmatrix} -k_1 \delta q_2 \\ k_1 \delta q_2 \\ -k_2 \delta q_4 \\ k_2 \delta q_4 \end{bmatrix} = \begin{bmatrix} \tau_1 \\ 0 \\ \tau_2 \\ 0 \end{bmatrix} . \tag{2.13}$$

The first and third equation of Eq.(2.13) give the expressions for the required torque to brake the joints, and the second and fourth equation describe the motion around the operating point. This second set of equations can be written as

$$\mathbf{H}^{*}(\mathbf{q}_r)\delta\ddot{\mathbf{q}} + \mathbf{C}_2\delta\dot{\mathbf{q}} + \mathbf{K}_2\delta\mathbf{q} = \mathbf{0} \tag{2.14}$$

where,

$$\delta\mathbf{q} = [\delta q_2, \delta q_4]^T$$

$$\mathbf{C}_2 = \begin{bmatrix} c_1 & 0 \\ 0 & c_2 \end{bmatrix}$$

$$\mathbf{K}_2 = \begin{bmatrix} k_1 & 0 \\ 0 & k_2 \end{bmatrix}$$

and $\mathbf{H}^{*}(\mathbf{q}_r)$ is defined in Eq.(2.3). Note that J_1 is included in I_0, and J_2 in I_1, since the brakes are applied and the inertia of a motor rotor becomes part of that of a previous link, assuming that the motor is at the joint and that direct drive is used.

The natural frequencies of the system are given by the square roots of the eigenvalues of the dynamic matrix $\mathbf{W}$, which is defined as

$$\mathbf{W} \equiv \mathbf{H}^{*}(\mathbf{q}_r)^{-1}\mathbf{K}_2 \ . \tag{2.15}$$

$\mathbf{H}^{*}(\mathbf{q}_r)$ is nonsingular, since it is a positive-definite matrix. Finally, the natural frequencies ω_1 and ω_2 are given by

$$\omega_1 = \sqrt{\frac{H_{11}k_2 + H_{22}k_1 - \sqrt{(H_{11}k_2 - H_{22}k_1)^2 + 4H_{12}^2k_1k_2}}{2(H_{11}H_{22} - H_{12}^2)}} \tag{2.16a}$$

$$\omega_2 = \sqrt{\frac{H_{11}k_2 + H_{22}k_1 + \sqrt{(H_{11}k_2 - H_{22}k_1)^2 + 4H_{12}^2k_1k_2}}{2(H_{11}H_{22} - H_{12}^2)}} \tag{2.16b}$$

where H_{ij} is the (i, j) component of $\mathbf{H}^{*}(\mathbf{q}_r)$. Since we assumed small motions when we linearized, the angle values can be chosen as $q_2 = q_1$ and $q_4 = q_3$. If we are given the known natural frequencies of a manipulator for a specific configuration, then the corresponding spring stiffnesses k_1 and k_2 at each joint can be determined from

Eqs.(2.16). Thereafter, using these computed spring stiffness values, the manipulator natural frequencies for other configurations can be approximated with Eqs.(2.16).

2.2.3 Cartesian Space vs. Joint Space

In the previous subsection, the natural-frequency expressions for a general two-flexible-joint planar manipulator were derived using the joint equations of motion. Therefore, by working in the joint space, these frequencies correspond to the joint oscillations. However, it will be shown in this subsection that these frequencies are actually the same as the ones corresponding to the oscillations of the end-effector (in Cartesian space). Thus, the frequency expressions Eqs.(2.16) can be used to describe the frequency content of a payload attached to the end-effector.

Cartesian velocities are related to joint velocities by the Jacobian matrix $\mathbf{J}(\mathbf{q}_r)$, namely,

$$\dot{\mathbf{x}} = \mathbf{J}(\mathbf{q}_r)\dot{\mathbf{q}}_r \ . \tag{2.17}$$

In this case, we have

$$\begin{bmatrix} \delta\dot{x} \\ \delta\dot{y} \end{bmatrix} = \begin{bmatrix} J_{11} & J_{12} \\ J_{21} & J_{22} \end{bmatrix} \begin{bmatrix} \delta\dot{q}_2 \\ \delta\dot{q}_4 \end{bmatrix} \tag{2.18}$$

where J_{ij} can be considered constant, since we are dealing with small motions.

If the first and second natural frequencies are ω_1 and ω_2, we can write

$$\delta q_2 = Z_1 \sin(\omega_1 t) \tag{2.19a}$$

$$\delta q_4 = Z_2 \sin(\omega_2 t) \ . \tag{2.19b}$$

where Z_1 and Z_2 are constant.

Differentiating Eqs.(2.19), we obtain

$$\delta\dot{q}_2 = Z_1\omega_1 \cos(\omega_1 t) \tag{2.20a}$$

$$\delta\dot{q}_4 = Z_2\omega_2 \cos(\omega_2 t) \ . \tag{2.20b}$$

Substituting Eqs.(2.20) in Eq.(2.18), we obtain

$$\delta\dot{x} = J_{11}Z_1\omega_1\cos(\omega_1 t) + J_{12}Z_2\omega_2\cos(\omega_2 t) \tag{2.21}$$

$$\delta\dot{y} = J_{21}Z_1\omega_1\cos(\omega_1 t) + J_{22}Z_2\omega_2\cos(\omega_2 t)\ . \tag{2.22}$$

Therefore, the frequency content of $\delta\dot{x}$ and $\delta\dot{y}$ is ω_1 and ω_2, and thus, the natural frequencies in the Cartesian space are the same as those in the joint space.

2.3 Two-DOF Simplified Model Plant

2.3.1 Model Description

The dynamics of a simple two-flexible-joint planar manipulator is rather complicated; it is preferable to employ a simplified model to analyze the problem stated in Section 1.3. We can replace the manipulator of Fig. 2.5(a) with an equivalent spring-and-dashpot system, as shown in Fig. 2.5(b). By a proper selection of the spring stiffness k and the damping coefficient c, the resonance frequency of the simplified system can be matched to the first one of the original system. Therefore, a similar relative motion of the payload with respect to the base can be obtained.

In this thesis, the two-flexible-joint manipulator model will be used to find the resonance frequencies of the manipulator for a specific payload and configuration. Then, by introducing suitable values for k and c into the simplified model of Fig. 2.5(b), the first natural frequency of the original system will be matched.

2.3.2 Model Formulation

In this section, the equations of motion for the simplified system are derived. These equations are written in various forms and will be used in the simulation models that are derived in Chapter 3.

The equations of motion for the system shown in Fig. 2.6 can be written directly

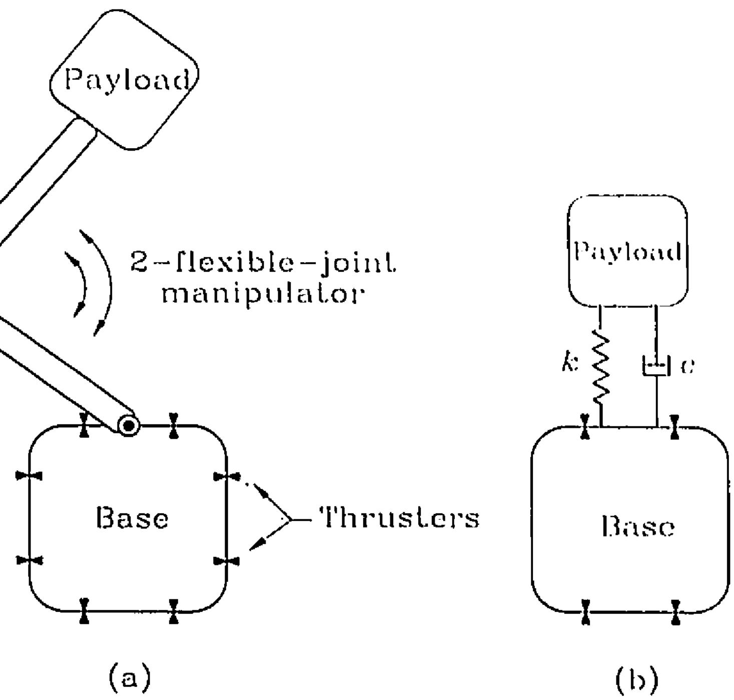

Figure 2.5: Manipulator replacement by a spring and a dashpot: (a) Two-link manipulator; (b) Simplified two-mass system.

as

$$M_1\ddot{y}_1 + c(\dot{y}_1 - \dot{y}_2) + k(y_1 - y_2) = Bu \tag{2.23a}$$

$$M_2\ddot{y}_2 - c(\dot{y}_1 - \dot{y}_2) - k(y_1 - y_2) = 0\ , \tag{2.23b}$$

where M_1 is the mass of the base, M_2 the mass of the payload, y_1 the position of the base, y_2 the position of the payload, k the spring stiffness, c the damping coefficient, B the amplitude of the force developed by the thrusters and u is the command of the thrusters, either +1, 0 or −1.

In order to write the system equations in state-space form, the following variables are defined:

$$x_1 = y_1 \tag{2.24a}$$

$$x_2 = \dot{y}_1 \tag{2.24b}$$

$$x_3 = y_2 \tag{2.24c}$$

$$x_4 = \dot{y}_2\ . \tag{2.24d}$$

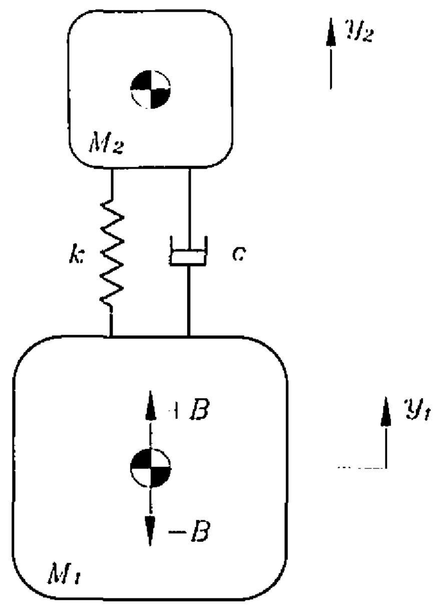

Figure 2.6: A two-mass system.

Using Eqs.(2.24), Eqs.(2.23) can be written as

$$\dot{x}_1 = x_2 \tag{2.25a}$$

$$\dot{x}_2 = \frac{1}{M_1}\Big[-c(x_2 - x_4) - k(x_1 - x_3) + Bu\Big] \tag{2.25b}$$

$$\dot{x}_3 = x_4 \tag{2.25c}$$

$$\dot{x}_4 = \frac{1}{M_2}\Big[c(x_2 - x_4) + k(x_1 - x_3)\Big] \ . \tag{2.25d}$$

If we define the state vector as $\mathbf{x} = [x_1, x_2, x_3, x_4]^T$, Eqs.(2.25) can be written in state-variable form as

$$\dot{\mathbf{x}} = \mathbf{A}\mathbf{x} + \mathbf{b}u \tag{2.26}$$

where

$$\mathbf{A} = \begin{bmatrix} 0 & 1 & 0 & 0 \\ -k/M_1 & -c/M_1 & k/M_1 & c/M_1 \\ 0 & 0 & 0 & 1 \\ k/M_2 & c/M_2 & -k/M_2 & -c/M_2 \end{bmatrix}, \qquad \mathbf{b} = \begin{bmatrix} 0 \\ B/M_1 \\ 0 \\ 0 \end{bmatrix} .$$

If the required output is y_1, then one can write

$$y_1 = \mathbf{c}^T\mathbf{x} \tag{2.27}$$

with

$$\mathbf{c} = \begin{bmatrix} 1 & 0 & 0 & 0 \end{bmatrix}^T .$$

The overall motion of the system can be decomposed into a rigid-body motion of the system centre of mass and a flexible-body motion around the centre of mass. The equations governing these two motions are now derived.

The position of the centre of mass is given by

$$y_c = \frac{M_1 y_1 + M_2 y_2}{M_1 + M_2} \tag{2.28}$$

and hence,

$$\ddot{y}_c = \frac{M_1 \ddot{y}_1 + M_2 \ddot{y}_2}{M_1 + M_2} \tag{2.29}$$

which can be written as

$$M_t \ddot{y}_c = M_1 \ddot{y}_1 + M_2 \ddot{y}_2 \tag{2.30}$$

where the total mass of the system is

$$M_t = M_1 + M_2 . \tag{2.31}$$

Adding Eqs.(2.23a) and (2.23b), we obtain

$$M_1 \ddot{y}_1 + M_2 \ddot{y}_2 = Bu . \tag{2.32}$$

Inserting Eq.(2.32) into Eq.(2.30), we obtain

$$M_t \ddot{y}_c = Bu . \tag{2.33}$$

This equation governs the motion of the system centre of mass.

Conversely, subtracting Eq.(2.23b) from Eq.(2.23a), we obtain

$$M_1 \ddot{y}_1 - M_2 \ddot{y}_2 + 2c(\dot{y}_1 - \dot{y}_2) + 2k(y_1 - y_2) = Bu . \tag{2.34}$$

By defining

$$y_f = y_1 - y_2 \tag{2.35}$$

and differentiating Eq.(2.35), we obtain

$$\dot{y}_f = \dot{y}_1 - \dot{y}_2 \tag{2.36}$$

$$\ddot{y}_f = \ddot{y}_1 - \ddot{y}_2 \ . \tag{2.37}$$

The first two terms of Eq.(2.34) can be written as

$$\begin{aligned} M_1\ddot{y}_1 - M_2\ddot{y}_2 &= (M_1\ddot{y}_1 - M_2\ddot{y}_2)\frac{(M_1+M_2)}{(M_1+M_2)} \\ &= \frac{M_1^2\ddot{y}_1 + M_1M_2(\ddot{y}_1 - \ddot{y}_2) - M_2^2\ddot{y}_2}{M_t} \\ &= \frac{M_1^2\ddot{y}_1 - M_1M_2(\ddot{y}_1 - \ddot{y}_2) - M_2^2\ddot{y}_2 + 2M_1M_2(\ddot{y}_1 - \ddot{y}_2)}{M_t} \end{aligned}$$

$$M_1\ddot{y}_1 - M_2\ddot{y}_2 = \frac{(M_1 - M_2)(M_1\ddot{y}_1 + M_2\ddot{y}_2) + 2M_1M_2(\ddot{y}_1 - \ddot{y}_2)}{M_t} \tag{2.38}$$

Substituting Eqs.(2.30) and (2.37) into Eq.(2.38), we finally obtain

$$M_1\ddot{y}_1 - M_2\ddot{y}_2 = (M_1 - M_2)\ddot{y}_c + \frac{2M_1M_2}{M_t}\ddot{y}_f \ . \tag{2.39}$$

Using Eq.(2.33), Eq.(2.39) can be written as

$$M_1\ddot{y}_1 - M_2\ddot{y}_2 = (M_1 - M_2)\frac{Bu}{M_t} + \frac{2M_1M_2}{M_t}\ddot{y}_f \ . \tag{2.40}$$

Therefore, substituting Eqs.(2.35), (2.36) and (2.40) into Eq.(2.34), we obtain

$$\frac{M_1M_2}{M_t}\ddot{y}_f + c\dot{y}_f + ky_f = \frac{M_2}{M_t}Bu \ . \tag{2.41}$$

By defining the equivalent reduced mass μ as

$$\mu = \frac{M_1M_2}{M_t} \ , \tag{2.42}$$

equation (2.41) can now be written as

$$\mu\ddot{y}_f + c\dot{y}_f + ky_f = \frac{\mu}{M_1}Bu \tag{2.43}$$

which can also be transformed into the usual form

$$\ddot{y}_f + 2\zeta\omega_n\dot{y}_f + \omega_n^2 y_f = \frac{1}{M_1}Bu \tag{2.44}$$

where the natural frequency ω_n is given by

$$\omega_n = \sqrt{\frac{k}{\mu}} \tag{2.45}$$

and the damping ratio ζ is defined as

$$\zeta = \frac{c}{2\sqrt{\mu k}} \ . \tag{2.46}$$

In summary, the system equations of motion, Eqs.(2.23), can now be written as

$$\ddot{y}_c = \frac{1}{M_t} B u \tag{2.47}$$

$$\ddot{y}_f + 2\zeta\omega_n \dot{y}_f + \omega_n^2 y_f = \frac{1}{M_1} B u \tag{2.48}$$

with ω_n and ζ defined in Eqs.(2.45) and (2.46).

Equation (2.47) represents the rigid-body motion, while Eq.(2.48) represents the flexible-body motion with a resonance frequency ω_n.

From Eq.(2.45), we obtain the system stiffness as

$$k = \mu\omega_n^2 \ . \tag{2.49}$$

Substituting Eq.(2.49) into Eq.(2.46), c can be written as

$$c = 2\mu\zeta\omega_n \ . \tag{2.50}$$

Therefore, using Eqs.(2.49) and (2.50), k and c can be chosen to match a specific resonance frequency ω_n and a specific damping ratio ζ for given masses M_1 and M_2.

The transfer function mapping the input u into the base position y_1, is now derived. That is

$$Y_1(s) = G_p(s)U(s) \ . \tag{2.51}$$

Using Eqs.(2.28) and (2.35), we can write

$$y_1 = \frac{M_t y_c + M_2 y_f}{M_t} \ . \tag{2.52}$$

Taking the Laplace transform of Eqs.(2.47) and (2.48), and assuming zero initial conditions, we obtain

$$M_t s^2 Y_c(s) = BU(s) \tag{2.53}$$

and

$$M_1 Y_f(s)(s^2 + 2\zeta\omega_n s + \omega_n^2) = BU(s)\ . \tag{2.54}$$

Substituting Eqs.(2.53) and (2.54) into Eq.(2.52), we obtain

$$Y_1(s) = \left(\frac{1/M_t}{s^2} + \frac{\frac{M_2}{M_1 M_t}}{s^2 + 2\zeta\omega_n s + \omega_n^2} \right) BU(s)\ . \tag{2.55}$$

By defining

$$\beta = M_2/M_1 \tag{2.56}$$

the transfer function $G_p(s)$ relating the input u to the base position y_1 becomes

$$G_p(s) = \frac{B/M_t}{s^2} + \frac{\beta B/M_t}{s^2 + 2\zeta\omega_n s + \omega_n^2} \tag{2.57}$$

where ω_n and ζ are defined in Eqs.(2.45) and (2.46).

2.4 Methods of Analysis

As mentioned in Section 1.3, this thesis deals with space manipulators mounted on a spacecraft controlled by on-off thrusters. This section describes various methods that are used in the following chapters to analyze these nonlinear systems. The phase-plane method is initially recalled, which is a graphical procedure applicable to second-order systems only. The second method is based on the describing function, which is an approximate technique that replaces nonlinear components by linear "equivalent" ones. Finally, a numerical simulation is presented, which is a useful tool to obtain the response of a very complicated system.

2.4.1 Phase Plane Analysis

Phase plane analysis is a graphical method for studying second-order systems. This method generates, in a two-dimensional plane called the phase plane, motion trajectories corresponding to various initial conditions. It is considered in this subsection mainly because the spacecraft attitude controller used in the next chapters is based on the phase plane construction.

As mentioned in (Slotine and Li, 1991), a major class of second-order systems can be described by differential equations of the form

$$\ddot{x} + f(x, \dot{x}) = 0 \; . \tag{2.58}$$

In state-space form, the underlying dynamics can be represented as

$$\dot{x}_1 = x_2 \tag{2.59a}$$

$$\dot{x}_2 = -f(x_1, x_2) \tag{2.59b}$$

with $x_1 = x$ and $x_2 = \dot{x}$. The phase plane is defined as the plane having x and $\dot{x}$ as coordinates. There are basically three methods to obtain the phase plane trajectories for systems such as that of Eqs.(2.59). The first method is to numerically integrate the system equations and then plot the trajectories. The second method is to solve Eqs.(2.59) symbolically and obtain the phase plane trajectories. The third method is to use graphical techniques, as the method of isoclines (Graham and McRuer, 1961). The second method will be illustrated below with the use of a simple example.

Let us consider a constant force F acting on a single mass M without any friction. The dynamics of this simple system is described by

$$M\ddot{x} = F \tag{2.60}$$

which can be written as

$$\ddot{x} = F/M \; . \tag{2.61}$$

By noting that $\ddot{x} = (d\dot{x}/dx)(dx/dt) = \dot{x}(d\dot{x}/dx)$, we can write Eq.(2.61) as

$$\dot{x}\,\frac{d\dot{x}}{dx} = \frac{F}{M} \tag{2.62}$$

or

$$\dot{x}\, d\dot{x} = \frac{F}{M}\, dx \ . \tag{2.63}$$

Integration of Eq.(2.63) yields

$$\frac{1}{2}\dot{x}^2 = \frac{F}{M}x + C \tag{2.64}$$

where C is a constant. Let us assume that the initial conditions are $x(0) = x_0$ and $\dot{x}(0) = \dot{x}_0$. Using these initial conditions, C is given by

$$C = \frac{1}{2}\dot{x}_0^2 - \frac{F}{M}x_0 \tag{2.65}$$

and Eq.(2.64) can be written as

$$x = \frac{1}{2}\frac{M}{F}\dot{x}^2 + \left(x_0 - \frac{1}{2}\frac{M}{F}\dot{x}_0^2\right) \ . \tag{2.66}$$

Therefore, phase plane trajectories are parabolas defined by Eq.(2.66), which depend on the initial conditions and the acceleration F/M. The orientation of the parabolas is dependent upon the direction of the force F. For a given mass and force, the trajectories for a positive F are depicted in Fig. 2.7(a) and the trajectories for a negative F in Fig 2.7(b).

More on phase plane analysis is presented in Chapter 3, which is concerned with control aspects.

2.4.2 Describing Function Analysis

The describing function is a tool used to find the approximate response of nonlinear systems using methods derived for studying the frequency response of linear systems. The main use of this method is the prediction of limit cycles in nonlinear systems, although it has a number of other applications, such as predicting subharmonics, jump phenomena, and the response of nonlinear systems to sinusoidal inputs. However, here, only the prediction of limit cycles is discussed in detail.

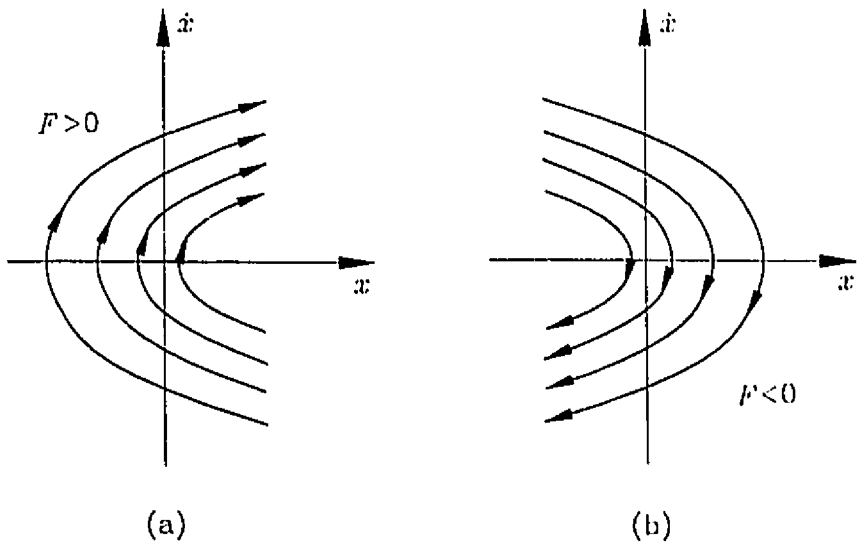

Figure 2.7: Parabolic phase plane trajectories.

First, it is important to define what kind of nonlinear systems can be analyzed with the describing function method. Simply stated, any system that can be transformed into the configuration in Fig. 2.8 can be studied using describing functions. However, to use the describing function technique in its simplest form (single input describing function), in a system that has only one nonlinear component, three basic conditions must be observed, as stated in (Slotine and Li, 1991):

1. the linear element has low-pass properties, and therefore, for a sinusoidal input $x = A\sin(\omega t)$, only the fundamental component $w_1(t)$ in the output $w(t)$ needs to be considered,

2. the nonlinear component is time-invariant, and

3. the nonlinearity is odd, which is the case for most common nonlinearities.

If a limit cycle is present in the system, the system signals must all be periodic, and hence these periodic signals can be expanded as the sum of many harmonics. Moreover, if the linear element in Fig. 2.8 has low-pass properties, which is true for most physical systems, then the higher frequency signals will be filtered out and the output $y(t)$ will be composed mostly of the lowest harmonic. Therefore, for the case

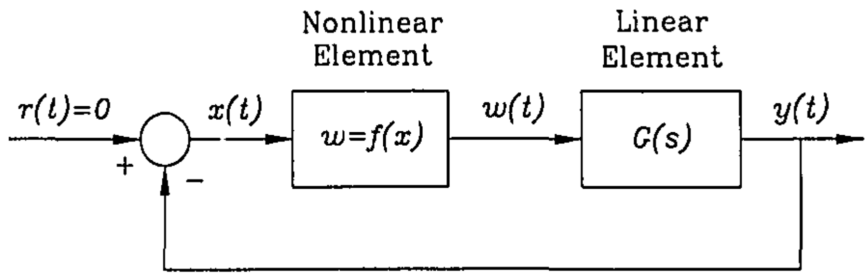

Figure 2.8: A nonlinear system.

where a limit cycle is present, it is appropriate to assume that the signals in the whole system are basically sinusoidal in form.

Using this assumption, a describing function can be found that represents the nonlinear component. Considering a sinusoidal input $x(t) = A\sin(\omega t)$, the output $w(t)$ of the nonlinearity is often a periodic function, and can be expanded in a Fourier series as

$$w(t) = \frac{a_0}{2} + \sum_{n=1}^{\infty}\Big[a_n\cos(n\omega t) + b_n\sin(n\omega t)\Big] \tag{2.67}$$

where

$$\begin{aligned} a_0 &= \frac{1}{\pi}\int_{-\pi}^{\pi} w(t)\,d(\omega t) \\ a_n &= \frac{1}{\pi}\int_{-\pi}^{\pi} w(t)\cos(n\omega t)\,d(\omega t) \\ b_n &= \frac{1}{\pi}\int_{-\pi}^{\pi} w(t)\sin(n\omega t)\,d(\omega t)\ . \end{aligned}$$

Since the nonlinearity is odd (third assumption above), one has $a_0 = 0$. Furthermore, due to the first assumption which states that the linear element has low-pass properties, only the fundamental component needs to be considered. Therefore,

$$w(t) = a_1\cos(\omega t) + b_1\sin(\omega t) \tag{2.68}$$

which can be written as

$$w(t) = Z\sin(\omega t + \phi) \tag{2.69}$$

where

$$Z(A,\omega) = \sqrt{a_1^2 + b_1^2} \tag{2.70}$$

and

$$\phi(A,\omega) = \tan^{-1}(a_1/b_1) \; . \tag{2.71}$$

If the describing function $N(A,\omega)$ of a nonlinearity is defined as a function that maps the input $x(t)$ to the output $w(t)$, we have

$$N(A,\omega) = \frac{w(t)}{x(t)} = \frac{Z\sin(\omega t + \phi)}{A\sin(\omega t)} \tag{2.72}$$

which can be written in complex form as

$$N(A,\omega) = \frac{Ze^{j(\omega t+\phi)}}{Ae^{j(\omega t)}} = \frac{Z}{A}e^{j\phi} = \frac{1}{A}(b_1 + ja_1) \; . \tag{2.73}$$

Thus, the describing function of the nonlinearity is given by

$$N(A,\omega) = \frac{1}{A}(b_1 + ja_1) \tag{2.74}$$

with

$$\begin{aligned} a_1 &= \frac{1}{\pi}\int_{-\pi}^{\pi} w(t)\cos(\omega t)\, d(\omega t) \\ b_1 &= \frac{1}{\pi}\int_{-\pi}^{\pi} w(t)\sin(\omega t)\, d(\omega t) \; . \end{aligned}$$

The nonlinearity representation, $N(A,\omega)$, is tabulated in many books for all typical nonlinearities. A good reference on the subject is (Gelb and Vander Velde, 1968). Therefore, the describing functions that are required in this thesis are taken from such a table, without making use of Eq.(2.74).

Now that we have a describing function for the nonlinearity, we are ready to analyze the system of Fig. 2.9 for the existence of limit cycles. $G(j\omega)$ is the frequency response of the linear element of the system and is simply obtained by substituting s by $j\omega$ in the transfer function $G(s)$. First, let us assume that there exists a self-sustained oscillation of amplitude A and frequency ω in the system. Then, the variables in the loop must satisfy the following relations

$$x = -y \tag{2.75}$$

$$w = N(A,\omega)x \tag{2.76}$$

$$y = G(j\omega)w \; . \tag{2.77}$$

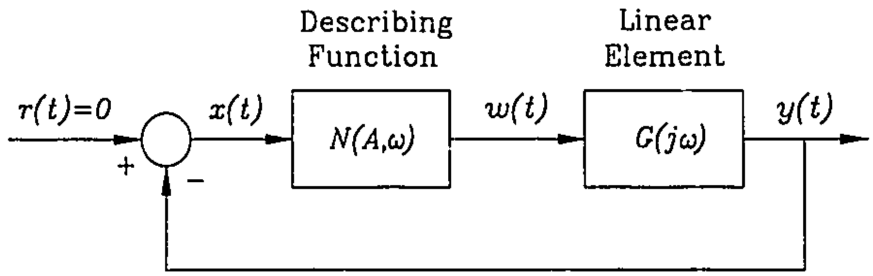

Figure 2.9: A nonlinear system.

Thus, we have $y = G(j\omega)N(A,\omega)(-y)$. Because $y \neq 0$, this implies:

$$G(j\omega)N(A,\omega) + 1 = 0 \tag{2.78}$$

which can be written as

$$G(j\omega) = -\frac{1}{N(A,\omega)} \, . \tag{2.79}$$

The amplitude A and the frequency ω of the limit cycle in the system must satisfy Eq.(2.79). If the above equation has no solution, then the nonlinear system has no limit cycle.

Since it can be difficult to solve Eq.(2.79) algebraically, a simple solution method consists of plotting both sides of Eq.(2.79) in the complex plane by varying A and ω, to observe whether the two curves intersect or not. The intersection point gives us the value of A and ω and, therefore, the approximate limit cycle $x = A\sin(\omega t)$ is completely determined.

As an example, let us consider the case when the describing function N is a function of the gain A only. So, Eq.(2.79) becomes

$$G(j\omega) = -\frac{1}{N(A)} \, . \tag{2.80}$$

The frequency response function $G(j\omega)$ can be plotted by varying ω in the complex plane as in Fig. 2.10. The same can be done for the negative inverse describing function $(-1/N(A))$ by varying A. If the two curves intersect, then there exist limit cycles and the values of A and ω corresponding to the intersection points are the

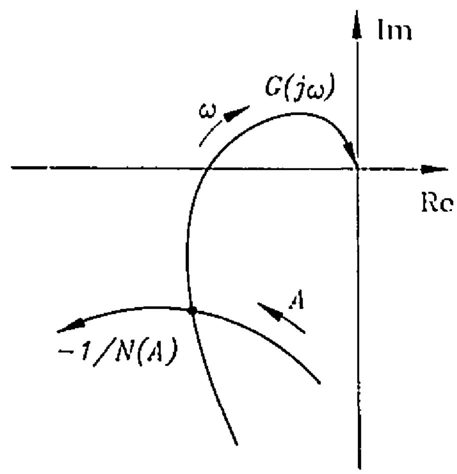

Figure 2.10: Limit cycle detection.

solutions of Eq.(2.80). If the curves intersect n times, then the system has n possible limit cycles and the one actually reached depends upon the initial conditions.

Since the describing function method is an approximate method, it is not surprising that the analysis results are sometimes not very accurate. Without going into details, we can state a general rule mentioned in (Slotine and Li, 1991). If the $G(j\omega)$ locus is tangent or almost tangent to the $-1/N(A,\omega)$ locus, as in Fig. 2.11(a), then the conclusions from a describing function analysis might be erroneous. Conversely, if the $-1/N(A,\omega)$ locus intersect the $G(j\omega)$ locus almost at right angles, as in Fig. 2.11(b), then the results of the describing function analysis are usually accurate.

An intersection point of the two loci within the complex plane does not guarantee stability of the predicted limit cycle. Such limit cycle can be unstable and it will never be observed. For brevity, we can state here a simple Limit Cycle Criterion based on the extended Nyquist criterion as stated in (Slotine and Li, 1991), namely,

Limit Cycle Criterion: *Each intersection point of the curve $G(j\omega)$ and the curve $-1/N(A)$ corresponds to a limit cycle. If points near the intersection and along the increasing-A side of the curve $-1/N(A)$ are not encircled by the curve $G(j\omega)$, then the corresponding limit cycle is stable. Otherwise, the limit cycle is unstable.*

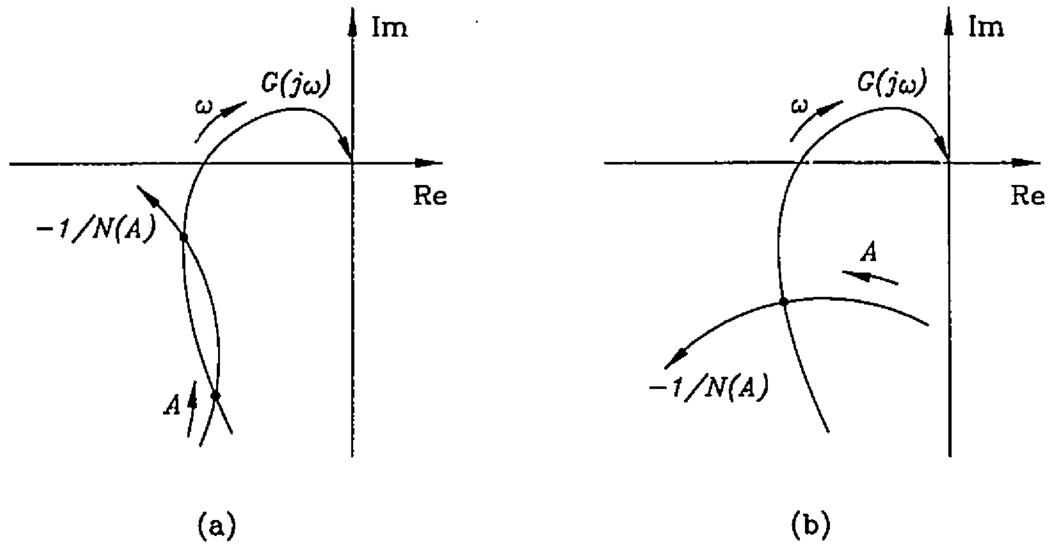

Figure 2.11: Reliability of limit cycle prediction.

For example, Fig. 2.11(b) depicts a stable limit cycle.

On the other hand, if no intersection of the loci $G(j\omega)$ and $-1/N(A)$ exists, the stability of the system is assessed using the normal Nyquist criterion with respect to any point on the $-1/N(A)$ locus rather than the point (−1,0) (Atherton, 1975). For example, assuming that $G(j\omega)$ is stable, Fig. 2.12(a) depicts a stable system while Fig. 2.12(b) an unstable one.

2.4.3 Simulation

The third method used to analyze a nonlinear system is by simulation, a very convenient way of obtaining results, since one just has to set up an adequate model and simulate its behaviour numerically. However, to perform many simulation runs, such as those required in a parametric study, can be very time consuming and give little insight on the physical system, as compared to algebraic or analytical methods. Therefore, in this thesis, simulations are used only to verify important results obtained with the describing function and phase plane analysis. The simulations model will be implemented with *Simulink*, a *Matlab* package that accommodates model definition and dynamic simulation.

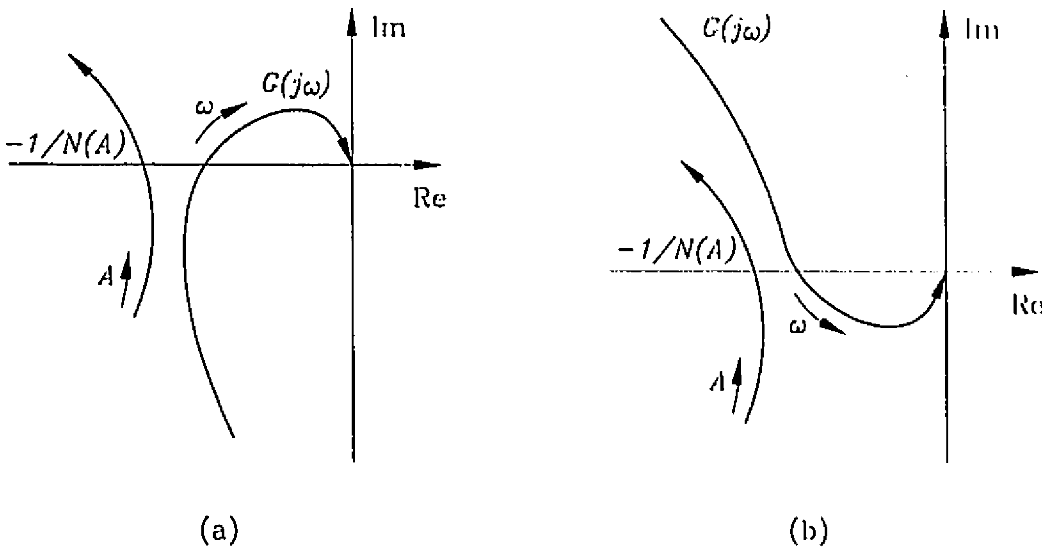

Figure 2.12: Stability prediction. (a) Stable system, (b) Unstable system.

Chapter 3

Control Problem

3.1 Introduction

In Chapter 2, a two-flexible-joint planar manipulator mounted on a spacecraft has been modelled, and a two-DOF simplified model was derived. As seen in Subsection 1.2.1, control methods have been developed to control the end-effector of such robots, while leaving the base free to react to disturbances. However, in cases where this is undesired, on-off thrusters must be used to control the attitude and the position of the spacecraft. Since, in this thesis, the latter control scheme is considered, a method for controlling the base must be formulated in order to analyze the problem of dynamic interactions at hand. The spacecraft control problem with on-off thrusters is addressed in this chapter to develop the detailed models required for analysis. Finally, stability definitions used in this thesis are presented.

3.2 Spacecraft Control Scheme

As mentioned in Section 1.3, in this thesis it is assumed that the spacecraft attitude and position are controlled by jet thrusters. The technology currently available does not allow the use of proportional valves in space, and thus, the classical linear control schemes of PD and PID control cannot be used. Therefore, actual spacecrafts are controlled by the use of on-off thrusters, that are nonlinear devices, since they are either on or off. The classical way of dealing with such devices is to use a controller based on phase plane methods. This controller requires the attitude and rate of the spacecraft as inputs. Since these two signals are not always available, a state estimator is needed to find an estimate for the required states. Thus, the general control scheme for the spacecraft is presented by the block diagram of Fig. 3.1. In the following sections, the controller, plant and state estimator blocks are considered separately to establish the models needed to analyze the problem at hand.

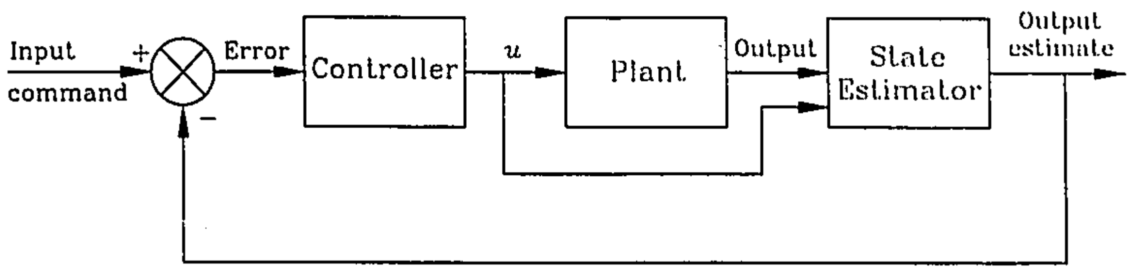

Figure 3.1: Standard spacecraft control scheme.

3.3 Controller

3.3.1 Simple Standard Controller Form

The usual scheme to control spacecraft with on-off thrusters is by the use of the error phase plane. This plane is defined as the plane having the spacecraft attitude error e and error rate $\dot{e}$ as coordinates. The on-and-off switching is determined by switching lines in the phase plane and can become very complex, as shown in (Sackett and Kirchwey, 1982) for the phase plane controller of the Space Shuttle. A simple switching logic used in this thesis is presented in Fig. 3.2. The phase plane is divided into three regions separated by two switching lines. The region between these two lines is a dead zone, whereby the thrusters are off. The right area is a zone where the thrusters are on in a given direction, while the left area is a zone where they are on in the opposite direction.

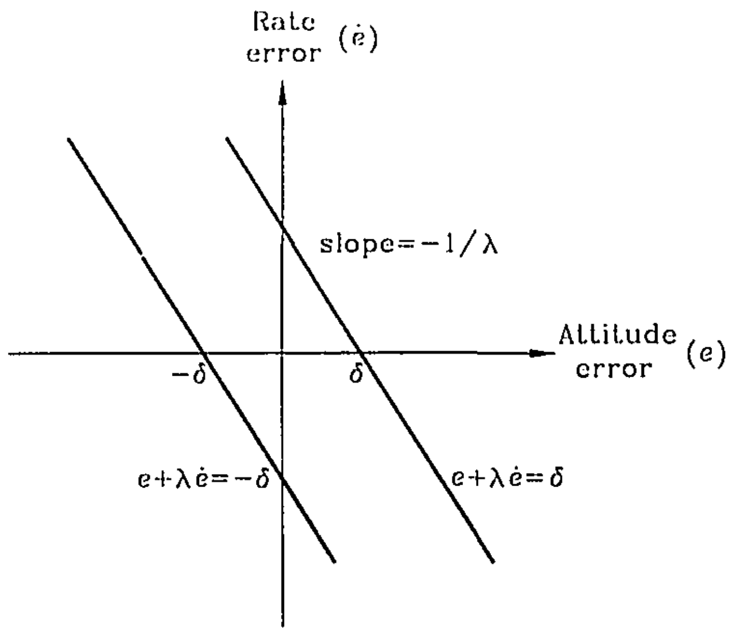

Figure 3.2: Switching logic in the error phase plane.

The dead zone limits $[-\delta, \delta]$ are determined by the attitude limit requirements, the slope of the switching lines being given by the desired rate of convergence towards the equilibrium and by the rate limits. The equations of the switching lines are

$$e + \lambda\dot{e} = \delta \tag{3.1a}$$

$$e + \lambda\dot{e} = -\delta \tag{3.1b}$$

where λ is the negative inverse of the slope of these lines. Note that the smaller λ, the higher the slope of the switching line and, therefore, the larger can be the rate errors.

This control logic is presented in block-diagram form in Fig. 3.3. It is composed of a relay nonlinearity with a dead zone. The input to this relay is the left-hand side of the switching lines, Eqs.(3.1), and the output is the command of the thrusters u, either $+1$, 0 or -1, based on the amplitude of the incoming signal.

This control scheme is understood more easily with the analysis of a single mass system controlled by thrusters. This is the subject of the next subsection.

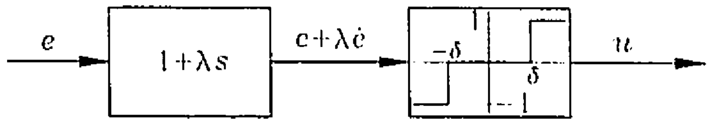

Figure 3.3: Controller block.

3.3.2 Phase Plane for a Single Rigid Body

As an example, the single-mass system studied in subsection 2.4.1 is considered. In this case, the force F acting on the mass is the force B developed by the thrusters. Therefore, we can rewrite Eq.(2.66), which gives the phase plane trajectories, by replacing the force F by the thrusters force B

$$x = \frac{1}{2}\frac{M}{B}\dot{x}^2 + \left(x_0 - \frac{1}{2}\frac{M}{B}\dot{x}_0^2\right) . \tag{3.2}$$

If the desired position of the mass is $x_d = 0$, the position error and the velocity error can be defined as:

$$e = -x \tag{3.3a}$$

$$\dot{e} = -\dot{x} . \tag{3.3b}$$

Using Eqs.(3.3), along with $e_0 = -x_0$ and $\dot{e}_0 = -\dot{x}_0$, Eq.(3.2) can be written as

$$e = \left(e_0 + \frac{1}{2}\frac{M}{B}\dot{e}_0^2\right) - \frac{1}{2}\frac{M}{B}\dot{e}^2 . \tag{3.4}$$

This equation represents the equation of a parabola in the error phase plane for a particular set of initial conditions (e_0, $\dot{e}_0$), the orientation of the parabola being determined by the direction of the thrusters firing. Therefore, the trajectories of the mass in the error phase plane are a combination of parabolic paths when the thrusters are on and horizontal linear paths when the thrusters are off (constant-velocity coasting). Given a particular set of initial conditions in the error phase plane, Fig. 3.4 presents schematically the thruster control of the single-mass system. The convergence rate is determined by the inclination of the switching lines, a limit cycle being unavoidable since a zero-gravity environment is considered with no disturbance

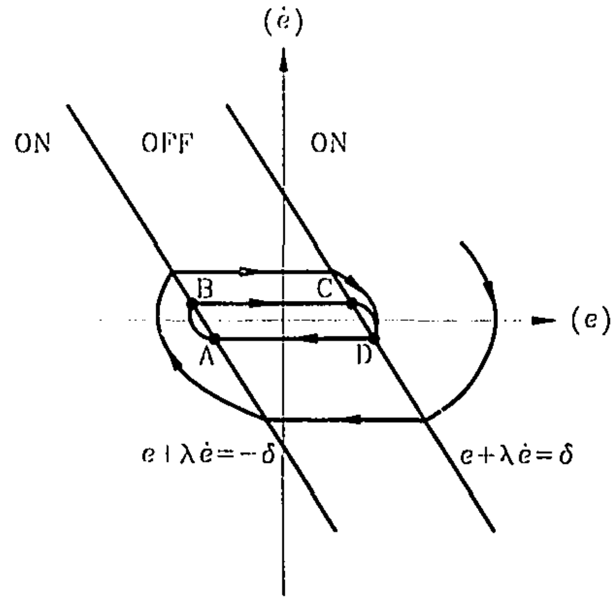

Figure 3.4: Single-mass example.

forces. The smaller the vertical dimension of this limit cycle, the smaller the fuel consumption, since the thrusters are firing for a very short period (during motions A-B and C-D).

More details must be given about the final limit cycle, since we said that it was unavoidable. This statement is true for practical reasons: when a thruster is turned on, it will remain on for at least a minimum operating time $\Delta T_{\min}$. However, if we consider a perfect theoretical relay with no minimum on-time, then we can imagine an impulse that will stop the mass. Because of physical limitations, this is impossible in any practical system, which is why we stated that the final limit cycle is unavoidable.

In practical systems, hysteresis and time delays are present. The effects of these two parameters are described in the next subsection with the use of the same single-mass example.

3.3.3 Effects of Hysteresis and Time Delays

In practical relay systems, hysteresis must be included to avoid a phenomenon called chatter, which is well described in (Flügge-Lotz, 1968). When a thruster is chattering, it turns on-and-off continuously, for a very short period ΔT_{min}. This behaviour can reduce considerably the useful life span of thrusters, while the addition of hysteresis can reduce the severity of this problem. Also, when relays are modelled, a time delay must be included since there is actually a delay between the time at which an open (or close) command is sent to the valves and the time at which the valves open (or close).

In this subsection, the effects of adding hysteresis and a pure time delay in the system are discussed. First, if hysteresis is included in the controller, the relay nonlinearity of Fig. 3.3 changes to that depicted in Fig. 3.5(a). The corresponding effect on the switching logic in the error phase plane is to add two switching lines, as shown in Fig. 3.5(b). This means that the turn-on switching lines (1 and 3) are not the same as the turn-off ones (2 and 4). Referring to Fig. 3.5(b), the equations of the switching lines are:

$$\begin{aligned}
&1. \quad & e+\lambda\dot{e} &= \delta \\
&2. \quad & e+\lambda\dot{e} &= \delta-\Delta \\
&3. \quad & e+\lambda\dot{e} &= -\delta \\
&4. \quad & e+\lambda\dot{e} &= -\delta+\Delta\,.
\end{aligned}$$

Since the turn-off switching lines are closer to the origin than the turn-on ones, the thrusters stay on for a longer period because they stop only when the turn-off switching line is reached instead of the original line, as when there is no hysteresis. Therefore, the more hysteresis Δ we add to the system, the larger the final limit cycle. A final limit cycle for the single-mass system example is presented schematically in Fig. 3.6.

Now a pure time delay τ_d is added to the hysteretic controller, such that when the controller sends the command to turn on or off the thrusters, the command is

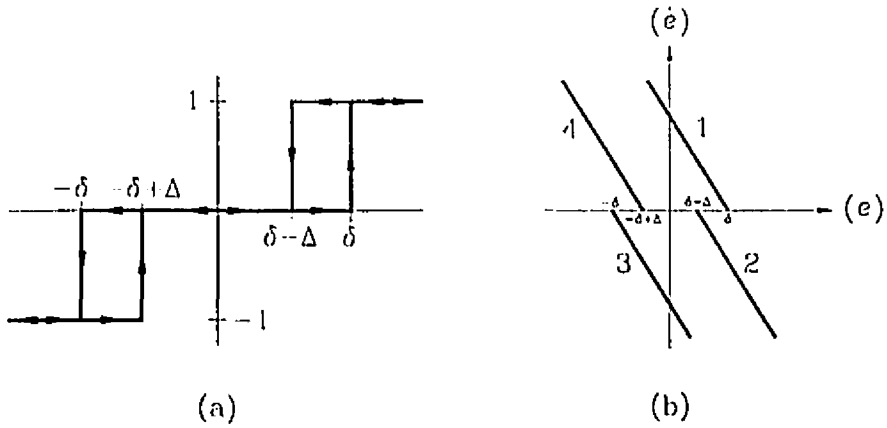

Figure 3.5: Controller with hysteresis. (a) Relay nonlinearity, (b) Phase plane switching logic.

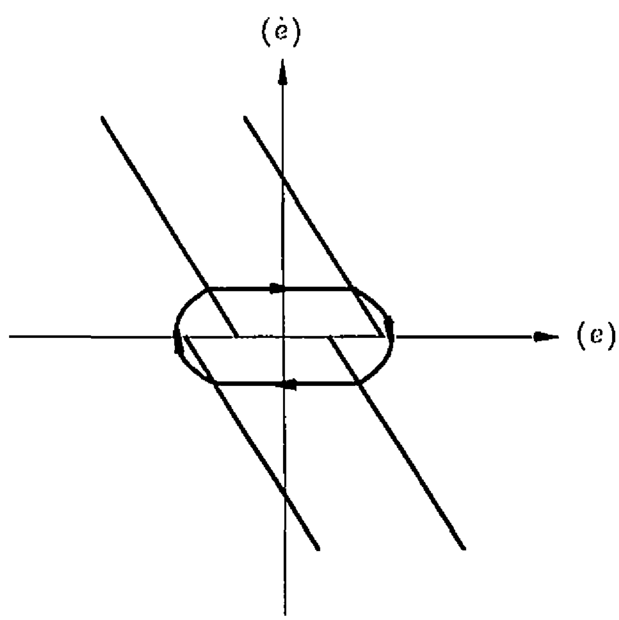

Figure 3.6: Single-mass example with an hysteretic controller.

executed τ_d seconds later. The effect of the time delay in the error phase plane is to change the slope of the switching lines, as shown in Fig. 3.7.

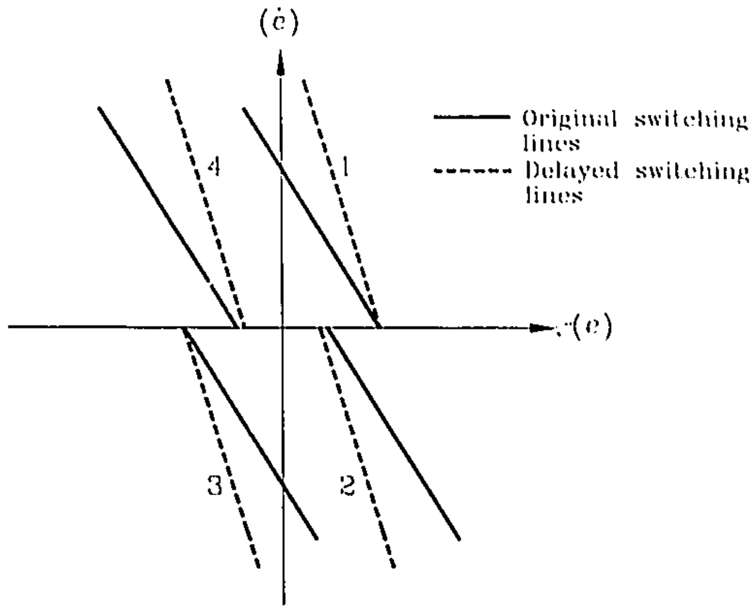

Figure 3.7: Effects of a pure time delay on the switching logic.

For the single-mass system, the new switching line equations are (Graham and McRuer, 1961)

$$\begin{array}{llcl}
1. & e + (\lambda - \tau_d)\dot{e} & = & \delta \\
2. & e + (\lambda - \tau_d)\dot{e} & = & -\dfrac{1}{2}\dfrac{B}{M}\tau_d(2\lambda - \tau_d) + \delta - \Delta \\
3. & e + (\lambda - \tau_d)\dot{e} & = & -\delta \\
4. & e + (\lambda - \tau_d)\dot{e} & = & \dfrac{1}{2}\dfrac{B}{M}\tau_d(2\lambda - \tau_d) - \delta + \Delta \, .
\end{array}$$

3.3.4 Describing Function of the Relay Nonlinearity

In this subsection, the describing functions for the two nonlinearities used in this thesis are derived. These describing functions are taken from (Gelb and Vander Velde, 1968) and adapted for the notation used in this thesis. For the relay containing a dead zone, as shown in Fig. 3.3, the describing function is given by

$$N_d(A) = \frac{4}{\pi A^2}\sqrt{A^2 - \delta^2}, \qquad A > \delta \tag{3.5}$$

where A is the amplitude of the predicted limit cycle and δ the deadband limit.

As well, the relay containing a dead zone and hysteresis of Fig. 3.5(a), is represented by

$$N_h(A) = \frac{2}{\pi A^2}\left[\sqrt{A^2-\delta^2} + \sqrt{A^2-(\delta-\Delta)^2}\right] - \frac{2\Delta}{\pi A^2}j, \qquad A > \delta \qquad (3.6)$$

where the first term represents the real part and the second term, the imaginary part of the describing function. Again, A is the amplitude of the predicted limit cycle, δ the deadband limit and Δ the amount of hysteresis included in the relay. It is noted that, for a relay nonlinearity, since the parameters δ and Δ are fixed by design, the describing function is simply a function of the amplitude A of the limit cycle and no longer a function of the frequency ω. Figure 3.8 introduces the $-1/N_d(A)$ and $-1/N_h(A)$ loci, which are plotted in the complex plane.

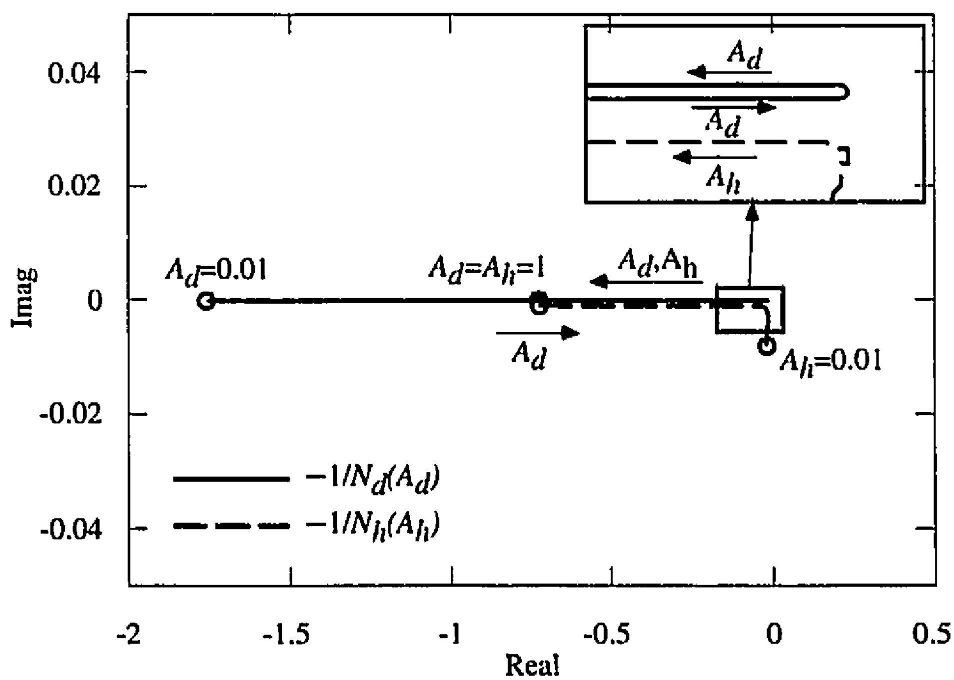

Figure 3.8: Loci of the describing functions for the relays.

3.4 Plant

For the plant block, see Fig. 3.1, the equations representing the dynamics of the simplified system are used. These equations are written in state-space and in transfer-function form in Subsection 2.3.2; they are then used in the appropriate model in the sections below. The sensors can be considered as part of the plant. A time delay τ must be included to account for the delay between the time a sensor reads a measurement and the time this measurement is used. Since this time delay is more significant than that of the relay operation due to the delay between the time the controller sends the command to turn on or off the thrusters, and the time this command is executed, only the sensor time delay is included in the models (and that of the relay is neglected). In block diagram form, the plant block is given in Fig. 3.9(a) for the state-space form, and in Fig. 3.9(b) for the transfer-function form. A thick line represents a state vector, while a thin line represents a scalar variable.

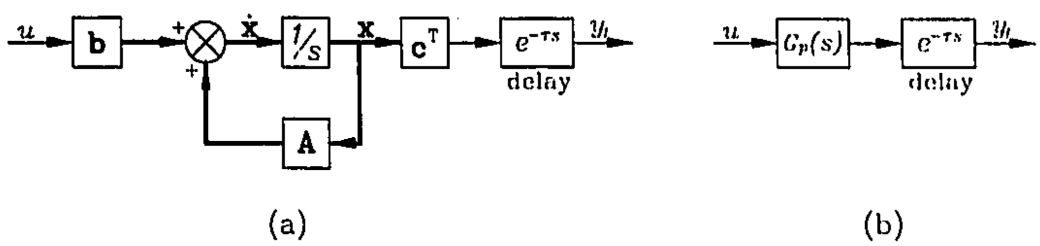

Figure 3.9: Plant block in: (a) state-space form and (b) transfer-function form.

3.5 State Estimator

A very important aspect in control system design is the design of state estimators, also known as state observers. Observers provide estimates for the states that are not readily available from measurements but are still required for feedback control, by using the states available by sensors.

In the case at hand, the required states are the position and the velocity of the system base. Using current space technology, both states can be obtained by sensor readings. However, it can happen that only the attitude is available and the velocity must be estimated with the use of a state estimator.

In this thesis, three cases are considered. For case 1, we assume that both signals are available and we simply pass these signals through filters to eliminate high-frequency noise. For the last two cases, we assume that only the position is available from sensors and use two different state estimators. In case 2, we differentiate the position signal while passing it through a filter to obtain an estimate for the velocity. The position signal is also filtered in this case. For case 3, a classical asymptotic state observer is used to obtain an estimate for the position and the velocity. This observer also has a filtering effect. In the following sections, each of these three cases is presented in more detail.

3.5.1 Case 1: Position and Velocity Filters

When position and velocity are available from sensors, the function of the state estimator is simply to filter high frequency noise. This can be shown schematically by the block diagram of Fig. 3.10.

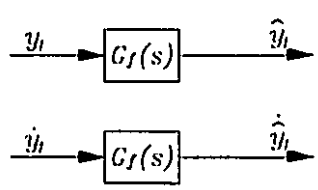

Figure 3.10: Case 1: block diagram when just filters are used.

Because of their simplicity, second-order filters are used, which can be represented with the following transfer function $G_f(s)$

$$G_f(s) = \frac{\omega_f^2}{s^2 + 2\zeta_f\omega_f s + \omega_f^2} \; . \tag{3.7}$$

The cutoff frequency ω_f must be chosen to filter high frequencies such that it does not slow down the response of the system by reducing its bandwidth. Since, for any particular system, the exact frequency content of the noisy signals is not known, we will use ω_f as a parameter in our study to examine its influence on the system performance. The damping term ζ_f in Eq.(3.7) is chosen to be 0.707, which gives good performance, since it is relatively fast, with small overshoot (4%) (Ogata, 1990).

3.5.2 Case 2: Velocity Estimator with Position Filter

The state estimator presented in Fig. 3.11 is similar to the one used on the Space Shuttle for on-orbit operations (Penchuk, Hattis and Kubiak, 1985; Sackett and Kirchwey, 1982; Hattis, 1982). It uses the current acceleration of the system centre of mass ($\ddot{y}_c = B/M_t$) and the delayed position (attitude) signal as input. Integrating the acceleration $\ddot{y}_c$ imposed to the whole system by the thruster action, an estimate for the velocity $\dot{\hat{y}}_c$ and the position $\hat{y}_c$ of the system centre of mass can be obtained. From Eq.(2.52), we have

$$y_f = \frac{M_t}{M_2}(y_1 - y_c) \ . \tag{3.8}$$

By defining

$$y'_f = \frac{M_2}{M_t}y_f = (y_1 - y_c) \ , \tag{3.9}$$

an estimate of y'_f, $\hat{y}'_f$, can be obtained by subtracting $\hat{y}_c$ from y_1. Differentiating this "flexible-position" estimate and passing it through a filter to eliminate high-frequency noise, a "flexible-rate" estimate $\dot{\hat{y}}'_f$ can be obtained. Then, adding the velocity estimate of the centre of mass of the system, $\dot{\hat{y}}_c$, we finally obtain an estimate for the velocity of the base $\dot{\hat{y}}_1$, since

$$\dot{\hat{y}}'_f + \dot{\hat{y}}_c = \frac{d}{dt}(y_1 - \hat{y}_c) + \dot{\hat{y}}_c = \dot{\hat{y}}_1 \ . \tag{3.10}$$

The differentiation of a noisy signal is usually not recommended because this amplifies the noise level in the signal. However, in this case, only the flexible part needs to be differentiated. This means that, for a rigid system, no differentiation is necessary. Therefore, this kind of state estimator can give very good results for cases of low

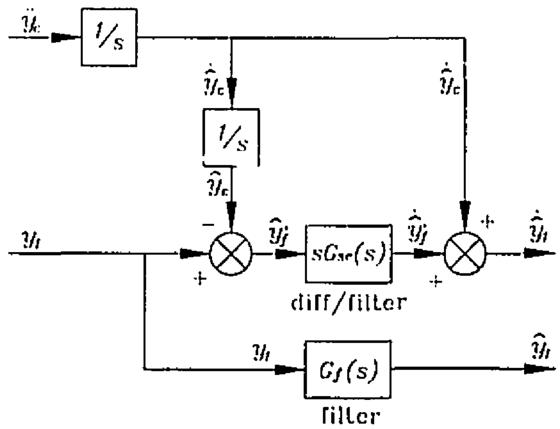

Figure 3.11: Case 2: block diagram for the velocity estimator only.

flexibility. The position filter is the same as the one presented in Subsection 3.5.1, the differentiator-filter being given by $sG_{sc}(s)$ where

$$G_{sc}(s) = \frac{\omega_{sc}^2}{s^2 + 2\zeta_{sc}\omega_{sc}s + \omega_{sc}^2} \ . \tag{3.11}$$

Again, ω_f of Eq.(3.7) will be a parameter in our study and ζ_f is chosen to be 0.707. The cutoff frequency for the differentiator-filter is chosen as $\omega_{sc} = 0.2513$ rad/s and the damping ratio as $\zeta_{sc} = 0.707$. These two values correspond to the approximated ones used on the Space Shuttle, as explained in (Penchuk, Hattis and Kubiak, 1985; Sackett and Kirchwey, 1982).

3.5.3 Case 3: Asymptotic State Estimator

The last state estimator studied is a classical asymptotic state estimator described in many books, for example (Chen, 1984).

Consider a plant model

$$\dot{\mathbf{x}} = \mathbf{A}\mathbf{x} + \mathbf{b}u \tag{3.12}$$

and a single continuous measurement of the output of the plant y_1

$$y_1 = \mathbf{c}^T\mathbf{x} \tag{3.13}$$

where $\mathbf{A}$, $\mathbf{b}$ and $\mathbf{c}$ are given by Eqs.(2.26) and (2.27). We can obtain an estimate for the state vector $\mathbf{x}$ with the use of y_1, u and knowledge of $\mathbf{A}$ and $\mathbf{b}$.

By defining

$$\hat{\mathbf{x}} = \text{estimate of } \mathbf{x} \ , \tag{3.14}$$

an estimated value of the measurement y_1 is given by

$$\hat{y}_1 = \mathbf{c}^T \hat{\mathbf{x}} \ . \tag{3.15}$$

With knowledge of $\mathbf{A}$, $\mathbf{b}$ and u, an estimate of $\mathbf{x}$ is available by feeding u into a software-implemented computer model of the plant, namely,

$$\dot{\hat{\mathbf{x}}} = \mathbf{A}\hat{\mathbf{x}} + \mathbf{b}u \ . \tag{3.16}$$

Under perfect knowledge of $\mathbf{A}$ and $\mathbf{b}$, Eqs.(3.15) and (3.16) would give the actual position of the base. However, this is never the case; the way to solve this problem is to feedback the error $y_1 - \hat{y}_1$ into every equation of Eq.(3.16), i.e.,

$$\dot{\hat{\mathbf{x}}} = \mathbf{A}\hat{\mathbf{x}} + \mathbf{b}u + \mathbf{k}(y_1 - \mathbf{c}^T\hat{\mathbf{x}}) \tag{3.17}$$

where

$$\mathbf{k} = \begin{bmatrix} L_1 \\ L_2 \\ L_3 \\ L_4 \end{bmatrix} \ . \tag{3.18}$$

By defining

$$\tilde{\mathbf{x}} = \hat{\mathbf{x}} - \mathbf{x} \tag{3.19}$$

as the error in the estimate, $\tilde{\mathbf{x}}$ can be determined by subtracting Eq.(3.12) from Eq.(3.17):

$$\dot{\tilde{\mathbf{x}}} = \mathbf{A}\tilde{\mathbf{x}} + \mathbf{k}(y_1 - \mathbf{c}^T\hat{\mathbf{x}}) \ . \tag{3.20}$$

Using Eq.(3.13), Eq.(3.20) can be written as

$$\dot{\tilde{\mathbf{x}}} = (\mathbf{A} - \mathbf{k}\mathbf{c}^T)\tilde{\mathbf{x}} \ . \tag{3.21}$$

Therefore, the gains L_1, L_2, L_3 and L_4 can be chosen such that the error equations Eq.(3.21) are stable, providing that $\{\mathbf{c}^T, \mathbf{A}\}$ is an observable pair, which is the case here. Then, the error $\tilde{\mathbf{x}}$ will tend toward zero as t increase. Now that a reasonable estimate $\hat{\mathbf{x}}$ is available, the desired estimate for the position and velocity of the base can be obtained with

$$\hat{\mathbf{y}} = \mathbf{E}\hat{\mathbf{x}} \tag{3.22}$$

where

$$\hat{\mathbf{y}} = [\hat{y}_1, \dot{\hat{y}}_1]^T ,$$

$$\mathbf{E} = \begin{bmatrix} 1 & 0 & 0 & 0 \\ 0 & 1 & 0 & 0 \end{bmatrix}$$

and $\hat{\mathbf{x}}$ as defined in Eq.(2.24).

The block diagram describing the asymptotic state estimator is illustrated in Fig. 3.12. The determination of gain $L_1, \cdots, L_4$ is an important part of this state estimator design. If the frequencies corresponding to the poles in the system of Eq.(3.21) are too large, then we obtain a very good estimate, but the filtering is not sufficient. Conversely, if these frequencies are too small, the filtering effect is very good but we obtain a poor estimate. Therefore, these gains must be determined carefully to obtain a reasonable performance of the state estimator.

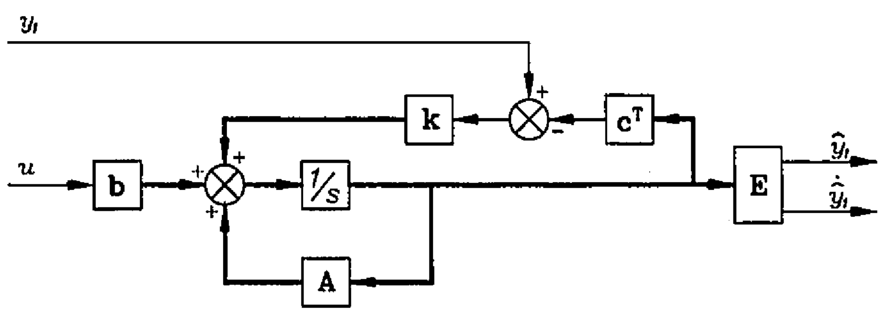

Figure 3.12: Case 3: block diagram for the asymptotic state estimator.

3.6 Modelling

This section introduces the complete models that are used to perform the describing function analysis and to run simulations. There is one model for each state estimator, as introduced in the previous section.

3.6.1 Case 1: Model with Position and Velocity Filters

In the model of Fig. 3.13, it is assumed that both position and velocity of the base are available for feedback. These signals are passed through a second-order filter $G_f(s)$ to eliminate high-frequency noise. The transfer function, $G_{\text{filter}}(s)$, representing the linear elements (Fig. 2.9) of this model is derived in Appendix B.1 and is given as

$$G_{\text{filter}}(s) = (1 + \lambda s) \exp^{-\tau s} G_p(s) G_f(s) \ , \tag{3.23}$$

where $G_p(s)$ and $G_f(s)$ are defined in Eqs.(2.57) and (3.7). Moreover, $G_p(s)$ represents the plant transfer function, while $G_f(s)$ is the transfer function of a second-order filter.

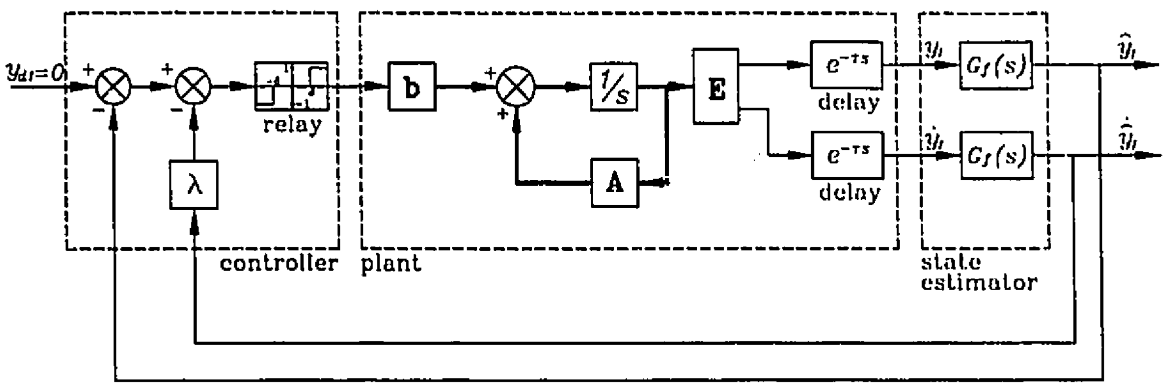

Figure 3.13: Case 1: model with position and velocity filters.

3.6.2 Case 2: Model with a Velocity Estimator and a Position Filter

For the model shown in Fig. 3.14, only the position is available for feedback. Since the velocity is also required, it is estimated with a differentiator combined with a filter $G_{se}(s)$. The position signal, in turn, is passed through a filter $G_f(s)$. For this model, the transfer function of the linear elements $G_{\text{rate}}(s)$ (Fig. 2.9) is derived in

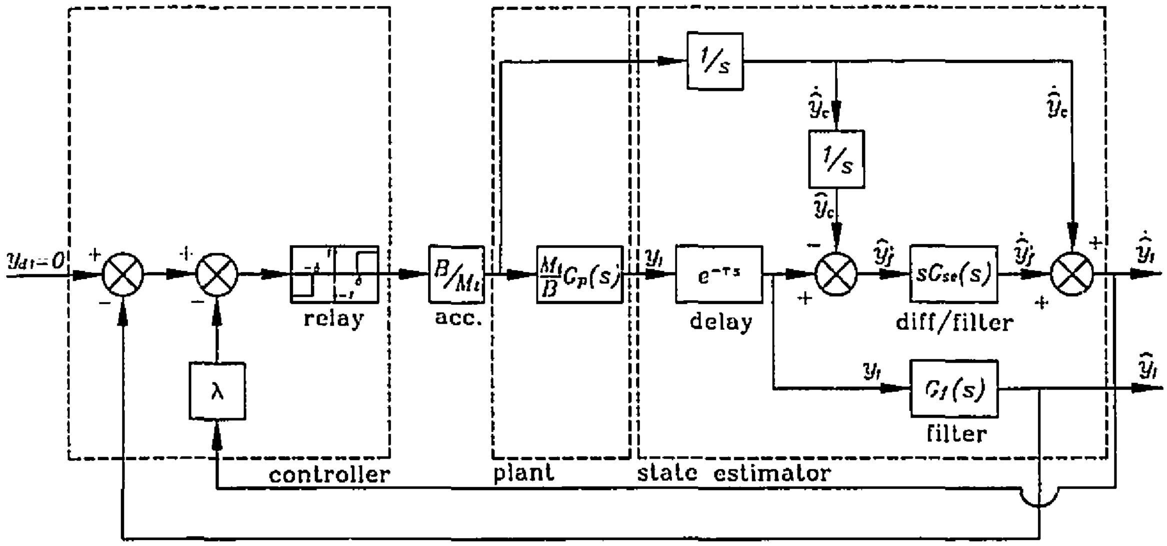

Figure 3.14: Case 2: model with a velocity estimator and a position filter.

Appendix B.2 and is given by

$$G_{rate}(s) = \exp^{-Ts} G_p(s)\Big(G_f(s) + \lambda s G_{se}(s)\Big) + \frac{\lambda B}{M_t s}\Big(1 - G_{se}(s)\Big) \,, \tag{3.24}$$

where $G_p(s)$, $G_f(s)$ and $G_{se}(s)$ are defined in Eqs.(2.57), (3.7) and (3.11) respectively. Finally, $G_p(s)$ represents the plant transfer function, while $G_f(s)$ and $G_{se}(s)$ are the transfer function of second-order filters.

3.6.3 Case 3: Model with an Asymptotic State Estimator

The last model discussed is the one using an asymptotic state estimator, as shown in Fig. 3.15. The position signal is used to obtain an estimate of the position and the velocity of the base. As derived in Appendix B.3, the transfer function $G_{asym}(s)$ of the linear elements (Fig. 2.9) of this model is given by

$$G_{asym}(s) = \begin{bmatrix} 1 & \lambda \end{bmatrix} \begin{bmatrix} g_{11}(s) & g_{12}(s) \\ g_{21}(s) & g_{22}(s) \end{bmatrix} \begin{bmatrix} 1 \\ \exp^{-Ts} G_p(s) \end{bmatrix} \tag{3.25}$$

where,

$$g_{11}(s) = \frac{M_2 s^2 + cs + k}{D(s)} \,,$$

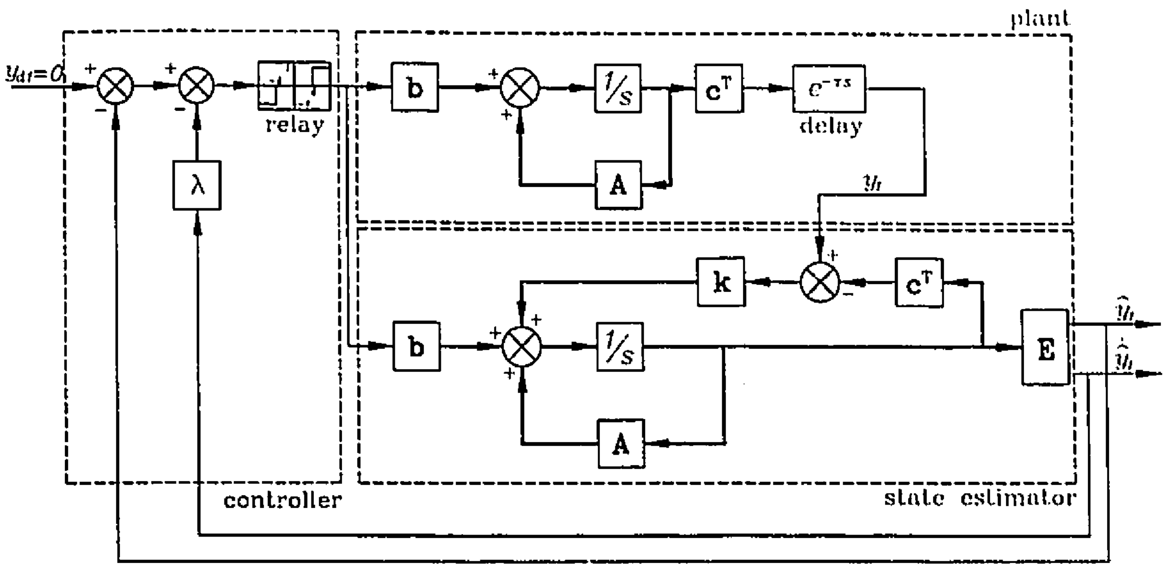

Figure 3.15: Case 3: model with an asymptotic state estimator.

$$g_{12}(s) = \frac{M_1M_2\Big[L_1s^3 + \Big(\frac{cL_1}{\mu} + L_2\Big)s^2\Big] + \Big(kM_1L_1 + cM_1L_2 + kM_2L_3 + cM_2L_4\Big)s + kM_1L_2 + kM_2L_4}{D(s)},$$

$$g_{21}(s) = \frac{M_2s^3 + \Big(c + L_1M_2\Big)s^2 + \Big(k + cL_1\Big)s + kL_1}{D(s)},$$

$$g_{22}(s) = \frac{M_1M_2L_2s^3 + \Big(cM_1L_2 - kM_2L_1 + kM_2L_3 + cM_2L_4\Big)s^2 + \Big(kM_1L_2 + kM_2L_4\Big)s}{D(s)},$$

with

$$D(s) = M_1M_2\Big[s^4 + \Big(\frac{c}{\mu} + L_1\Big)s^3 + \Big(\frac{k}{\mu} + \frac{cL_1}{\mu} + L_2\Big)s^2\Big] + \Big(kM_1L_1 + kM_2L_3 + cM_1L_2 + cM_2L_4\Big)s + kM_1L_2 + kM_2L_4$$

and $G_p(s)$ and μ are defined in Eqs.(2.57) and (2.42). $G_p(s)$ represents the plant transfer function, while μ is the equivalent reduced mass.

3.7 Stability

3.7.1 Definitions

In this subsection, a stability definition is given and used to describe the possible behaviours of the system, as modelled in Section 3.6. This stability definition is based on the rate of fuel consumption of the system, which is explained in more detail below.

The fuel consumed by the thrusters is proportional to their opening time. Therefore, we can write

$$Z(t) = S \int |u|\, dt \tag{3.26}$$

where S is a specific constant dependent upon the type of thruster fuel used and the characteristics of the thrusters, and u is the thrusters command, either $+1$, 0 or -1. Since S is constant, the fuel consumption $F_c(t)$ is defined in this thesis as

$$F_c(t) = \frac{Z(t)}{S} = \int |u|\, dt\ , \tag{3.27}$$

and the units of $F_c(t)$ will be simply called "fuel units". As well, the rate of fuel consumption $R_f(t)$ can be defined as

$$R_f(t) = \frac{d}{dt} F_c(t) = \frac{d}{dt} \int |u|\, dt\ . \tag{3.28}$$

Since $F_c(t)$ is a discontinuous function, $R_f(t)$ is not defined at the discontinuity points. However, a continuous function $F_c^*(t)$ can be defined that best fits the fuel consumption curve and then, the rate of fuel consumption is defined everywhere as a smooth function.

In all cases studied in this thesis, three different classes of behaviour were observed. In the first class, the system eventually reaches a limit cycle similar to a rigid body limit cycle, where the system states remain contained between the switching lines. The resulting rate of fuel consumption is thus minimal and comparable to that of a rigid body and the system is considered stable. In the second class, the position of the spacecraft diverges from the equilibrium and thus the fuel consumption increases with time, leading to a non-zero rate of fuel consumption. Since this rate of fuel consumption is much larger than that of the desired rigid body case, the system is considered unstable, in accordance with the divergence of motion. For the third possible class of behaviour, the spacecraft motion follows a limit cycle of large amplitude due to the excitation of the system flexible modes. As a result, the limit cycle is not contained inside the switching lines and the thrusters are firing continuously, leading to a non-zero rate of fuel consumption comparable to the one obtained when the motion diverges. This type of behaviour will also be considered unstable since it is not desirable from the fuel consumption point of view. These observations lead to the following stability definitions:

Stability Definitions:

1. a **type-1 instability (U1)** will describe an unstable behaviour for which the motion diverges, resulting in a non-zero rate of fuel consumption;

2. a **type-2 instability (U2)** will describe a system where the motion reaches a limit cycle that is not contained inside the switching lines as for a rigid body limit cycle, thus resulting in a non-zero rate of fuel consumption. This system will be classified as unstable, too;

3. a **stable system (S)** will describe a system where the motion reaches a limit cycle similar to a rigid body limit cycle, thus being contained between the switching lines, and resulting in a near-zero rate of fuel consumption as for a rigid body system.

3.7.2 Application

The stability definitions of Subsection 3.7.1 are applied by using either the describing function method or simulation.

For the describing function method, three typical describing function plots are presented below to show the applicability of the stability definitions.

Type-1 Instability

The plot shown in Fig. 3.16 is typical of a type-1 instability. Since all the points of the $-1/N_d(A)$ locus are encircled clockwise by the $G(j\omega)$ locus, they are all unstable according to the Nyquist criterion and the amplitude of the oscillations, A, will increase indefinitely. Therefore, the two intersecting points in Fig. 3.16 represent unstable limit cycles that will never practically be observed.

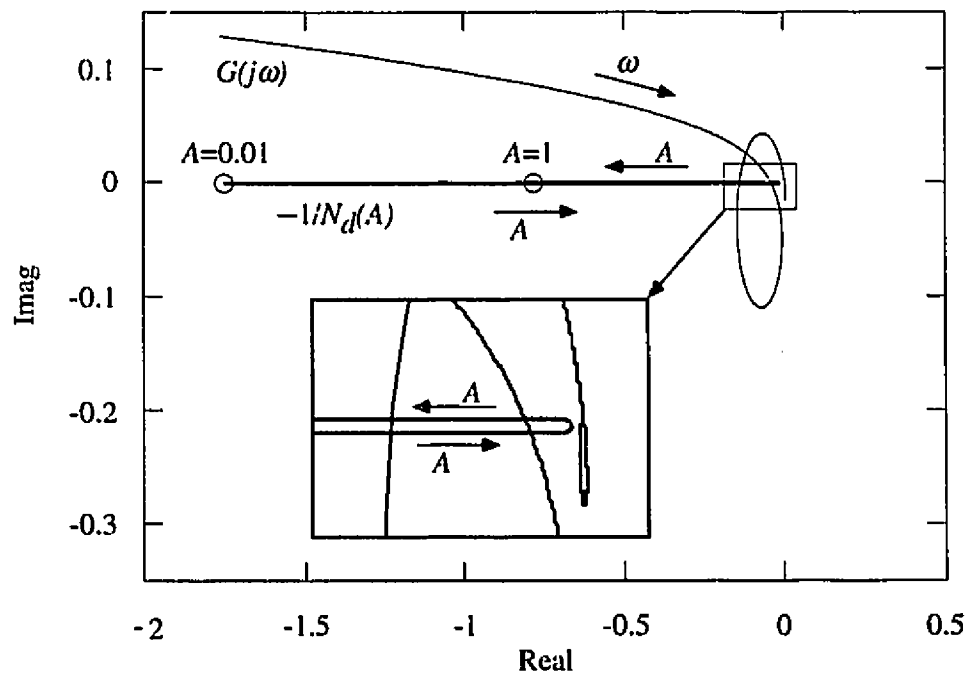

Figure 3.16: Describing function plot for a type-1 instability.

Type-2 Instability

In this case, the plot of Fig. 3.17 represents a type-2 instability. Since all points to the left of the $G(j\omega)$ locus are not encircled clockwise by this locus, they represent a stable zone, while the points to the right of the same locus are unstable points. Two types of behaviour are observed in this plot. First, if we take a point on the $-1/N_d(A)$ locus that corresponds to $A < 0.0101$ m, then the system is stable and the amplitude of the oscillations will decrease till $A = 0.01$ m, that corresponds to

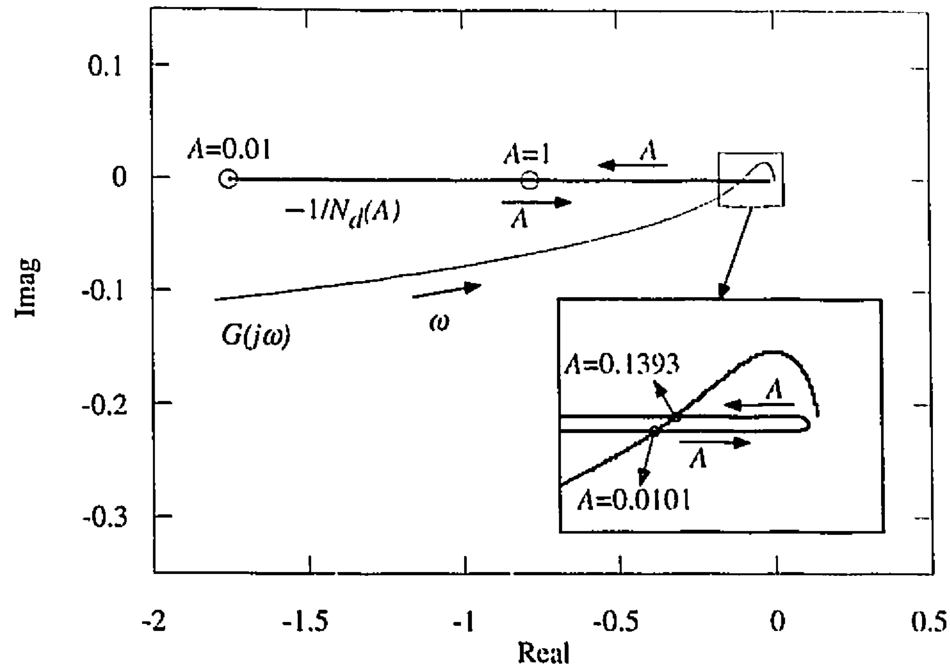

Figure 3.17: Describing function plot for a type-2 instability.

the deadband limit which is the minimum value of A where $-1/N_d(A)$ is defined. Therefore, this corresponds to a stable motion according to the stability definitions of Subsection 3.7.1. However, if the point on the $-1/N_d(A)$ locus corresponds to 0.0101 m $< A <$ 0.1393 m, then this point is unstable and its amplitude will increase. If the amplitude becomes greater than $A = 0.1393$ m, then this point becomes a stable point and the related amplitude will decrease. Therefore, the point corresponding to $A = 0.1393$ m represents a stable limit cycle of amplitude $A = 0.1393$ m, which is not contained between the two switching lines since $A >$ 0.0i m. The actual behaviour of the system will depend upon the initial conditions. However, since the possibility of a type-2 instability is present, the system is classified as being a type-2 instability. Moreover, the stable case is unlikely to happen since the amplitude of the limit cycle, A, must also be greater than the deadband limit, by definition, which is $\delta = 0.01$ m. The zone of stability is therefore very small.

Stable System

A stable system is represented by the describing function plot shown in Fig. 3.18.

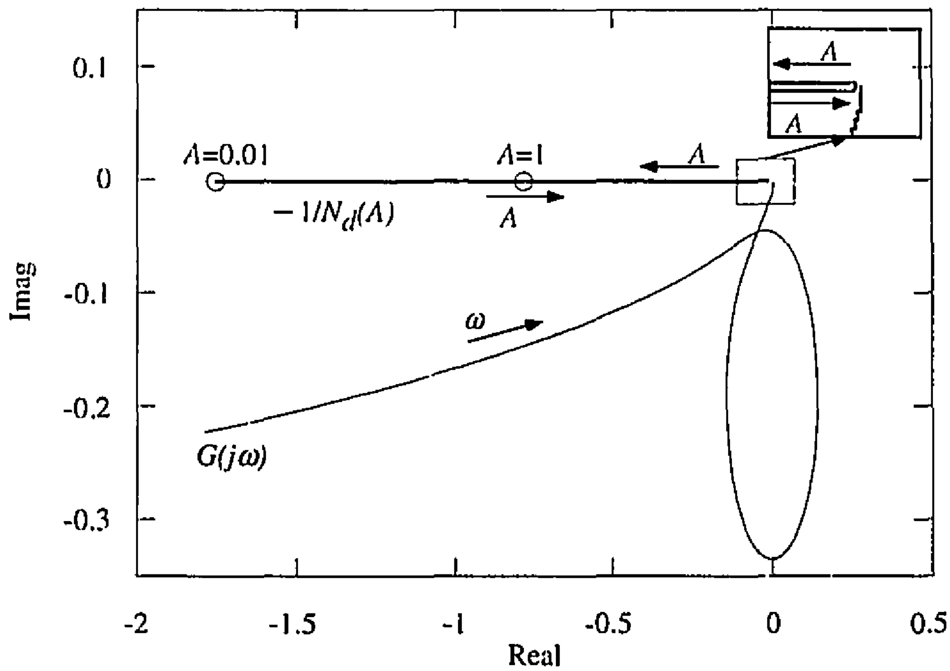

Figure 3.18: Describing function plot for a stable system.

Since no point of the $-1/N_d(A)$ locus is encircled clockwise by the $G(j\omega)$ locus, all the points are stable, and the system exhibits a stable behaviour according to our stability definition. No large-amplitude limit cycles are present in this system because there is no intersection of the two loci and, therefore, a small unavoidable limit cycle due to $\Delta T_{\min}$ will be reached as explained in Subsection 3.3.2.

In the case where simulations are performed, the fuel consumption given by Eq.(3.27) can be obtained easily, by integrating the absolute value of the thrusters command u. The stability definition can be applied qualitatively by looking at this fuel-consumption curve and imagining a continuous curve that fits this curve. If the slope of this continuous curve becomes flat after a while, as the one in Fig. 3.19(a), this means that the rate of fuel consumption is near-zero, and that the system is stable. If this continuous curve has a non-zero slope, as in Fig. 3.19(b), then the system is said to be unstable. The type of unstable behaviour can be determined by examining the error phase plane of the spacecraft to see if the motion diverges as in Fig. 3.19(c), or reaches a large limit cycle that is not contained between the

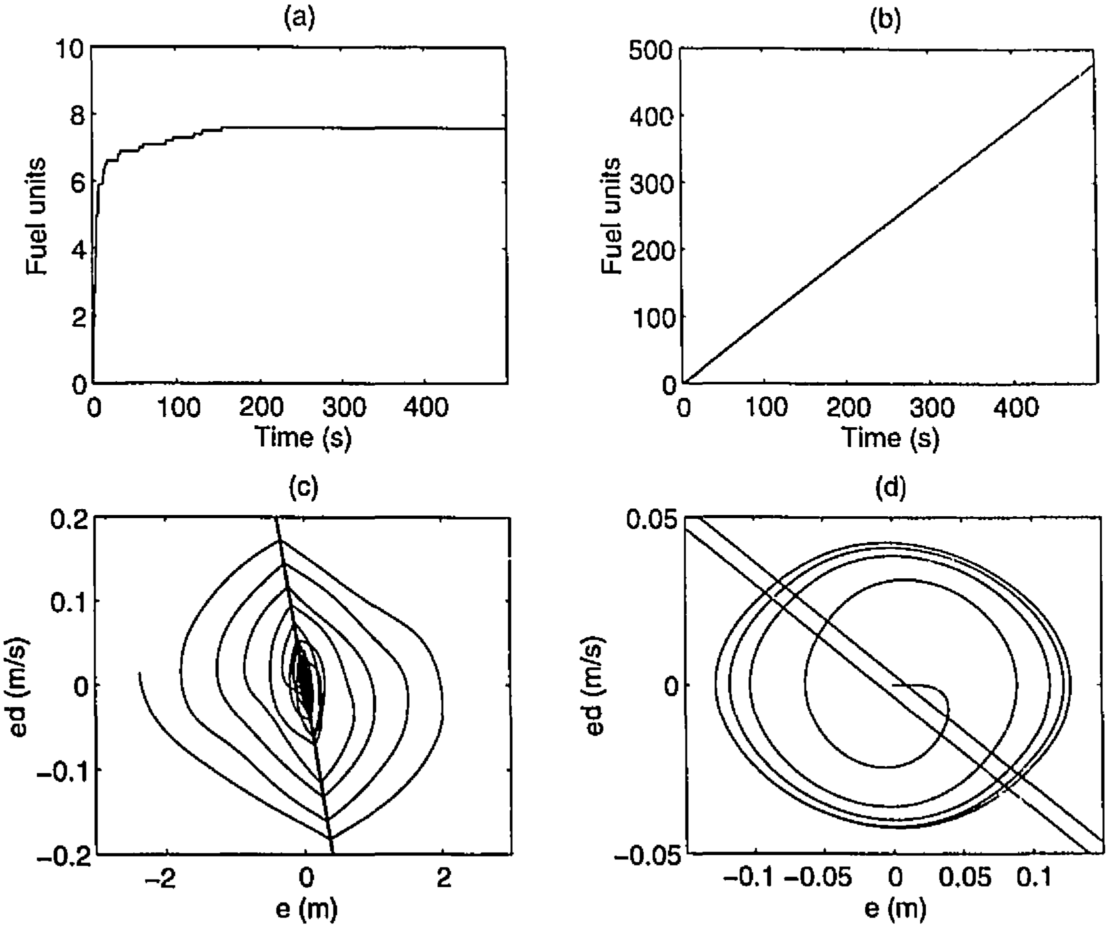

Figure 3.19: Examples of stability determination. (a) Fuel-consumption curve of a stable system, (b) Fuel-consumption curve of an unstable system, (c) Spacecraft error phase plane when the motion diverges, (d) Spacecraft error phase plane when the motion reaches a large limit cycle.

switching lines, as in Fig. 3.19(d).

Chapter 4

Analysis and Discussion

4.1 Introduction

In Chapters 2 and 3, the analysis tools and control models required to study the problem formulated in Section 1.3 were introduced. The analysis of this problem is now adressed in this chapter to allow us draw design guidelines and conclusions. Realistic parameter values are first proposed for the models. These values are next used in a parametric study done using the describing function method. Simulation results are also produced to show the reliability of this approximate method. Conclusions and discussion of this study follow and, finally, the importance of hysteresis, noise and perturbed mass properties are studied in the last three sections.

4.2 Numerical Application

To perform a parametric study using the describing function method, and to simulate the models presented in Section 3.6, numerical values are chosen for all parameters required. Using the approximate characteristics of the CANADARM-Space-Shuttle system, the natural frequencies of the system are also obtained.

4.2.1 Determination of Parameter Values for the Models

In order to perform the parametric study, realistic parameter values must be chosen for the models formulated in Section 3.6. Some parameters like acceleration, time delays, minimum operating time of the thrusters, etc. are taken from the Space Shuttle system as indicative of current space technology.

Plant Parameters

Despite the fact that the CANADARM-Space-Shuttle system is often taken as reference, this thesis does not focus on some particular system. Therefore, the mass of the spacecraft M_1 can be chosen arbitrarily, and is chosen as 500 kg, which is quite small compared to the mass of the Space Shuttle. However, the important point is to use a system acceleration that is reasonable; by a proper choice of the force level of the thrusters, this can be attained, and thus, similar behaviours are obtained. By choosing a small mass for the spacecraft, we show that our analysis is not restricted to the Space Shuttle system, and hence, it can apply to any space robotic system. The manipulator is assumed to have a negligible mass, and since the maximum payload rating for the CANADARM is about 30% of the mass of the Space Shuttle, the ratio of the mass of the payload over the mass of the spacecraft, β, is assumed to vary between 0.01 and 0.3. For the manipulator, the four configurations studied are shown in Fig. 4.1. The configuration in Fig. 4.1(a) is that corresponding to the highest first resonance frequency expected for a specific payload, while the configuration in Fig. 4.1(d) corresponds to the smallest frequency for the same payload. Configurations in Figs. 4.1(b) and (c) yield intermediate frequencies. The second-order structural damping ratio ζ was obtained experimentally for the CANADARM, as reported in (Allen, D'Eleuterio and MacLean, 1994), and is equal to 0.068. It is also possible to extract this parameter from the simulation results of Singer (1989), which give approximately 0.05. In this thesis, we also use $\zeta = 0.05$. As mentioned in Section 3.4, the time delay for the relay operation is neglected since it is small compared to the sensor time delay. This sensor delay is chosen as $\tau = 0.1$ s, which

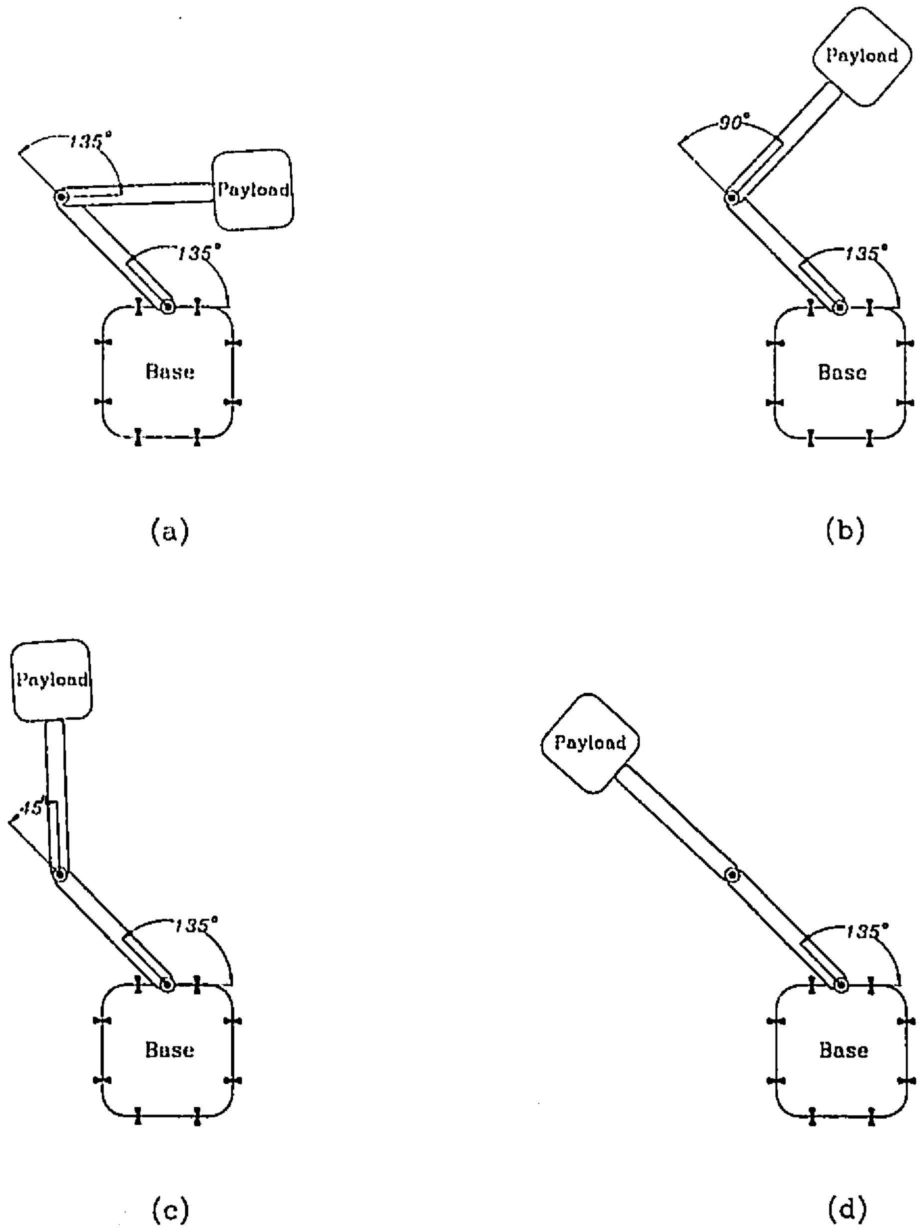

Figure 4.1: Manipulator configurations studied.

is inside the range of current delays for space sensors, order of 80 ms to 300 ms. As example, the Space Shuttle sensors have a delay of $\tau = 0.312$ s (Penchuk, Hattis and Kubiak, 1985).

Controller Parameters

Current on-off thrusters can develop various force levels B, the choice of the required force being dependent upon the system. For this thesis, a 5 N force is assumed to be available to translate the system either in the positive or negative direction and is chosen as the nominal value, while, for the parametric study, the thrusters are assumed to range from 0.1 N to 10 N. Moreover, the deadband attitude limit δ, is also system-dependent. Here, 0.01 m is chosen as the nominal value for δ, while the range for the study is from 0.001 m to 0.1 m. The negative inverse of the slope of the switching lines, λ, is assumed to vary from 0.1 s to 10 s, and the minimum operating time for the thrusters is chosen as $\Delta T_{\min} = 0.1$ s, which is of the same order of magnitude as that for the thrusters of the Space Shuttle, 0.080 s (Nakano and Willms, 1982; Hattis et al., 1982).

State Estimator Parameters

Some of the state estimator parameter values have already been defined in Subsections 3.5.1 and 3.5.2. These are

$$\omega_{sc} = 0.2513 \text{ rad/s}$$
$$\zeta_{sc} = 0.707$$
$$\zeta_f = 0.707 \, .$$

The cutoff frequency of the filters ω_f is varied from 0.2513 rad/s to 4 rad/s. The same range is chosen for the pole placement using the gain **k** of the asymptotic state estimator. Two poles are placed on the negative real axis at the chosen frequency ω_{asym}, while the two other ones are placed symmetrically about the negative real axis for the same frequency, but with a damping coefficient ζ_{asym} of 0.707—see Fig 4.2.

All these parameter values are summarized in Tables 4.1 and 4.2.

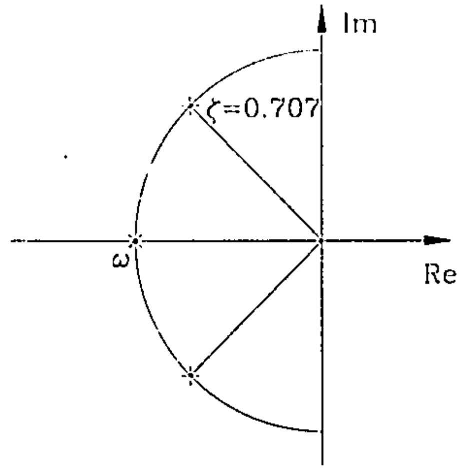

Figure 4.2: Poles placement of the asymptotic state estimator.

M_1	q_1	ζ	τ	$\Delta T_{\min}$	ω_{sc}	ζ_f	ζ_{sc}	ζ_{asym}
500 kg	135°	0.05	0.1 s	0.1 s	0.2513 rad/s	0.707	0.707	0.707

Table 4.1: Fixed-parameter values.

β	$0.01 \leq \beta \leq 0.3$
λ	0.1 s $\leq \lambda \leq 10$ s
B	0.1 N $\leq B \leq 10$ N
δ	0.001 m $\leq \delta \leq 0.1$ m
q_3	$-135°, -90°, -45°, 0°$
ω_f	0.2513 rad/s $\leq \omega_f \leq 4$ rad/s
ω_{asym}	0.2513 rad/s $\leq \omega_{asym} \leq 4$ rad/s

Table 4.2: Free-parameter values.

4.2.2 First Natural Frequency Evaluation of the CANADARM-Shuttle System

The natural frequencies of the manipulator are dependent upon the payload and the configuration of the manipulator. Equation (2.16a) can be used to approximate the first natural frequency of the CANADARM mounted on the Space Shuttle in a specific configuration and for a particular payload. The approximate characteristics of the CANADARM-Space Shuttle system are used to derive the model. The CANADARM, a 6-DOF manipulator, has two long flexible links. If the characteristics of the whole manipulator are lumped around these two flexible links, and the Space Shuttle is assumed to be the base, we obtain the approximate parameters given in Table 4.3. These parameters were obtained as follows: the length of the three first links of the CANADARM (6.6 m, 7.1 m and 1.8 m, respectively) are taken from (Singer, 1989) and their corresponding mass (140 kg, 85 kg and 95 kg, respectively), from (Cyril, 1988). The second and third links are assumed to be rigidly connected as a single link, which corresponds to the second link of our model. Therefore, the centre of mass of this link is at 5.9 m from the beginning of the link. The moment of inertia of the first two links of the CANADARM, with respect to their centre of mass, is approximated by the moment of inertia of a uniform thin rod i.e., $I = ml^2/12$. As well, the moment of inertia of the last link of the CANADARM, with respect to its centre of mass, is approximated using the moment of inertia of a cylinder, i.e., $I = m(r^2/4 + l^2/12)$, and by assuming a radius of $r = 0.25$ m. These calculated values are 508 kg m^2, 357 kg m^2 and 27 kg m^2, respectively, for the first three links of the CANADARM. The moment of inertia of the second link of our model, with respect to its centre of mass, can therefore be obtained from the second and third links values of the CANADARM. Now, considering a point mass payload of βm_0 kg, where β is the ratio of the mass of the payload over the mass of the spacecraft, as defined in Eq.(2.56), the properties of the second link of our model are modified as follows: the centre of mass of the link becomes $x_c = (1062 + 8.9\beta m_0)/(180 + \beta m_0)$, its mass

Body	l_i (m)	r_i (m)	m_i (kg)	I_i (kg m^2)
0		1	75,000	1,635,937
1	3.3	3.3	140	508
2	5.9	3	180	1273
2+Payload	x_c	$8.9 - x_c$	$180 + \beta m_0$	$1273 + 180(x_c - 5.9)^2 + \beta m_0(8.9 - x_c)^2$

Table 4.3: Shuttle, simplified 2-link manipulator and payload parameter values.

$m_2 = 180+\beta m_0$ and its moment of inertia $I_2 = 1273+180(x_c-5.9)^2+\beta m_0(8.9-x_c)^2$.

For the Space Shuttle, a mass $m_0 = 75,000$ kg seems reasonable, since its dry weigth is about 68,000 kg (Lyndon B. Johnson Space Center, 1976). Finally, the moment of inertia of the Space Shuttle was approximated by considering a 37 m long cylinder with a radius of 3.5 m, and using the formula $I = m(r^2/4 + l^2/12)$. The length of 37 m is the actual length of the Space Shuttle (Lyndon B. Johnson Space Center, 1976) and the radius of 3.5 m is an approximate value.

The first two natural frequencies for the CANADARM in the configuration $q_1 = 135°$ and $q_3 = 0°$, without payload are, as mentioned in (Singer, 1989),

$$\omega_1 = 2\pi(0.32) \text{ rad/s} \tag{4.1a}$$

$$\omega_2 = 2\pi(3.2) \text{ rad/s} \tag{4.1b}$$

Substituting Eqs.(4.1) in Eqs.(2.16) with the use of the parameters in Table 4.3 and solving for k_1 and k_2, two sets of solutions are obtained

$$k_{1,1} = 137,086 \text{ Nm/rad} \tag{4.2a}$$

$$k_{2,1} = 295,547 \text{ Nm/rad} \tag{4.2b}$$

or

$$k_{1,2} = 1,228,961 \text{ Nm/rad} \tag{4.3a}$$

$$k_{2,2} = 32,967 \text{ Nm/rad} \tag{4.3b}$$

The first set of solution, $k_{1,1}$ and $k_{2,1}$ of Eqs.(4.2), is considered in the following analysis because the two spring stiffnesses k_1 and k_2 are of the same order of magnitude, which makes more sense, since the two corresponding joints of the CANADARM are similar. Therefore values of Eqs.(4.2) can be used in Eqs.(2.16) to obtain the manipulator natural frequencies for all configurations. Some results for the CANADARM are available in (Singer, 1989), and displayed in Table 4.4 with results obtained using Eqs.(2.16). We see that the error is quite small, and, despite the fact that we lumped all flexibility at the joints, the model gives good agreement with the experiments. Therefore, the parameters given by Eqs.(4.2) will be used in conjunction with Eqs.(2.16) to obtain the configuration-dependent resonance frequencies for the manipulator under study.

q_1 (deg)	q_3 (deg)	First nat. freq. (Hz) CANADARM	First nat. freq. (Hz) Using Eqs.(2.16)	Error (%)
135	0	0.32	0.32	0
135	-45	0.35	0.34	3
135	-90	0.45	0.43	4
135	-135	0.8	0.65	19

Table 4.4: First resonance frequency comparison.

Using Eq.(2.16a), the set of first natural frequencies, for the range of β and the specific configurations q_1 and q_3 used in the parametric study, are given in Table 4.5, where the ratio of the highest frequency to the lowest one is 5 to 1. Making use of the damping ratio ζ, these frequencies are substituted in Eqs.(2.49) and (2.50) to obtain the required spring stiffness k and damping coefficient c for the simplified model formulated in Section 2.3.

4.3 Results of the Parametric Study

A parametric study, using the describing function technique, is next performed for all three models considered in this thesis. System stability is investigated as done in

β	$q_3 = -135°$	$q_3 = -90°$	$q_3 = -45°$	$q_3 = 0°$
0.01	0.255	0.170	0.136	0.127
0.05	0.128	0.090	0.075	0.071
0.1	0.097	0.072	0.062	0.059
0.15	0.083	0.065	0.057	0.054
0.2	0.076	0.061	0.054	0.052
0.25	0.071	0.058	0.052	0.050
0.3	0.067	0.056	0.051	0.049

Table 4.5: First natural frequency evaluation (Hz).

the typical examples of Subsection 3.7.2.

To validate the results obtained by the describing function method, a large number of simulations have been performed using *Simulink*, a *Matlab* package. More attention was given to critical points, which differentiate unstable from stable behaviour. In general, simulation results confirmed those obtained by the describing function method. However, for some conditions, the conclusions based on the describing function method were false. In those cases, simulations for conditions near the ones that gave false results gave results that were in agreement with the describing function predictions. Since we are only concerned with the general trends and not with accurate values, conclusions based on describing functions remain acceptable.

In the following subsections, the results of the parametric study are discussed with the results of one simulation for each of the three models studied. The three simulation cases studied are typical of the three possible types of behaviour described in Subsection 3.7.1. In all simulations reported in this chapter, an initial error of 0.05 m was assumed for both the position of the spacecraft and the position of the payload. The controller was then used to try to bring the spacecraft within the deadband limits.

4.3.1 Case 1: Model with Position and Velocity Filters

The results of the describing function analysis for the model with position and velocity filters, which is shown in Fig. 3.13, are summarized in Tables 4.6, 4.7 and 4.8. In these tables, "U1" means an unstable system of type-1, "U2" an unstable system of type-2, and "S" a stable system. For this model, the flexibility level in the system does not play an important role in stability determination. If a system is stable for a high-frequency case, it is also stable for a low-frequency case, for the same parameter values. This conclusion is also valid for an unstable system. Therefore, the results displayed in Tables 4.6, 4.7 and 4.8 are valid for the whole range of β and q_3 values studied.

	λ (s)								
ω_f (rad/s)	0.1	0.5	1	2	3	4	5	7	10
0.2513	U1	U1	U1	U1	U1	U1	U1	U2	U2
0.4700	U1	U1	U1	U1	U1	U2	U2	U2	U2
0.6911	U1	U1	U1	U1	U2	U2	U2	U2	U2
1	U1	U1	U1	U2	U2	U2	U2	U2	U2
2	U1	U1	U2	U2	U2	U2	U2	U2	U2
3	U1	U1/U2	S	S	S	S	U2	U2	U2
4	U1	S	S	S	S	S	S	U2	U2
10	U1	S	S	S	S	S	S	S	S

where U1 = Type-1 instability
U2 = Type-2 instability
S = Stable system

Table 4.6: Stability as a function of λ and ω_f ($B = 5$ N, $\delta = 0.01$ m).

In Table 4.6, the force level B of the thrusters and the deadband limits δ are fixed to 5 N and 0.01 m, respectively. We can see that, for a given cutoff frequency ω_f smaller or equal to 2 rad/s, the system is unstable for all λ values, either by a type-1 or a type-2 instability. A small λ results in type-1 instability, while a larger λ results in type-2 instability. Moreover, the greater ω_f, the smaller the λ separating

δ (m)	B (N)				
	0.1	0.5	1	5	10
0.001	U1	U1	U1	U1	U1
0.01	U1	U1	U1	U1	U1
0.05	U1	U1	U1	U1	U1
0.1	U1	U1	U1	U1	U1

where U1 = Type-1 instability

Table 4.7: Stability as a function of B and δ ($\omega_f = 0.47$ rad/s, $\lambda = 3$ s).

δ (m)	B (N)				
	0.1	0.5	1	5	10
0.001	S	S	U2	U2	U2
0.01	S	S	S	S	U2
0.05	S	S	S	S	S
0.1	S	S	S	S	S

where U2 = Type-2 instability
S = Stable system

Table 4.8: Stability as a function of B and δ ($\omega_f = 3$ rad/s, $\lambda = 3$ s).

the type-1 and type-2 instability zones. If ω_f is increased further, i.e., if $\omega_f > 2$ rad/s, a stable system for intermediate values of λ can be obtained. Moreover, the range of allowable λ values for stability increases as ω_f increases. Therefore, for the model with position and velocity filters, ω_f should be greater than 2 rad/s for a possible stable behaviour, as large as possible to increase the possibility of obtaining a stable system. However, filters are designed to eliminate high-frequency noise; if the cutoff frequency ω_f is too large, noise will pass through the filters and they will not be effective. The proper choice of ω_f will thus depend upon the quality of the available sensors and the need for filtering.

From Table 4.7, where ω_f is fixed to 0.47 rad/s and λ to 3 s, it is noted that the variation of B and δ has no effect on the stability of the system. In all cases, the system exhibits a type-1 instability. However, in Table 4.8, we can see that, for a larger cutoff frequency, say, $\omega_f = 3$ rad/s, the system is stable for low values of B, as expected. The stability zone is also extended by the choice of a larger deadband limit δ. Therefore, δ should be chosen as large as possible, being limited by the amount of attitude error that is allowed in the system. The thruster force B should be chosen as small as possible, without being saturated by base reaction forces induced by possible motions of the manipulator. In other words, B should be high enough to compensate for all base-reaction disturbances.

A simulation has been conducted using the parameters of Tables 4.1 and 4.9 for this model, the results being shown in Fig. 4.3. From Figs. 4.3(b) and (c), we can see that the thrusters are firing continuously, which results in a high total fuel consumption of 478.9 fuel units, and a non-zero rate of fuel consumption. Therefore, the system can be classified as unstable. Moreover, by looking at the phase plane trajectories in Fig. 4.3(a), the instability is said to be of type-2, since a limit cycle that is not contained inside the switching lines is reached. Hence, this agrees with the describing function results of Table 4.6 for $\omega_f = 0.6911$ rad/s and $\lambda = 3$ s.

β	λ	B	δ	ω_n	ω_f
0.01	3 s	5 N	0.01 m	$2\pi(0.255)$ rad/s	0.6911 rad/s

Table 4.9: Free-parameter values for a type-2 instability.

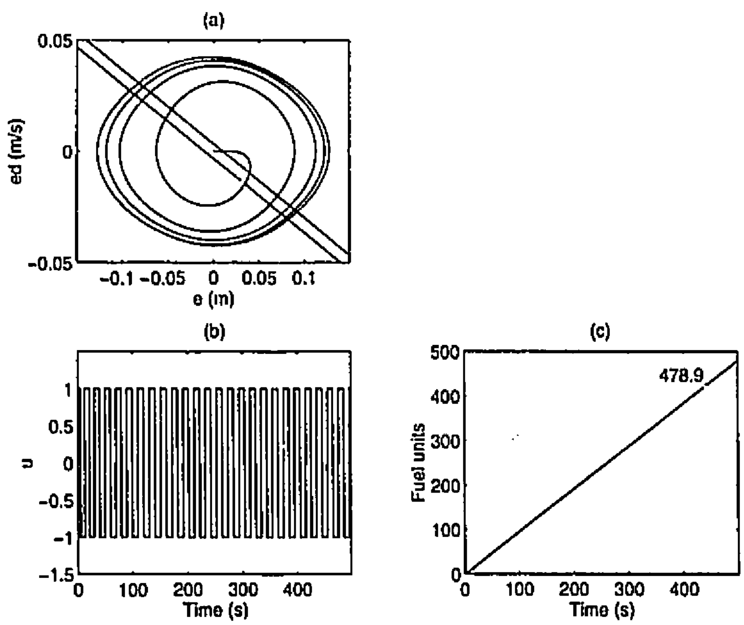

Figure 4.3: Simulation results for a type-2 instability. (a) Spacecraft error phase plane, (b) Thruster command history, (c) Fuel consumption.

4.3.2 Case 2: Model with a Velocity Estimator and a Position Filter

If a velocity estimator and a position filter are used, as for the model of Fig. 3.14, the flexibility level in the system is very important for stability determination. Since the conclusion about the stability of a system for a particular set of β and q_3 values can be different than the conclusion about the stability for the same system, but with another set of β and q_3 values, it is not possible to present the results in the same form as in Subsection 4.3.1. In this case, all free parameters are studied separately with the aid of a stability map.

The stability map studying the effect of the cutoff frequency ω_f of the position filter is presented in Fig. 4.4(a) by setting λ, B and δ equal to 3 s, 5 N and 0.01 m, respectively. Each curve in this stability map represents a stability boundary for a given ω_f. The region above a stability boundary is a zone of instability either by type-1 or type-2, while the region below the boundary is a zone of stability. We can see that the stability zone is augmented by increasing ω_f, since the stability boundary moves up. For $\omega_f \geq 1$ rad/s, the system is stable for all β and q_3 values studied. Therefore, ω_f should be chosen as large as possible, while keeping in mind the noise reduction problem.

In the stability map of Fig. 4.4(b), parameters ω_f, λ and δ are fixed to 0.47 rad/s, 3 s and 0.01 m, respectively, to study the effect of the force level B developed by the thrusters. For low force, i.e., $B = 0.1$ N, the system is always unstable (for $\beta \geq 0.01$). However, for a small increase in B, $B = 0.5$ N, the stability zone is increased significantly. This stability zone is subsequently reduced if B further increases, and, finally, maintains the same level for $B \geq 5$ N. In this case, the best parameter choice is probably $B \geq 5$ N, since at lower force levels, there is a jump between stability and instability zone. This kind of jump phenomena should be avoided to eliminate the possibility of instability in a real physical system.

The effect of the negative inverse of the slope of the switching lines λ is studied

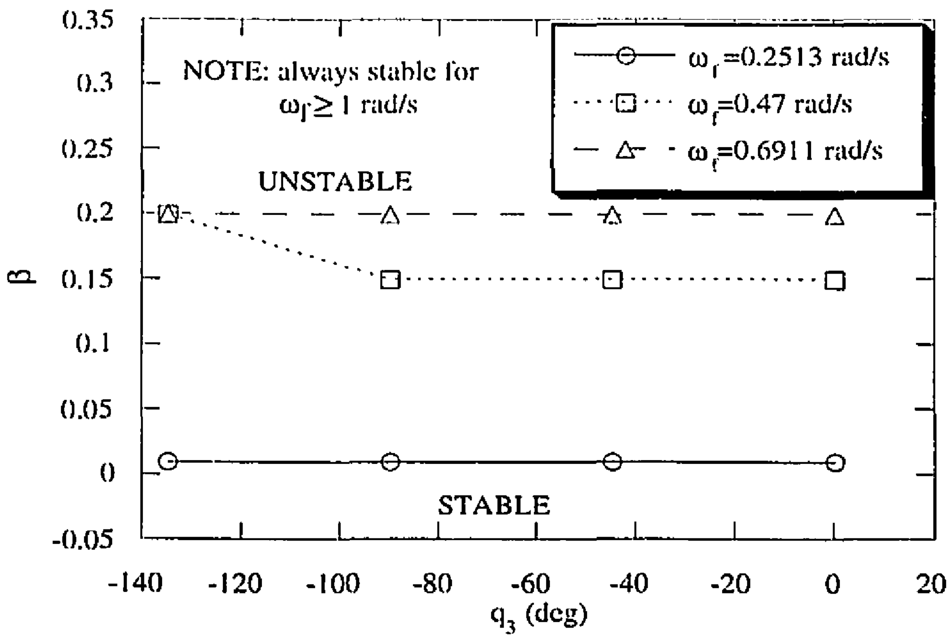
0.35
0.3
0.25
0.2
0.15
0.1
0.05
0
-0.05
β
NOTE: always stable for
$\omega_f \geq 1$ rad/s
UNSTABLE
STABLE
ω_f=0.2513 rad/s
ω_f=0.47 rad/s
ω_f=0.6911 rad/s
-140
-120
-100
-80
-60
-40
-20
0
20
q_3 (deg)

(a)

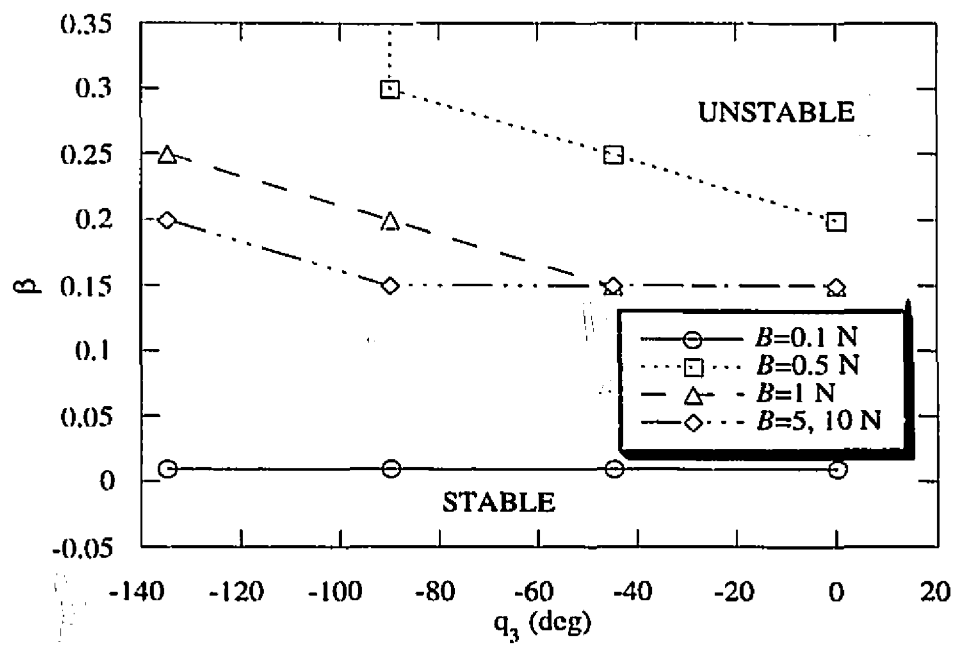
0.35
0.3
0.25
0.2
0.15
0.1
0.05
0
-0.05
β
UNSTABLE
STABLE
B=0.1 N
B=0.5 N
B=1 N
B=5, 10 N
-140
-120
-100
-80
-60
-40
-20
0
20
q_3 (deg)

(b)

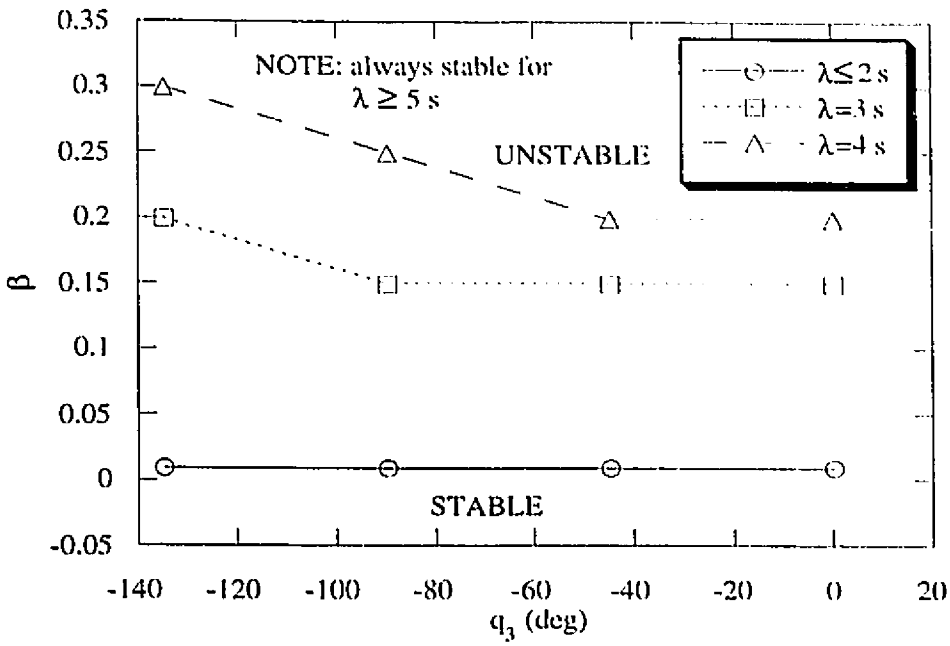

(c)

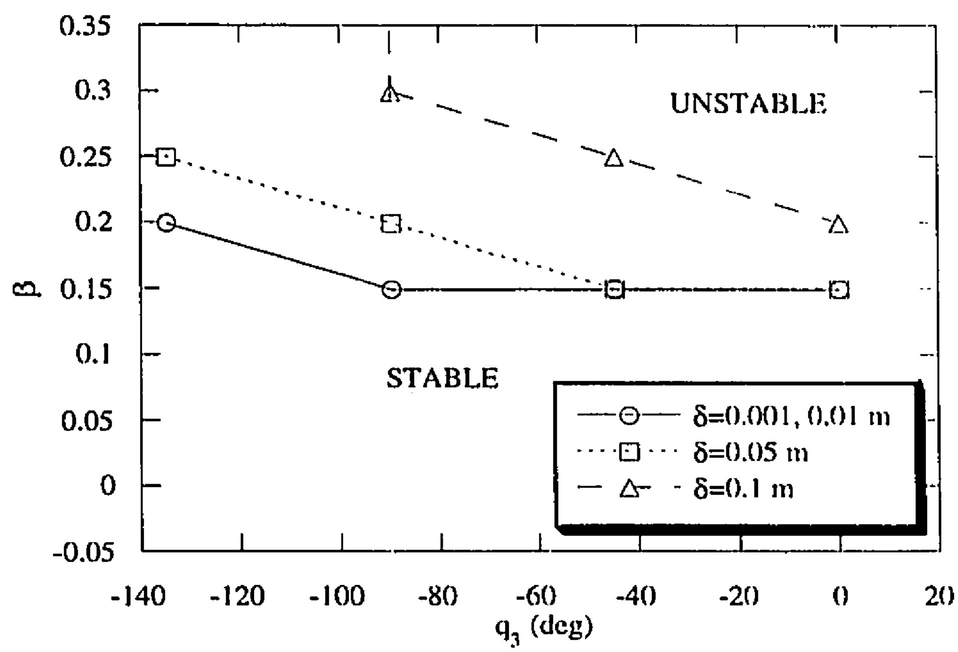

(d)

Figure 4.4: Describing function stability maps. (a) Effect of ω_f, (b) Effect of B, (c) Effect of λ, (d) Effect of δ.

in the stability map of Fig. 4.4(c). For this study, the parameters ω_f, B and δ are fixed to 0.47 rad/s, 5 N and 0.01 m, respectively. For $\lambda \leq 2$ s, the system is always unstable and the stability zone is enlarged with an increase in λ. For $\lambda \geq 5$ s, the system becomes stable for all cases studied. Therefore, an obvious choice is to select a large λ, which means that the velocity feedback is more weighted, to obtain stability in all possible configurations and payloads.

Finally, the stability map of Fig. 4.4(d) presents the effect of the deadband limits δ by setting ω_f, λ and B to 0.47 rad/s, 3 s and 5 N, respectively. As observed with the model studied in Subsection 4.3.1, the stability zone increases with a larger δ. However, for the fixed-parameters of ω_f, λ and B, it seems impossible to obtain a full stability area while keeping δ in a reasonable range, because there is no δ for which the system is always stable for all configurations and payloads.

It is important to note that the maps of Fig. 4.4 are approximate, since only a few β and q_3 values were studied. It should be possible to obtain more precise maps by reducing the interval of variation of the parameters for each stability analysis. However, the conclusion would be the same, since we are only examining the trend of increasing a certain parameter value and not specific point values.

The free-parameter values of Table 4.10 have been used, with the fixed-parameter values of Table 4.1, to run the simulation model. The results obtained are displayed in Fig. 4.5. By examining the phase plane portrait of Fig. 4.5(a), we can see that the amplitude of the motion is diverging since the initial error was 0.05 m. This behaviour is typical of a type-1 instability. Moreover, we observe from Figs. 4.5(b) and (c) that the thrusters are firing continuously and that the total fuel consumption is very high, namely, 466.5 fuel units. A conclusion about stability can also be drawn by looking at the slope of the fuel-consumption curve in Fig. 4.5(c). Since the slope is non-zero, we can conclude that the system is unstable according to the stability definition of Subsection 3.7.1, which is the same conclusion reached with the describing function method, looking at Fig. 4.4(c) for $\lambda = 2$ s.

β	λ	B	δ	ω_n	ω_f
0.3	2 s	5 N	0.01 m	$2\pi(0.067)$ rad/s	0.4700 rad/s

Table 4.10: Free-parameter values for a type-1 instability.

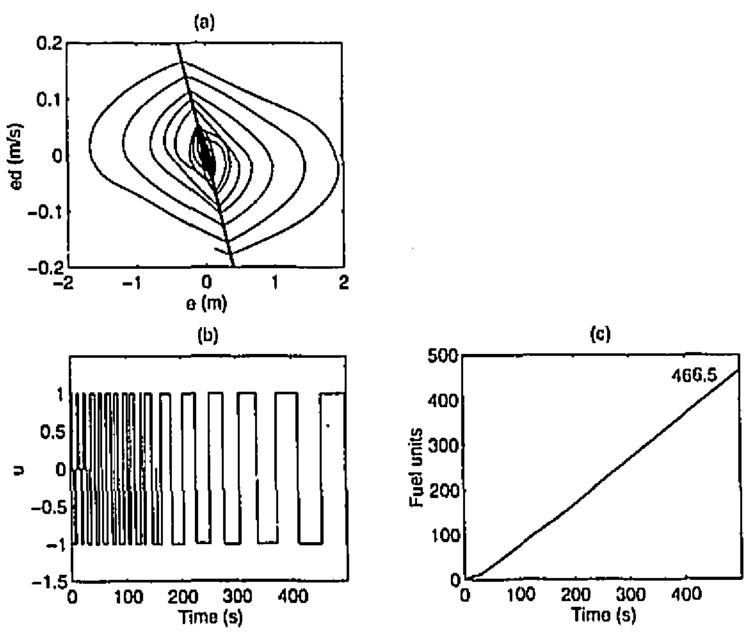

Figure 4.5: Simulation results for a type-1 instability. (a) Spacecraft error phase plane, (b) Thruster command history, (c) Fuel consumption.

4.3.3 Case 3: Model with an Asymptotic State Estimator

The use of an asymptotic state estimator, as in the model of Fig. 3.15, gives very interesting results. Using the describing function technique, it was found that the system was almost always stable for all β and q_3 values, and for all free-parameter values studied. Only a few instability cases were obtained at low values of λ. Therefore, the performance of the reaction control system is increased significantly with the use of this model. All the stable cases studied are reported in Table 4.11, while the unstable cases in Table 4.12. For cases in Table 4.11, the stability conclusion is valid for all β and q_3 values studied in this thesis. The results of Table 4.12 can also be illustrated with the stability map of Fig. 4.6, using $\omega_f = 0.7230$ rad/s, $B = 5$ N and $\delta = 0.01$ m.

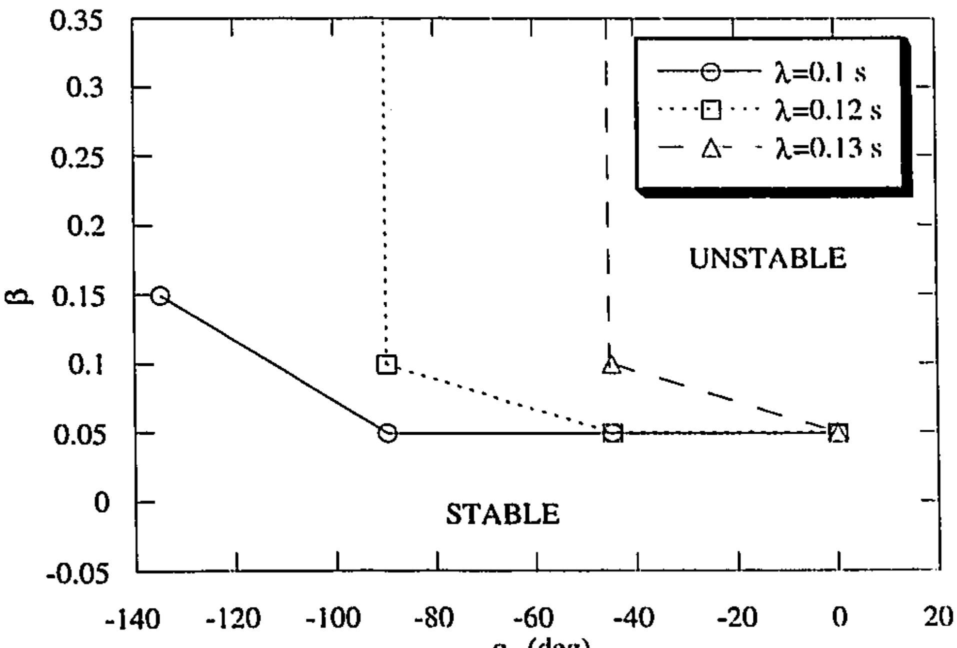

Figure 4.6: Stability map for the model with an asymptotic state estimator.

The system was simulated using the parameters of Table 4.13, again with the fixed-parameters of Table 4.1. The results are illustrated in Fig. 4.7. From Figs. 4.7(a) and (b), it can be seen that a small limit cycle that is contained between the switching lines is reached, corresponding to a stable case. One can note that the motion

ω_f (rad/s)	B (N)	δ (m)	λ (s)
0.2513	5	0.01	3
0.7230	0.1	0.01	3
0.7230	0.5	0.01	3
0.7230	1	0.01	3
0.7230	5	0.01	3
0.7230	5	0.01	0.15
0.7230	5	0.01	0.5
0.7230	5	0.01	1
0.7230	5	0.01	2
0.7230	5	0.01	3
0.7230	5	0.01	4
0.7230	5	0.01	5
0.7230	5	0.01	7
0.7230	5	0.01	10
0.7230	5	0.05	3
0.7230	5	0.1	3
0.7230	10	0.01	3
1	5	0.01	3
2	5	0.01	3
3	5	0.01	3
4	5	0.01	3

Table 4.11: Stable cases for the model with an asymptotic state estimator.

ω_f (rad/s)	B (N)	δ (m)	λ (s)	β	q_3 (deg.)
0.7230	5	0.01	0.1	≥ 0.15	-135
0.7230	5	0.01	0.1	≥ 0.05	-90
0.7230	5	0.01	0.1	≥ 0.05	-45
0.7230	5	0.01	0.1	≥ 0.05	0
0.7230	5	0.01	0.12	≥ 0.1	-90
0.7230	5	0.01	0.12	≥ 0.05	-45
0.7230	5	0.01	0.12	≥ 0.05	0
0.7230	5	0.01	0.13	≥ 0.1	-45
0.7230	5	0.01	0.13	≥ 0.05	0

Table 4.12: Unstable cases for the model with an asymptotic state estimator.

β	λ	B	δ	ω_n	ω_{asym}
0.3	2 s	5 N	0.01 m	$2\pi(0.049)$ rad/s	0.7230 rad/s

Table 4.13: Free-parameter values for a stable system.

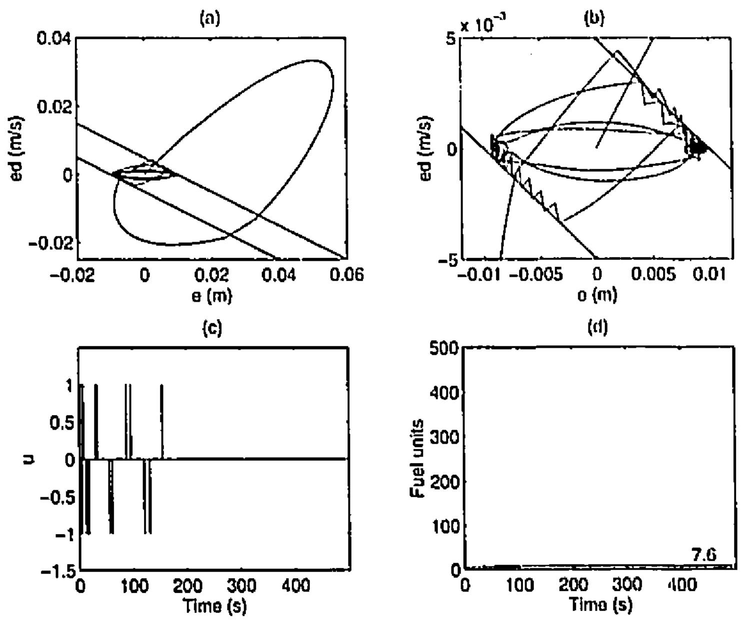

Figure 4.7: Simulation results for a stable system. (a) Spacecraft error phase plane, (b) Spacecraft error phase plane (zoom), (c) Thruster command history, (d) Fuel consumption.

appears to be concentrated at the left side of Fig. 4.7(b) in a spiral motion. However, if the simulation is run for a larger period, the right switching line will eventually be reached and thus, a firing will occur, then reactiving the small limit cycle. This longer simulation run was not performed in order to maintain consistency in the results presentations and, since the velocity is very small, the time required can be quite significant. Figs. 4.7(c) and (d) are also typical of a stable system, since the thrusters are not firing continuously and the fuel-consumption curve is flat, thereby resulting in a near-zero rate of fuel consumption. In this case, the total fuel consumption is very small, with only 7.6 fuel units.

4.4 Conclusions and Discussion of the Describing Function Studies

The conclusions of the parametric study of Section 4.3 are the same for all three models studied. They are summarized below:

1. the cutoff frequency ω_f for the low-pass filters should be chosen as large as possible to avoid instability;

2. a small velocity gain λ can result in instability in the system; therefore, a large λ should be selected. However, one must be careful, since a large λ may lead to a type-2 instability for case 1, where the model with position and velocity filters is used;

3. the force level B of the thrusters should be chosen small for stability. Unstable types of behaviour are more likely to occur for large B. However, one must be careful because the system can be unstable for a very low thrust level as, for example, in the case of the model with a velocity estimator and a position filter (always unstable when $B = 0.1$ N);

4. deadband limits δ should be chosen as large as possible to avoid instability in the system.

Physical interpretations of these conclusions are given below.

A filter is designed to reject the noise in a signal. If a low cutoff frequency is chosen, the filtering effects will be better, but lag will be introduced in the system. This lag can have similar effects to delays, i.e., it can change the effective slope of the switching lines—see Section 3.3.3. If this lag becomes so significant that the slope of the switching lines becomes positive, then an unstable behaviour of type-1 is obtained, since the amplitude of the motion will always increase. Lag effects can also explain the increase of type-2 instabilities with an increase of ω_f. When lag is present, more and longer firings are necessary to bring the system to equilibrium. Since the natural frequencies are rather low, longer firing periods can more easily excite these modes. As well, many firings are more likely to excite flexible modes than a few firings. Therefore, the first conclusion of the describing function analysis seems quite reasonable physically.

The first part of the second conclusion can be explained by similar arguments. If λ is small, i.e., if the slope of the switching lines is large, a small lag can change this slope to a large positive value, thereby resulting in an unstable system of type-1. Increased chance for a type-2 instability when λ is not very small seems also quite reasonable. When λ is large, which corresponds to a small slope of the switching line, the chattering phenomenon introduced in Subsection 3.3.3 is more likely to become significant, thereby resulting in more subsequent firings, and, therefore, in flexible-mode excitation. However, this conclusion is not valid in case 2, where the model with a velocity estimator and a position filter is studied. In this case, when λ is increased, there are less possibilities of obtaining a type-2 instability. This is contradictory and means that other phenomena play a more significant role in the system. No explanation is currently available: more research is required to understand this phenomenon.

The third conclusion on the effect of the force level B of the thrusters can also be explained physically. When the thruster force is large, a single impulse of thrusters is more likely to excite the flexible modes of the system, since the impact is more profound. However, the reasons why instabilities can result with very low force levels are less obvious. A tentative explanation is that, if the force is low, then the thrusters have to fire for a longer period. These longer jet firings can lead to low frequency excitation, thereby resulting in an instability of type-2.

Finally, the fourth conclusion can be easily explained. If the deadband limits are larger, then there is more off-time between firings, therefore resulting in less subsequent firings. It is thus more unlikely to excite the flexible modes in the system.

Throughout this section, it was shown that the trend of the parameter values obtained by the describing function analysis make sense physically. This physical understanding is significant when establishing confidence in the approximate method. Simulation results were also reported; these confirmed the relatively good accuracy of the method for behaviour prediction.

4.5 Importance of Hysteresis

In the describing function plots of Subsection 3.7.2, no hysteresis was included in the controllers. However, if 20% of hysteresis is added to the controller of the example for a type-2 instability, which means that $\Delta = 0.002$ m (Fig. 3.5), the plot of Fig. 4.8 is obtained, where subscripts d and h refer to the relay without and with hysteresis respectively. The describing function representing the relay without hysteresis is also included for comparison. We can see that the intersecting points corresponding to the two curves, with and without hysteresis, are very close and correspond to the same amplitude for the predicted limit cycle, i.e., $A = 0.1393$ m. The major difference is that, if hysteresis is present, there is no possibility for a stable system, while stable responses were possible in the case without hysteresis. However, as explained in Subsection 3.7.2, the system is considered unstable because there are possibilities for unstable responses. Therefore, the conclusion on system stability is the same and independent of the presence or lack of hysteresis.

Intuitively, the same conclusion is drawn by considering that hysteresis is actually included in the control system to avoid excessive firings of the thrusters, as explained in Subsection 3.3.3. However, when a large limit cycle is reached, the thrusters are firing for quite a large period and, hence, the hysteresis does not play an important role. Since we are only concerned about system stability, it is not necessary to include hysteresis for the research conducted in this thesis.

To verify this conclusion, the same model that was simulated in Subsection 4.3.1 using the parameters of Tables 4.1 and 4.9 was simulated including 20% of hysteresis

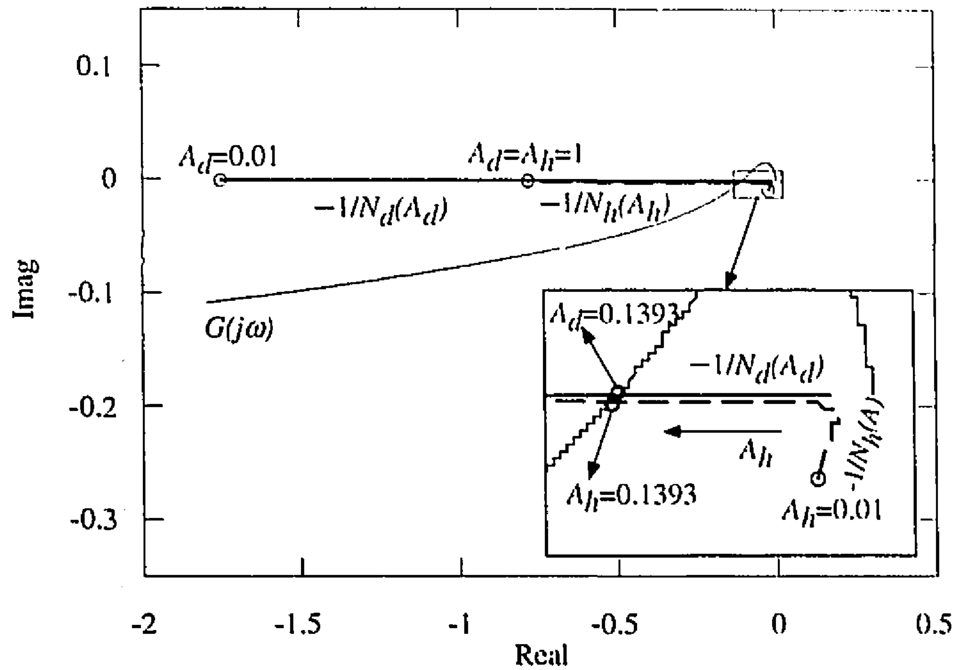

Figure 4.8: Describing function plot with and without hysteresis.

to the controller. The results, illustrated in Fig. 4.9, are almost the same as those of Fig. 4.3 for the case without hysteresis. The total fuel consumption is slightly higher in the case where hysteresis is included, i.e., 483.9 fuel units instead of 478.9 fuel units. Again, this shows that, for the problem at hand, hysteresis does not play an important role. Since this situation is typical of all cases studied, hysteresis was not included further in this thesis.

4.6 Effects of Noise

In the describing function analysis of Section 4.3, it was not possible to include noise in the system. Therefore, to complete the study, the effect of noise is investigated in this section by introducing white noise into the sensor readings of the simulation models. Since we are not dealing with any particular system, the amount of noise is not known, because this is dependent upon the quality of the sensors. For this reason, we assume some reasonable values for the parameters of the noise. White

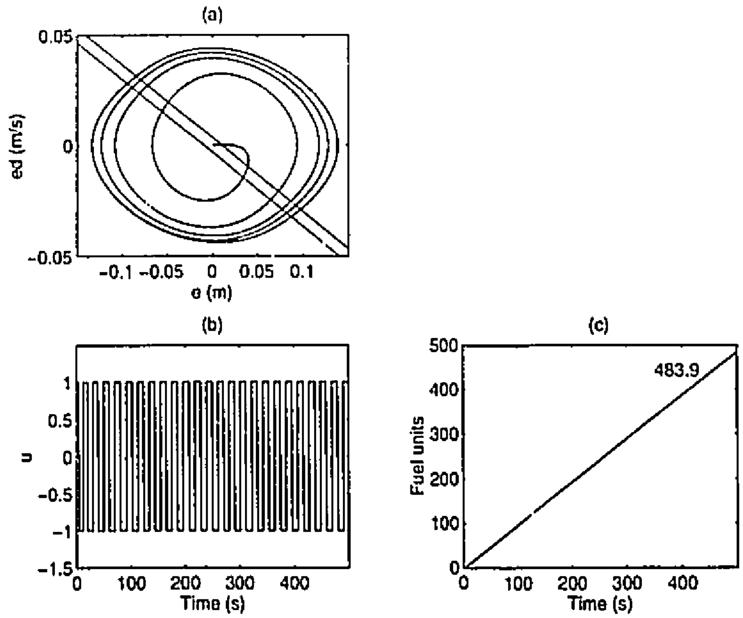

Figure 4.9: Simulation results for a type-2 instability with an hysteretic controller. (a) Spacecraft error phase plane, (b) Thruster command history, (c) Fuel consumption. To be compared with Fig. 4.3.

noise is assumed: this means that the noise is normally distributed with a variance σ_{noise} and a zero mean $\mu_{noise} = 0$ m. The *Simulink* white noise generator block was used to generate the noise into the models. The noise variance was selected to be 20% of the variance of a stable system motion, which is quite a large noise level, since typical values are of the order of 10%. For deadband limits from $\delta = -0.01$ m to $\delta = 0.01$ m, the variance of the stable motion becomes

$$\sigma_{motion} = \frac{(0.01) - (-0.01)}{6} = 0.00333333 \text{ m} . \tag{4.4}$$

The variance of the noise is thus chosen as

$$\sigma_{noise} = 0.2\sigma_{motion} = 0.00066666 \text{ m} . \tag{4.5}$$

If the free-parameters of Table 4.14, corresponding to the most flexible case studied, are chosen for the model with a velocity estimator and a position filter, the resulting motion should be stable according to Fig. 4.4(a), since $\omega_f \geq 1$ rad/s, and

β	λ	B	δ	ω_n	ω_f
0.3	3 s	5 N	0.01 m	$2\pi(0.049)$ rad/s	3 rad/s

Table 4.14: Free-parameter values for the noisy stable system.

a small limit cycle is expected. The simulation model was run using these parameters and white noise of variance $\sigma_{noise} = 0.00066666$ m was added to the system. The results shown in Fig. 4.10 indicate a stable system. Again, for consistency, the model was run for only 500 s, resulting in motion near the zero velocity at the right of Fig. 4.10(b). However, a small limit cycle is expected if the motion is run for a longer period. We can see that even if the cutoff frequency of the filter is chosen large, i.e., $\omega_f = 3$ rad/s, which results in poor filtering effect and a fast response, the motion is also stable with the addition of noise. This result is typical of all results obtained and indicates that it is not necessary to have a large filtering to obtain a stable system. However, in the case 2 where the model with a velocity estimator and a position filter is used, the position signal used to obtain an estimate of the velocity must be filtered since a differentiator is used, which would result in a very noisy estimate. This comment explains why the attitude controller of the Space Shuttle uses a very small cutoff frequency of $\omega_f = 0.2513$ rad/s for the rate estimator, while using basically the unfiltered measurement values for the attitude (Sackett and Kirchwey, 1982). In this kind of nonlinear system, unfiltered signals can still give good performance because they do not pass through the controller as in a linear system. The controller, which only has three output values, either $+1$, 0 or -1 is, therefore, a very good filter as far as the noise reduction is concerned, and thus, always has a clean output signal.

For the case 1 where the model with position and velocity filters is used, it was shown in Subsection 4.3.1 that the system was always unstable for low cutoff frequencies and can be stable for high cutoff frequencies. However, at the limit, if the filters are completely removed, a stable system is possible even in the presence of

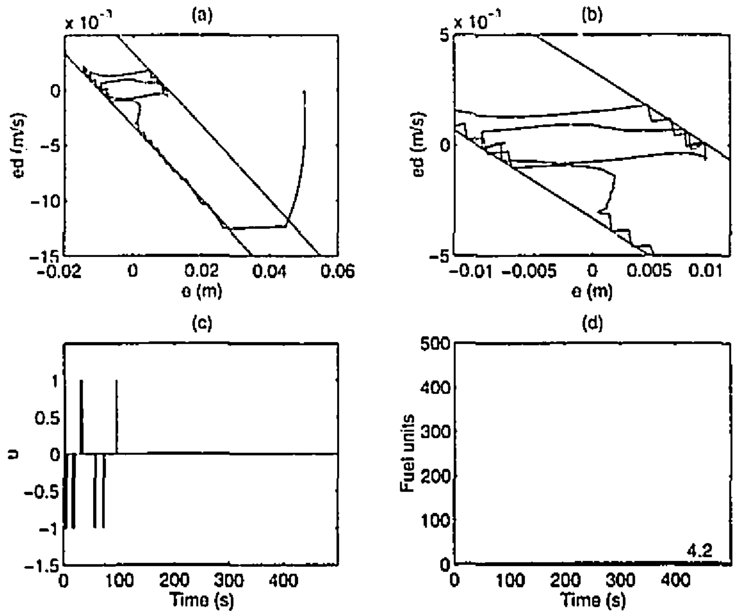

Figure 4.10: Simulation results for a noisy stable system (σ_{noise} = 0.00066666 m). (a) Spacecraft error phase plane, (b) Spacecraft error phase plane (zoom), (c) Thruster command history, (d) Fuel consumption.

noise. Simulation results for such cases are included in Fig. 4.11 using the parameters of Table 4.15. The resulting motion near the equilibrium is obviously very noisy, but still the system behaviour is stable, as seen in Fig. 4.11(d), by considering the fuel-consumption curve. Therefore, the model with position and velocity filters can still be useful, and possesses interesting performance, even if it was almost always unstable in the study of Subsection 4.3.1. However, one must be careful with this model, because, if the noise level in the sensor readings is more significant, let us say, if the variance of the noise is 50% of the variance of the stable motion, i.e. $\sigma_{noise} = 0.00166667$ m, the same system can become unstable, as shown in Fig. 4.12. Hence, it is always more secure to use filters, even with a large cutoff frequency, to eliminate high-frequency noise. The actual usefulness of this model will depend upon the quality of the sensors available.

β	λ	B	δ	ω_n
0.3	3 s	5 N	0.01 m	$2\pi(0.049)$ rad/s

Table 4.15: Free-parameter values for the noisy system without filters.

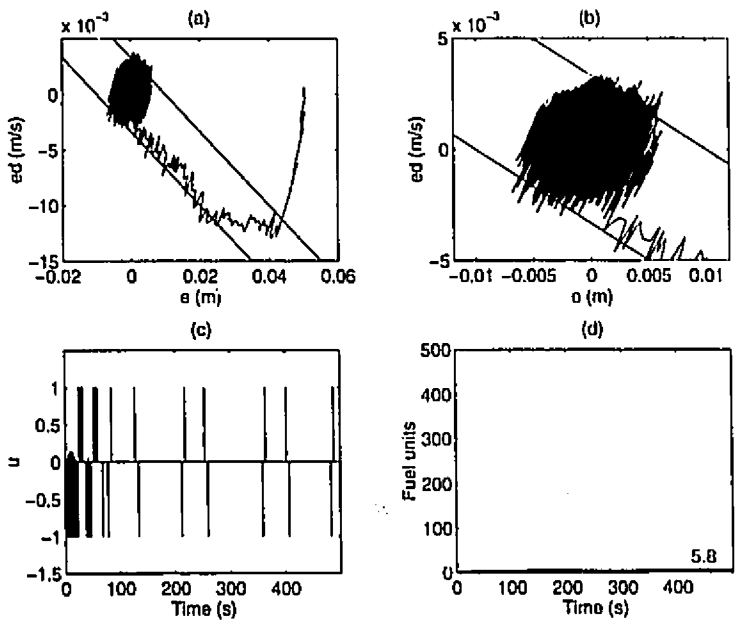

Figure 4.11: Simulation results for a stable noisy system without filters (σ_{noise} = 0.00066666 m). (a) Spacecraft error phase plane, (b) Spacecraft error phase plane (zoom), (c) Thruster command history, (d) Fuel consumption.

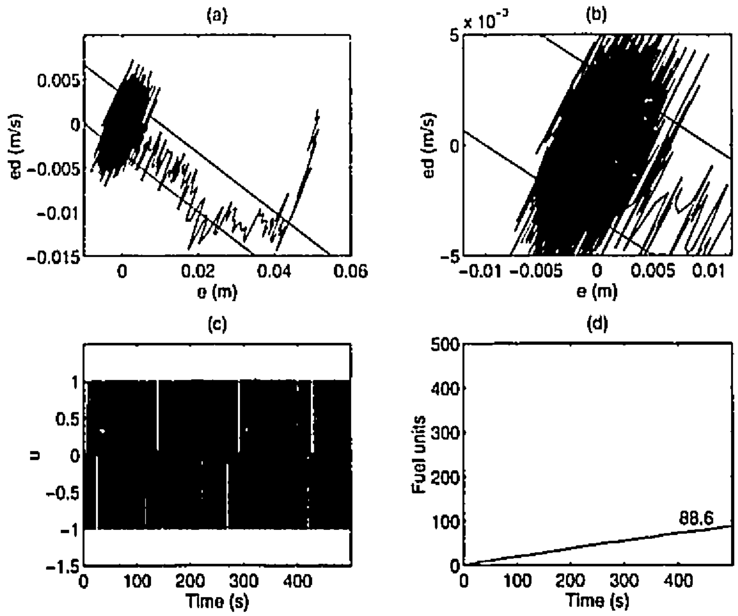

Figure 4.12: Simulation results for an unstable noisy system without filters (σ_{noise} = 0.00166667 m). (a) Spacecraft error phase plane, (b) Spacecraft error phase plane (zoom), (c) Thruster command history, (d) Fuel consumption.

4.7 Perturbation in the Model with an Asymptotic State Estimator

In Subsection 4.3.3, it was observed that the model with an asymptotic state estimator was almost always stable. However, for this model, a dynamic representation of the plant is required; it was assumed previously that this was perfectly known. In this section, the effect of perturbing the plant and adding noise in the system is addressed.

To perturb the system, we will assume that the actual mass of the spacecraft is M_{1p} = 250 kg instead of M_1 = 500 kg, as in Table 4.1. For the payload, its mass is increased by 50%, giving $M_{2p} = 1.5\beta M_1$. These perturbations are not realistic since the mass properties are usually well known in space system, but are chosen to show the robustness of this system to unmodelled uncertainties. The parameter values of Table 4.13 are used to run the same case of Subsection 4.3.3, while employing the perturbed masses for the plant. Using Eq.(2.16a), the first natural frequency is $\omega_n = 2\pi(0.049)$ rad/s, which is the same as for the non-perturbed case. White noise with a variance of $\sigma_{noise} = 0.00066666$ m is also added to the system. The simulation results of this perturbed-noisy system are presented in Fig. 4.13. It is noted that the system is still stable because the rate of fuel consumption is near zero. The total fuel consumption has increased somewhat from the non-perturbed system, i.e., 20.2 fuel units instead of 7.6 fuel units (Section 4.3.3). However, the important conclusion is that the system remains stable even with very perturbed mass properties and noise addition.

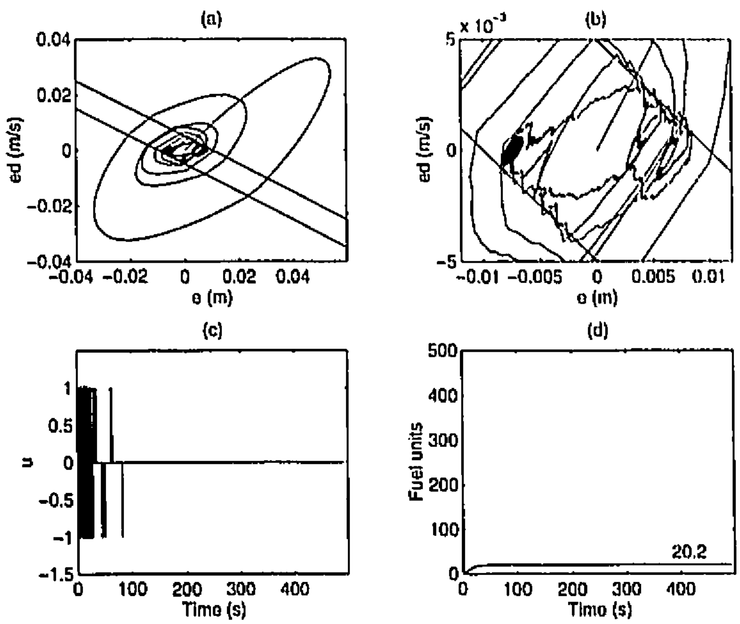

Figure 4.13: Simulation results for the model with an asymptotic state estimator with perturbed mass properties. (a) Spacecraft error phase plane, (b) Spacecraft error phase plane (zoom), (c) Thruster command history, (d) Fuel consumption.

The performance of the asymptotic state estimator is thus very good and considerably improves the stability zone of the actual controller used on the Space Shuttle. Using this state estimator, the likelihood of actually exciting the flexible modes of the manipulator is small, even when assuming large errors in the mass properties. Since all these mass properties are known precisely before sending an object in space, the performance cannot be worse than that studied in this section. Therefore, the model with an asymptotic state estimator provides very good control characteristics and is preferred over those studied in this thesis.

Chapter 5

Conclusions and Recommendations

5.1 Conclusions

This thesis examined the possible dynamic interactions between the attitude controller of a spacecraft and the flexible modes of a space manipulator mounted on it. The dynamic model of a two-flexible-joint planar manipulator mounted on a free-flying base was derived. Its natural frequencies were obtained using data from the Space Shuttle-CANADARM system. These frequencies were then used to determine the corresponding spring stiffness and damping coefficient of a simplified two-mass system that reproduced the relative motion of the payload (carried by the manipulator), with respect to the spacecraft. A classical attitude controller based on phase plane techniques was implemented to control the spacecraft. This attitude controller was integrated with the dynamic model of the simplified system in three different simulation models, cases 1, 2 and 3. The first simulation model, case 1, assumed that the position and the velocity of the spacecraft were obtained from sensor readings and the signals were simply passed through second-order filters to eliminate high frequency noise. In the second model, case 2, it was assumed that only the position was available by sensors and a state estimator was employed, which basically differentiates the filtered position signal to obtain an estimate of the velocity. This model is similar to the one used on the Space Shuttle. Finally, the last model, case 3, also employs the position data available by sensors; however, an asymptotic state estimator is used to obtain an estimate of the position and the velocity based on this signal.

Since the attitude controller assumes the use of on-off thrusters, which are nonlinear devices, techniques for analysis of nonlinear systems were required. The describing function method was used to analyze the characteristics of the three models and to perform a parametric study investigating the significant parameters of the system. The results obtained with this approximate method have been verified by simulation using *Simulink*, a *Matlab* package. These results were usually in agreement with those of the simulation and, therefore, we concluded that the describing function technique is a very good tool to analyze this type of nonlinear systems. Hence, the stability of a particular system can be verified quickly and easily using this method. Lengthy simulations need only be performed to examine critical stability limits, which requires less effort. Moreover, the conclusions of the parametric study were explained physically. These final conclusions are summarized below:

1. the cutoff frequency ω_f for the low-pass filters should be chosen as large as possible to avoid instability;

2. a small velocity gain λ can result in instability in the system; therefore, a large λ should be selected. However, one must be careful, since a large λ may lead to a type-2 instability for case 1, where the model with position and velocity filters is used;

3. the force level B of the thrusters should be chosen small for stability. Unstable types of behaviour are more likely to occur for large B. However, one must be careful because the system can be unstable for a very low thrust level as,

for example, in the case of the model with a velocity estimator and a position filter (always unstable when $B = 0.1$ N);

4. deadband limits δ should be chosen as large as possible to avoid instability in the system.

These conclusions can be used as guidelines in the design of an attitude controller. The describing function can thus be useful to readily find a stability margin of the chosen system.

From the three models studied, the case 1 where the model that assumes that the position and the velocity are available by sensors is the one that gives the worst performance. Due to the use of filters, lag is introduced in the system, which results in an unstable system. However, when high-quality sensors are available with a low noise level, the need of filters with a low cutoff frequency is less important; adequate performance can then be obtained with this model. It was shown that, at the limit, when the filters are removed, a stable system is possible, even in the presence of noise. The general poor performance of this system explains why velocity sensors are not currently used in accurate attitude control manoeuvres of the Space Shuttle.

The best performance case, out of the three models studied in this thesis, was obtained with the case 3 which uses an asymptotic state estimator. It was noted that stable systems were possible for very large parameter variations. In fact, stability problems were only present for a very low velocity gain λ, which corresponds, to large slopes for the switching lines. This estimator can be used to improve the performance of the actual attitude control systems when flexibility is a major concern. Even in the presence of large uncertainties in the mass properties, the performance obtained was very good. However, this state estimator requires an accurate dynamic model of the plant, even though it was demonstated in Section 4.7 that the controller performed adequately when a significant perturbation of mass properties was introduced into the model. This is not a large drawback, since accurate inertial properties of a spacecraft can be obtained prior to its launching into space. However, in the case of a space robotic system, the dynamics can become very complicated when flexibility in the links and joints of the robot, along with the payload flexibility, must be considered. The computational time required for this complicated system becomes significant, and the use of models running in real-time can become difficult and will be dependent upon the available hardware. However, a simpler approximate model may be sufficient to achieve good performance. More research is therefore needed on the possible implementation of this type of controller.

It was observed that the model with a velocity estimator and a position filter, as used on the Space Shuttle, did not provide very good performance. However, this observer is simple to implement since no dynamic model is necessary. If this model is selected for a particular system, the guidelines presented above can be used to choose the parameters that will provide good performance in a variety of conditions.

It should be mentioned that the stability of the system is also dependent upon the initial conditions. In the simulations reported in Chapter 4, the system was assumed to have a large initial error; it was attempted to restore it to within the deadband limits. Since the initial error is large, there is a high probability of exciting the flexible modes of the manipulator. In a more practical situation, the spacecraft would already be within the attitude limits and it would most likely be disturbed due to manipulator motion, hence requiring reaction control. In this case, the correcting action would take place when the error is small. Therefore, the thrusters would fire for a short period, as for a rigid body limit cycle, which would not likely excite the flexible modes. However, the rapid commanded motion of the manipulator could incur a larger disturbance; therefore, the chances to obtain an unstable system become more significant. In conclusion, even if the describing function method predicts an unstable system, a stable behaviour is still possible, but the motion must be executed slowly. This is due to the fact that in most unstable predictions, a stable system was also possible for small initial errors. In those cases, we concluded that the system was unstable due to the instability possibility. The use of an asymptotic state estimator in these cases would allow faster motions that are most likely expected in future space exploitation.

5.2 Recommendations for Future Work

The problem addressed in this thesis was solved in a very simplified form. There exists a wide range of further investigations that could be performed as an extension to this work. Some suggestions for future activities are outlined as follows:

1. Incorporate the dynamics of a two-flexible-joint manipulator in the models, instead of the dynamics of the simplified system.

2. Use an improved controller with optimum switching functions and velocity limits drift channel instead of the simple switching lines used in this thesis.

3. Extend the simulation models to a three-dimensional case, as opposed to the one-dimensional case considered here. A three-axis controller should therefore be developed.

4. In the case where the model with a velocity estimator and a position filter must be used, investigate the incorporation of compensation techniques to push the closed loop poles of the system to the left of the complex plane to eliminate lag due to the filter and, therefore, enlarge the stability zone of the system.

5. Study the implementation of the asymptotic state estimator for real-time control in the case of complicated dynamic models with limited computer time available.

6. Investigate the use of a Kalman filter in the case where noise properties are known.

7. Investigate the possibility of using pulse-width modulation techniques to control the position (attitude) of the spacecraft.

References

Alexander, H. L., and Cannon, R. H. Jr., 1990, "An Extented Operational-Space Control Algorithm for Satellite Manipulators," *The Journal of the Astronautical Sciences*, Vol. 38, No. 4, pp. 473–486.

Allen, A. C. M., D'Eleuterio, G. M. T., and MacLean, S. G., 1994, "An Investigation into the Control of Flexible Manipulators Using the Advanced Space Vision System," *Proc. of the second Workshop on Robotics in Space*, Montreal, Canada.

Anthony, T. C., Wie, B., and Carroll, S., 1990, "Pulse-Modulated Control Synthesis for a Flexible Spacecraft," *Journal of Guidance, Control, and Dynamics*, Vol. 13, No. 6, pp. 1014–1022.

Atherton, D. P., 1975, *Nonlinear Control Engineering*, Van Nostrand, New York.

Bryson, A. E., and Ho, Y., 1975, *Applied Optimal Control: Optimization, Estimation, and Control*, Hemisphere Pub. Corp., Washington.

Chen, C. T., 1984, *Linear System Theory and Design*, Holt, Rinehart, and Winston, New York.

Cyril, X., 1988, "Dynamics of Flexible-Link Manipulators," Ph. D dissertation, Dept. of Mechanical Engineering, McGill University, Montreal, Canada.

Dubowsky, S., Vance, E. E., and Torres, M. A., 1989, "The Control of Space Manipulators Subject to Spacecraft Attitude Control Saturation Limits," *Proc. of the NASA Conference on Space Telerobotics*, Jet Propulsion Lab., Passadena, CA, Vol. IV, pp. 409–418.

Flügge-Lotz, I., 1968, *Discontinuous and Optimal Control*, McGraw-Hill, New York.

Gelb, A., and Vander Velde, W. E., 1968, *Multiple-Input Describing Functions and Nonlinear System Design*, McGraw-Hill, New York.

Goldstein, H., 1980, *Classical Mechanics*, Addison-Wesley Pub. Co. , Reading, Mass.

Graham, D., and McRuer, D., 1961, *Analysis of Nonlinear Control Systems*, Wiley, New York.

Hablani, H. B., 1992, "Self-Balanced Modal Control for Spacecraft Using Thrusters and Adaptive Bandpass Filters," *Journal of Guidance, Control, and Dynamics*, Vol. 15, No. 3, pp. 587–596.

Hattis, P. D., et al., 1982, "Qualitative Differences Between On-Orbit and Transition RCS Control," *Proc. of the AIAA Guidance and Control Conference*, San Diego, CA, pp. 437–442.

Kubiak, E. T., and Martin, M. W., 1983, "Minimum Impulse Limit Cycle Design to Compensate for Measurement Uncertainties," *Journal of Guidance, Control, and Dynamics*, Vol. 6, No. 6, pp. 432–435.

Lindberg, R. E., Longman, R. W., and Zedd, M. F., 1990, "Kinematic and Dynamic Properties of an Elbow Manipulator Mounted on a Satellite," *The Journal of the Astronautical Sciences*, Vol. 38, No. 4, pp. 397–421.

Longman, R. W., 1990a, "Attitude Tumbling Due to Flexibility in Satellite-Mounted Robots," *The Journal of the Astronautical Sciences*, Vol. 38, No. 4, pp. 487–509.

Longman, R. W., 1990b, "The Kinetics and Workspace of a Satellite-Mounted Robot," *The Journal of the Astronautical Sciences*, Vol. 38, No. 4, pp. 423–440.

Longman, R. W., Lindberg, R. E., and Zedd, M. F., 1987, "Satellite-Mounted Robot Manipulators — New Kinematics and Reaction Moment Compensation," *International Journal of Robotics Research*, Vol. 6, No. 3, pp. 87–103.

Lyndon B. Johnson Space Center, 1976, *Space Shuttle*, NASA, Washington.

Millar, R. A., and Vigneron, F. R., 1979, "Attitude Stability of a Pseudorate Jet-Controlled Flexible Spacecraft," *Journal of Guidance, Control, and Dynamics*, Vol. 2, No. 2, pp. 111–118.

Nakamura, Y., and Mukherjee, R., 1991, "Nonholonomic Path Planning of Space Robots via a Bidirectional Approach," *IEEE Transactions on Robotics and Automation*, Vol. 7, No. 4, pp. 500–514.

Nakano, M. M., and Willms, R. L., 1982, "Space Shuttle On-Orbit Flight Control System," *Proc. of the AIAA Guidance and Control Conference*, San Diego, CA, pp. 429–436.

Nenchev, D., Umetani, Y., and Yoshida, K., 1992, "Analysis of a Redundant Free-Flying Spacecraft/Manipulator System," *IEEE Transactions on Robotics and Automation*, Vol. 8, No. 1, pp. 1–6.

Ogata, K., 1990, *Modern Control Engineering*, 2nd Edition, Prentice Hall, Englewood Cliffs, N.J.

Papadopoulos, E., 1990, "On the Dynamics and Control of Space Manipulators," Ph. D dissertation, Dept. of Mechanical Engineering, Massachusetts Institute of Technology, Cambridge, MA.

Papadopoulos, E., and Dubowsky, S., 1991a, "Coordinated Manipulators/Spacecraft Motion Control for Space Robotic Systems," *Proceedings of the IEEE International Conference on Robotics and Automation*, Vol. 2, pp. 1696–1701.

Papadopoulos, E., and Dubowsky, S., 1991b, "On the Nature of Control Algorithms for Free-Floating Space Manipulators," *IEEE Transactions on Robotics and Automation*, Vol. 7, No. 6, pp. 750–758.

Papadopoulos, E., and Dubowsky, S., 1993, "Dynamic Singularities in Free-Floating Space Manipulators," *ASME Journal of Dynamic Systems, Measurement, and Control*, Vol. 115, No. 1, pp. 44–52.

Penchuk, A. N., Hattis, P. D., and Kubiak, E. T., 1985, "A Frequency Domain Stability Analysis of a Phase Plane Control System," *Journal of Guidance, Control, and Dynamics*, Vol. 8, No. 1, pp. 50–55.

Quinn, R. D., Chen, J. L., and Lawrence, C., 1994, "Base Reaction Control for Space-Based Robots Operating in Microgravity Environment," *Journal of Guidance, Control, and Dynamics*, Vol. 17, No. 2, pp. 263–270.

Redding, D. C., and Adams, N. J., 1987, "Optimized Rotation-Axis Attitude Maneuver Controller for the Space Shuttle Orbiter," *Journal of Guidance, Control, and Dynamics*, Vol. 10, No. 1, pp. 4–13.

Sackett, L. L., and Kirchwey, C. B., 1982, "Dynamic Interaction of the Shuttle On-Orbit Flight Control System with Deployed Flexible Payload," *Proc. of the AIAA Guidance and Control Conference*, San Diego, CA, pp. 232–245.

Singer, N. C., 1989, "Residual Vibration Reduction in Computer Controlled Machines," Technical Report 1030, MIT Artificial Intelligence Laboratory, Cambridge, MA.

Skaar, S. B., Tang, L., and Yalda-Mooshabad, I., 1986, "On-Off Attitude Control of Flexible Satellites," *Journal of Guidance, Control, and Dynamics*, Vol. 9, No. 4, pp. 507–510.

Slotine, J.-J. E., and Li, W., 1991, *Applied Nonlinear Control*, Prentice Hall, Englewood Cliffs, N.J.

Spofford, J. R., and Akin, D. L., 1990, "Redundancy Control of a Free-Flying Telerobot," *Journal of Guidance, Control and Dynamics*, Vol. 13, No. 3, pp. 515–523.

Torres, M. A., and Dubowsky, S., 1992, "Minimizing Spacecraft Attitude Disturbances in Space Manipulator Systems," *Journal of Guidance, Control, and Dynamics*, Vol. 15, No. 4, pp. 1010–1017.

Umetani, Y., and Yoshida, K., 1989, "Resolved Motion Rate Control of Space Manipulators with Generalized Jacobian Matrix," *IEEE Transactions on Robotics and Automation*, Vol. 5, No. 3, pp. 303–314.

Vafa, Z., and Dubowsky, S., 1987, "On the Dynamics of Manipulators in Space Using the Virtual Manipulator Approach," *Proceedings of the IEEE International Conference on Robotics and Automation*, pp. 579–585.

Vafa, Z., and Dubowsky, S., 1990a, "The Kinematics and Dynamics of Space Manipulators: The Virtual Manipulator Approach," *International Journal of Robotics Research*, Vol. 9, No. 4, pp. 3–21.

Vafa, Z., and Dubowsky, S., 1990b, "On the Dynamics of Space Manipulators Using the Virtual Manipulator, with Applications to Path Planning," *The Journal of the Astronautical Sciences*, Vol. 38, No. 4, pp. 441–472.

Vander Velde, W. E., and He, J., 1983, "Design of Space Structure Control Systems using On-Off Thrusters," *Journal of Guidance, Control, and Dynamics*, Vol. 6, No. 1, pp. 53–60.

Wie, B., and Plescia, C. T., 1984, "Attitude Stabilization of Flexible Spacecraft During Stationkeeping Maneuvers," *Journal of Guidance, Control, and Dynamics*, Vol. 7, No. 4, pp. 430–436.

Appendix A

Expressions of Coriolis and Centrifugal Terms

The $N_{ij}(\mathbf{q}_r, \dot{\mathbf{q}}_r)$ expressions of Eq.(2.10) are given by

$$N_{11}(\mathbf{q}_r, \dot{\mathbf{q}}_r) = \frac{1}{2}\left(\frac{D_1 + D_2}{D}\right)^2 \frac{\partial D}{\partial q_2}\dot{q}_2 - \left(\frac{D_1 + D_2}{D}\right)\left(\frac{\partial D_1}{\partial q_2} + \frac{\partial D_2}{\partial q_2}\right)\dot{q}_2 \tag{A.1}$$

$$\begin{aligned} N_{12}(\mathbf{q}_r, \dot{\mathbf{q}}_r) = & -2\left(\frac{D_1 + D_2}{D}\right)\left(\frac{\partial D_1}{\partial q_4} + \frac{\partial D_2}{\partial q_4}\right)\dot{q}_2 + \left(\frac{D_1^2 + D_2^2}{D^2}\right)\frac{\partial D}{\partial q_4}\dot{q}_2 \\ & + \frac{D_1 D_2}{D^2}\frac{\partial D}{\partial q_4}(2\dot{q}_2 + \dot{q}_4) + \frac{\partial d_{12}}{\partial q_4}(2\dot{q}_2 + \dot{q}_4) \\ & + \left(\frac{D_2}{D}\right)^2\left(\frac{\partial D}{\partial q_4} - \frac{1}{2}\frac{\partial D}{\partial q_2}\right)\dot{q}_4 + \frac{D_2}{D}\left(\frac{\partial D_2}{\partial q_2} - \frac{\partial D_1}{\partial q_4}\right)\dot{q}_4 \\ & - \left(\frac{D_1 + 2D_2}{D}\right)\frac{\partial D_2}{\partial q_4}\dot{q}_4 \end{aligned} \tag{A.2}$$

$$\begin{aligned} N_{21}(\mathbf{q}_r, \dot{\mathbf{q}}_r) = & -\frac{1}{2}\left(\frac{D_1 + D_2}{D}\right)^2 \frac{\partial D}{\partial q_4}\dot{q}_2 + \left(\frac{D_1 + D_2}{D}\right)\left(\frac{\partial D_1}{\partial q_4} + \frac{\partial D_2}{\partial q_4}\right)\dot{q}_2 \\ & - \frac{D_2}{D}\frac{\partial D_1}{\partial q_2}\dot{q}_2 - \left(\frac{D_1 + 2D_2}{D}\right)\frac{\partial D_2}{\partial q_2}\dot{q}_2 + \left(\frac{D_1 D_2 + D_2^2}{D^2}\right)\frac{\partial D}{\partial q_2}\dot{q}_2 \\ & + \left(\frac{D_2}{D}\right)^2 \frac{\partial D}{\partial q_2}\dot{q}_4 - 2\left(\frac{D_2}{D}\right)\frac{\partial D_2}{\partial q_2}\dot{q}_4 + \frac{\partial d_{12}}{\partial q_4}\dot{q}_4 \end{aligned} \tag{A.3}$$

$$N_{22}(\mathbf{q}_r, \dot{\mathbf{q}}_r) = \frac{1}{2}\left(\frac{D_2}{D}\right)^2 \frac{\partial D}{\partial q_4}\dot{q}_4 - \frac{D_2}{D}\frac{\partial D_2}{\partial q_4}\dot{q}_4 \,, \tag{A.4}$$

where

$$
\begin{aligned}
\frac{\partial d_{12}}{\partial q_4} &= -\left[\frac{m_1 m_2}{M} r_1 l_2 + \frac{m_0 m_2}{M} l_2(l_1 + r_1)\right] \sin(q_4) \\
\frac{\partial D_1}{\partial q_2} &= -\frac{m_0 r_0}{M}\left[l_1(m_1 + m_2) + r_1 m_2\right] \sin(q_2) \\
\frac{\partial D_1}{\partial q_4} &= -\left[\frac{m_1 m_2}{M} r_1 l_2 + \frac{m_0 m_2}{M} l_2(l_1 + r_1)\right] \sin(q_4) \\
\frac{\partial D_2}{\partial q_2} &= -\frac{m_0 m_2}{M} r_0 l_2 \sin(q_2 + q_4) \\
\frac{\partial D_2}{\partial q_4} &= -\frac{m_1 m_2}{M} r_1 l_2 \sin(q_4) - \frac{m_0 m_2}{M} l_2\left[(l_1 + r_1)\sin(q_4) + r_0 \sin(q_2 + q_4)\right] \\
\frac{\partial D}{\partial q_2} &= -2\frac{m_0 r_0}{M}\left\{\left[l_1(m_1 + m_2) + r_1 m_2\right] \sin(q_2) + m_2 l_2 \sin(q_2 + q_4)\right\} \\
\frac{\partial D}{\partial q_4} &= -2\frac{m_1 m_2}{M} r_1 l_2 \sin(q_4) - 2\frac{m_0 m_2}{M} l_2\left[(l_1 + r_1)\sin(q_4) + r_0 \sin(q_2 + q_4)\right] .
\end{aligned}
$$

Appendix B

Transfer Function Derivation of the Linear Elements of the Simulation Models

In this Appendix, the transfer function of the linear elements of the three models studied in this thesis are derived. This transfer function is represented by $G(s)$ in Fig. B.1. By examining Fig. B.1, we can write

$$\sigma = -y$$
$$\sigma = -G(s)u \tag{B.1}$$

where u is the output of the relay nonlinearity, either $+1$, 0 or -1.

Therefore, if an equation similar to Eq.(B.1) can be obtained, this means that the model is reduced into a suitable form for describing function analysis.

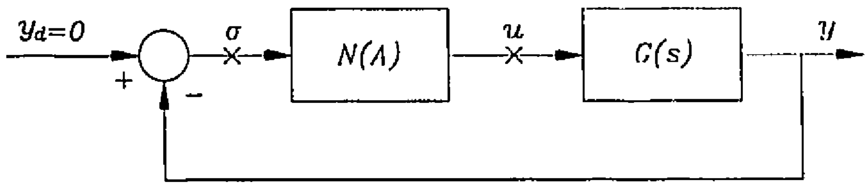

Figure B.1: A nonlinear system.

B.1 Case 1: Model with Position and Velocity Filters

The dynamics of the plant in the model presented in Fig. B.2 is represented in state-space form. The transfer function describing this dynamics can be written as

$$G_1(s) = \mathbf{E}(s\mathbf{I} - \mathbf{A})^{-1}\mathbf{b} \ . \tag{B.2}$$

Using the expressions of **A**, **b** and **E**, defined in Eqs.(2.26) and (3.22), we obtain

$$G_1(s) = \begin{bmatrix} G_p(s) \\ sG_p(s) \end{bmatrix} \tag{B.3}$$

where $G_p(s)$ is defined in Eq.(2.57) and represents the plant transfer function.

Therefore, examining Fig. B.2, with the use of Eq.(B.3), we can write

$$\begin{aligned} \sigma &= -\hat{y}_1 - \lambda\dot{\hat{y}}_1 \\ &= -G_f(s)y_1 - \lambda G_f(s)\dot{y}_1 \\ &= -G_f(s)\exp^{-\tau s} G_p(s)u - \lambda G_f(s)\exp^{-\tau s} sG_p(s)u \\ &= -(1+\lambda s)\exp^{-\tau s} G_p(s)G_f(s)u \\ \sigma &= -G_{\text{filter}}(s)u \ , \end{aligned} \tag{B.4}$$

by defining

$$G_{\text{filter}}(s) = (1+\lambda s)\exp^{-\tau s} G_p(s)G_f(s) \ .$$

Equation (B.4) is of the same form of Eq.(B.1) and therefore, $G_{\text{filter}}(s)$ is the transfer function of the linear elements of the model with position and velocity filters.

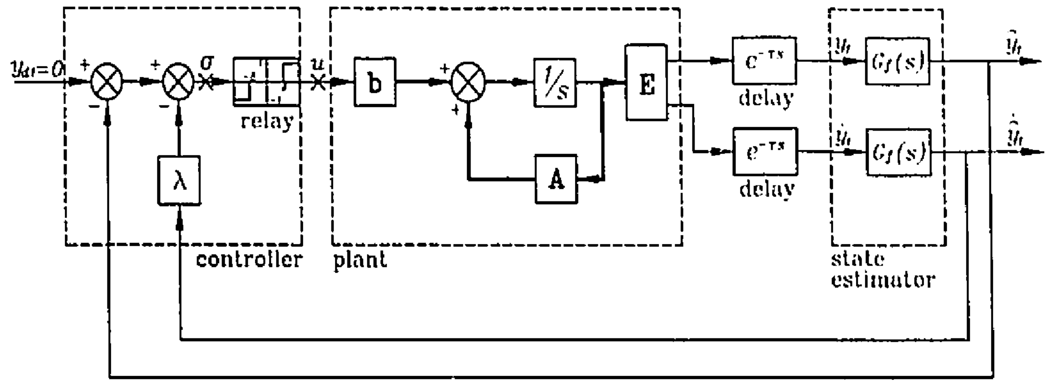

Figure B.2: Case 1: model with position and velocity filters.

B.2 Case 2: Model with a Velocity Estimator and a Position Filter

Examining Fig. B.3, we can write

$$\begin{aligned}
\sigma &= -\hat{y}_1 - \lambda\hat{\dot{y}}_1 \\
&= -G_f(s)y_1 - \lambda\Big(sG_{se}(s)\hat{y}'_f + \frac{1}{s}\frac{B}{M_t}u\Big) \\
&= -G_f(s)\exp^{-\tau s}G_p(s)u \\
&\qquad -\lambda\Big[sG_{se}(s)\Big(\exp^{-\tau s}G_p(s)u - \frac{1}{s^2}\frac{B}{M_t}u\Big) + \frac{1}{s}\frac{B}{M_t}u\Big] \\
&= -\Big[\exp^{-\tau s}G_p(s)\Big(G_f(s) + \lambda sG_{se}(s)\Big) + \frac{\lambda B}{M_t s}\Big(1 - G_{se}(s)\Big)\Big]u \\
\sigma &= -G_{\text{rate}}(s)u \qquad \text{(B.5)}
\end{aligned}$$

by defining

$$G_{\text{rate}}(s) = \exp^{-\tau s}G_p(s)\Big(G_f(s) + \lambda sG_{se}(s)\Big) + \frac{\lambda B}{M_t s}\Big(1 - G_{se}(s)\Big)\,.$$

Equation (B.5) is of the same form of Eq.(B.1) and therefore, $G_{\text{rate}}(s)$ is the transfer function of the linear elements of the model with a velocity estimator and a position filter.

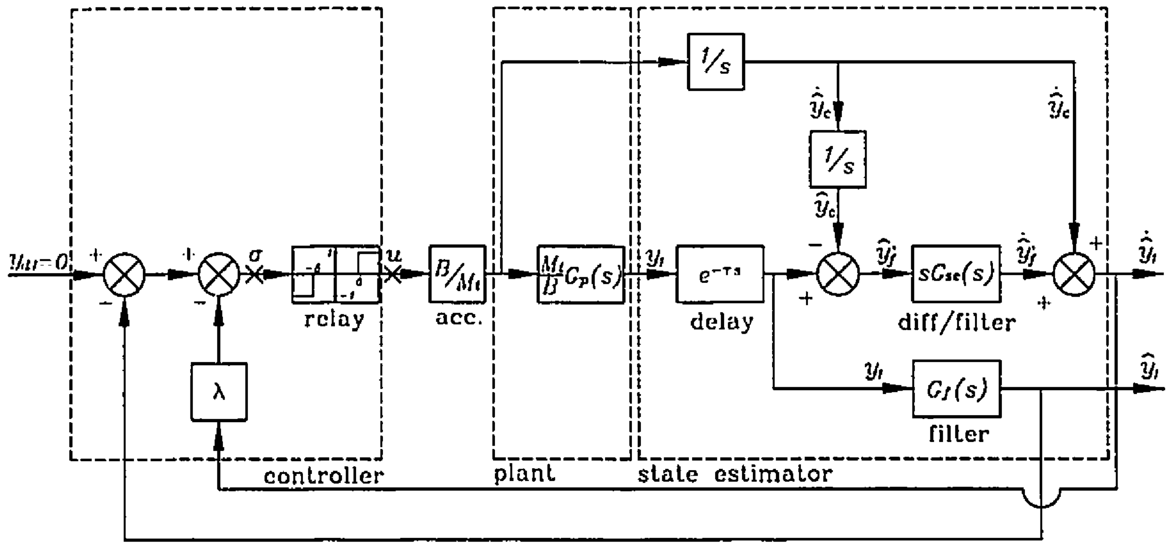

Figure B.3: Case 2: model with a velocity estimator and a position filter.

B.3 Case 3: Model with an Asymptotic State Estimator

The dynamics of the plant in the model presented in Fig. B.4 is represented in state-space form. This dynamics is written in transfer function form in Subsection 2.3.2, and the transfer function representing this dynamics is given by $G_p(s)$ which is defined in Eq.(2.57).

For the state estimator part, we have

$$\begin{aligned}\dot{\hat{\mathbf{x}}} &= \mathbf{A}\hat{\mathbf{x}} + \mathbf{b}u + \mathbf{k}(y_1 - \mathbf{c}^T\hat{\mathbf{x}}) \\ &= (\mathbf{A} - \mathbf{k}\mathbf{c}^T)\hat{\mathbf{x}} + \mathbf{b}u + \mathbf{k}y_1 \\ &= (\mathbf{A} - \mathbf{k}\mathbf{c}^T)\hat{\mathbf{x}} + \begin{bmatrix} \mathbf{b} & \mathbf{k} \end{bmatrix} \begin{bmatrix} u \\ y_1 \end{bmatrix} .\end{aligned} \tag{B.6}$$

We also have

$$\begin{bmatrix} \hat{y}_1 \\ \dot{\hat{y}}_1 \end{bmatrix} = \mathbf{E}\hat{\mathbf{x}} . \tag{B.7}$$

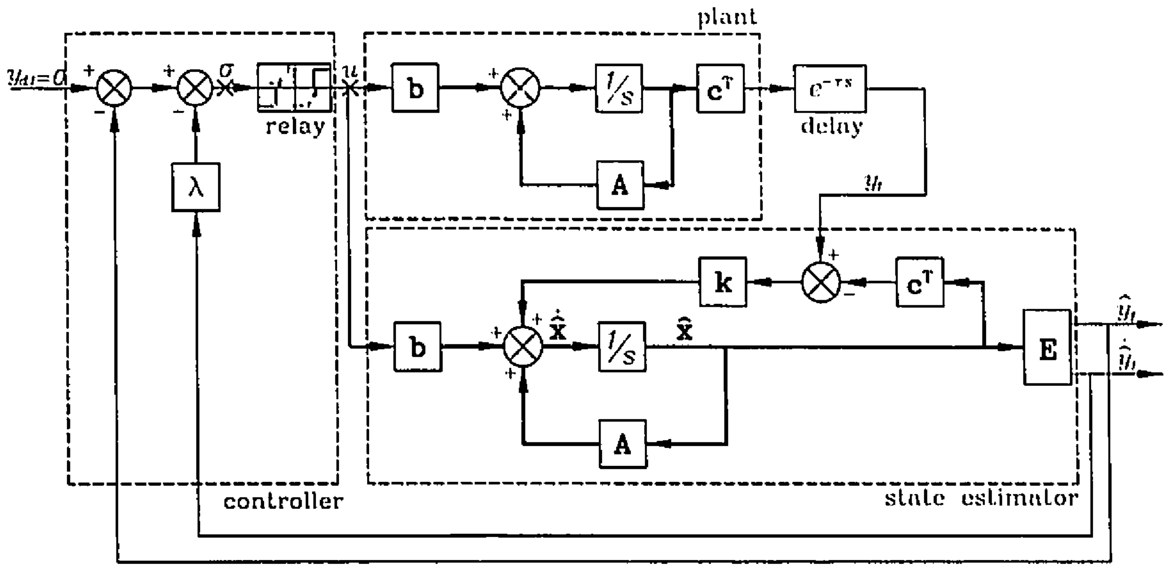

Figure B.4: Case 3: model with an asymptotic state estimator.

In transfer function form, Eqs.(B.6) and (B.7) can be written as

$$\begin{bmatrix} \hat{y}_1 \\ \dot{\hat{y}}_1 \end{bmatrix} = G_2(s) \begin{bmatrix} u \\ y_1 \end{bmatrix} \tag{B.8}$$

where

$$G_2(s) = \mathbf{E}\Big(s\mathbf{I} - (\mathbf{A} - \mathbf{k}\mathbf{c}^T)\Big)^{-1} \begin{bmatrix} \mathbf{b} & \mathbf{k} \end{bmatrix} .$$

Using the expressions of **A**, **b**, **c**, **E** and **k**, which are defined in Eqs.(2.26), (2.27), (3.22) and (3.18) respectively, we obtain

$$G_2(s) = \begin{bmatrix} g_{11}(s) & g_{12}(s) \\ g_{21}(s) & g_{22}(s) \end{bmatrix} \tag{B.9}$$

with

$$g_{11}(s) = \frac{M_2 s^2 + cs + k}{D(s)} ,$$

$$g_{12}(s) = \frac{M_1 M_2\Big[L_1 s^3 + \Big(\frac{cL_1}{\mu} + L_2\Big)s^2\Big] + \Big(kM_1L_1 + cM_1L_2 + kM_2L_3 + cM_2L_4\Big)s + kM_1L_2 + kM_2L_4}{D(s)} ,$$

$$g_{21}(s) = \frac{M_2 s^3 + \left(c + L_1 M_2\right)s^2 + \left(k + cL_1\right)s + kL_1}{D(s)} \,,$$

$$g_{22}(s) = \frac{\begin{array}{r} M_1 M_2 L_2 s^3 + \Big(cM_1 L_2 - kM_2 L_1 + kM_2 L_3 + \\ cM_2 L_4\Big)s^2 + \left(kM_1 L_2 + kM_2 L_4\right)s \end{array}}{D(s)} \,,$$

and

$$D(s) = M_1 M_2\left[s^4 + \left(\frac{c}{\mu} + L_1\right)s^3 + \left(\frac{k}{\mu} + \frac{cL_1}{\mu} + L_2\right)s^2\right] + \\ \left(kM_1 L_1 + kM_2 L_3 + cM_1 L_2 + cM_2 L_4\right)s + kM_1 L_2 + kM_2 L_4 \,.$$

The block diagram of Fig. B.4 can therefore be represented as the one of Fig. B.5.

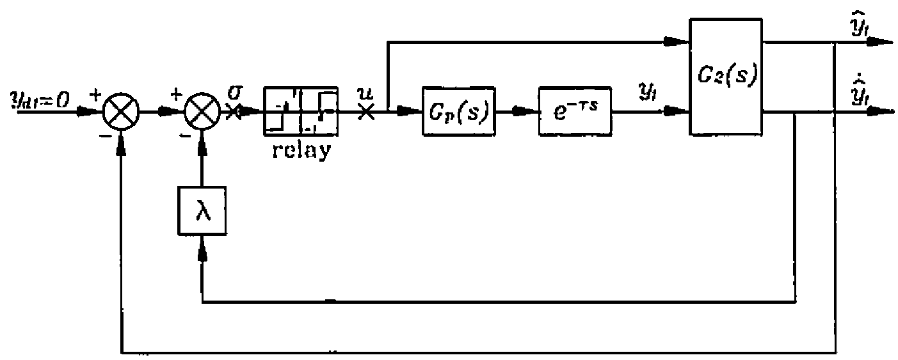

Figure B.5: Model with an asymptotic state estimator using transfer functions.

Examining Fig. B.5, we can write

$$\begin{aligned} \sigma &= -\hat{y}_1 - \lambda\dot{\hat{y}}_1 \\ &= -\begin{bmatrix} 1 & \lambda \end{bmatrix}\begin{bmatrix} \hat{y}_1 \\ \dot{\hat{y}}_1 \end{bmatrix} \\ &= -\begin{bmatrix} 1 & \lambda \end{bmatrix}\begin{bmatrix} g_{11}(s) & g_{12}(s) \\ g_{21}(s) & g_{22}(s) \end{bmatrix}\begin{bmatrix} u \\ y_1 \end{bmatrix} \end{aligned}$$

$$
\begin{aligned}
&= -\begin{bmatrix} 1 & \lambda \end{bmatrix} \begin{bmatrix} g_{11}(s) & g_{12}(s) \\ g_{21}(s) & g_{22}(s) \end{bmatrix} \begin{bmatrix} u \\ \exp^{-\tau s} G_p(s) u \end{bmatrix} \\
&= -\begin{bmatrix} 1 & \lambda \end{bmatrix} \begin{bmatrix} g_{11}(s) & g_{12}(s) \\ g_{21}(s) & g_{22}(s) \end{bmatrix} \begin{bmatrix} 1 \\ \exp^{-\tau s} G_p(s) \end{bmatrix} u \\
\sigma &= -G_{\text{asym}}(s) u
\end{aligned}
\tag{B.10}
$$

by defining

$$
G_{\text{asym}}(s) = \begin{bmatrix} 1 & \lambda \end{bmatrix} \begin{bmatrix} g_{11}(s) & g_{12}(s) \\ g_{21}(s) & g_{22}(s) \end{bmatrix} \begin{bmatrix} 1 \\ \exp^{-\tau s} G_p(s) \end{bmatrix}.
$$

where $g_{11}(s)$, $g_{12}(s)$, $g_{21}(s)$ and $g_{22}(s)$ are defined in Eq.(B.9).

Equation (B.10) is of the same form of Eq.(B.1) and therefore, $G_{\text{asym}}(s)$ is the transfer function of the linear elements of the model with an asymptotic estimator.